Ph.D. DISSERTATION

Investigations of Concentration Boundary Layer along Heterogeneous Nano-porous Membrane Fabricated with Adhesive Lift Method

접착식 리프트 방법으로 제작된 비균일한 나노다공성 막을 따라 형성되는 농도경계층에 대한 연구

August 2022

Department of Electrical and Computer Engineering
College of Engineering
Seoul National University

Myungin Seo

Investigations of Concentration Boundary Layer along Heterogeneous Nano-porous Membrane Fabricated with Adhesive Lift Method

지도 교수 김 성 재

이 논문을 공학박사 학위논문으로 제출함
2022년 8월

서울대학교 대학원
전기·정보 공학부
서 명 진

서명진의 공학박사 학위논문을 인준함
2022년 8월

위 원 장	홍 용 택	(Seal)
부위원장	김 성 재	(Seal)
위 원	김 호 영	(Seal)
위 원	이 종 호	(Seal)
위 원	곽 노 균	(Seal)

Abstract

Nanochannels have been widely utilized in micro/nanofluidic systems due to the unique characteristics of the nanochannels. One of the most unique characteristics is ion selectivity induced by the overlap of electrical double layer. Using ion selectivity, electrokinetic systems employing nanochannels have been widely developed. Due to the scalability and visibility, micro/nanofluidic platforms have been utilized for the fundamental studies of the electrokinetic systems. To simulate the realistic macro systems, the micro platforms have been fabricated with a design which mimics the systems. However, the designs of the platforms have been limited due to the limitations in the nanojunction fabrication methods. Therefore, in this thesis, a nanoporous membrane patterning method was developed and concentration boundary layers were investigated with micro/nanofluidic platforms fabricated with the patterning method.

First, an arbitrary-shaped nanoporous membrane fabrication with adhesive lift method was presented. The presented method utilizes oxygen plasma treatment and spin coating for the uniform and precise patterning of the nanoporous membrane. To demonstrate the fabrication method, we fabricated micro/nanofluidic platforms with membranes patterned along microchannels with surface shape of square, sine, sawtooth, triangle and fractal wave and with depth of 5 μm, 15 μm and 150 μm. The conformal patterning was confirmed by direct visualization of ion concentration polarization in three mechanisms (surface conduction, electroosmotic flow and electroosmotic instability). Furthermore, the different effect of undulated surface on ion concentration polarization in electroosmotic flow regime and electroosmotic

instability regime was evaluated with direct visualization and electric measurements. Therefore, we suggest that the presented nanoporous membrane fabrication method would enable the fabrication of near-practical micro/nanofluidic platforms.

Secondly, we demonstrated the alignment of electroconvection utilizing reinforcing structures which have been utilized as physical component of ion selective membrane. The experimental devices were fabricated with the adhesive lift method. Through numerical simulation and experiments, we confirmed that the stable electroconvection was aligned with reinforcements which was wide in width and close to ion depletion zone, and the geometric conditions of reinforcements for the stable vortex alignment was confirmed. Furthermore, the electroconvection in chaotic regime was also aligned with reinforcing structures. Due to the alignment, the chaotic electroconvection was stabilized and the stabilization was quantified with time-averaged profiles of cation concentration (simulation) and fluorescence intensity (experiment). Moreover, we demonstrated that the electric current was stabilized with the reinforcing structures inside the ion selective membranes. Thus, we present that the reinforcing structures would be utilized for the stabilization of electroconvection in various concentration polarization systems.

Finally, we presented a continuous and spontaneous nanoparticle separator based on diffusiophoresis induced by ion exchange. The diffusiophoretic separator was fabricated with the adhesive lift method. In the separator, the exclusion distance followed the scaling law of the conventional spontaneous diffusiophoretic system. Thus, we separated particles with different diffusiophoretic mobility due to the difference of size (40 nm, 200 nm and 2 μm). Furthermore, the separation resolution was increased by enhanced concentration gradient induced by addition of Tris buffer. The addition of Tris also played a role as a pH regulator so that the

separated buffer stream can be appropriate for pH-sensitive biomolecules. Therefore, we expect the presented continuous and spontaneous diffusiophoretic separation platform to be utilized for analysis of various nanoscale biomolecules.

Keywords: Electrokinetic phenomena, Adhesive Lift Method, Ion Selectivity, Ion Concentration Polarization, Electroconvection, Diffusiophoresis.

Student Number: 2017-23030

Table of Contents

List of Figures

List of Tables

Chapter 1. Introduction

1.1. Ion-selectiviy of a Nanochannel

Nanochannels have been reported to have unique characteristics unlike microchannels. One of the main characteristics is ion selectivity which is induced by overlap of electrical double layer (EDL). When a microchannel is filled with electrolyte, the ions in the electrolyte is affected by the electric field induced by the surface charge at the microchannel wall[1]. Therefore, when the wall is negatively charged, the concentration of cations near the wall becomes higher than the concentration at bulk and the electric potential exponentially increases to zero with distance from the wall. The EDL is defined as the layer near the wall with the ion distribution which is different from that of the bulk. In the case of symmetrical electrolyte, the thickness of EDL is measured as

$$\lambda_D = \left(\frac{\varepsilon_0 \varepsilon_r k_B T}{2 e^2 z^2 n_\infty} \right)^{1/2}, \tag{1.1}$$

where ε_0 is permittivity of free space, ε_r is the relative permittivity, k_B is Boltzmann constant, T is the absolute temperature, e is elementary charge, z is the valence of the ion and n_∞ is the bulk concentration[2]. As indicated in the equation (1.1), the thickness of the electrical double layer depends on the bulk concentration of the electrolyte. Hence, the Debye length in the microchannel filled with 1 mM KCl solution is 10 nm at room temperature and the Debye length decreases as the ionic strength of the solution increases.

In the case of microchannels, ions in the electrolyte move freely in the center of

the channel since the width of the channel is extremely large compared to the thickness of EDL as shown in Figure 1.1(a). On the other hand, in the case of nanochannels, the size of the nanochannel is small compared to the EDL so that the EDLs on the walls overlaps each other as shown in Figure 1.1(b). Consequently, only cations exist within the overlapped electrical double layer inside the negatively charged nanochannel. Therefore, cations can pass through the nanochannel while anions are blocked at the nanochannel, which is called ion selectivity. In this thesis, Nafion was mainly utilized as nanojunction so that cation-selective transport was mainly covered in this thesis[3].

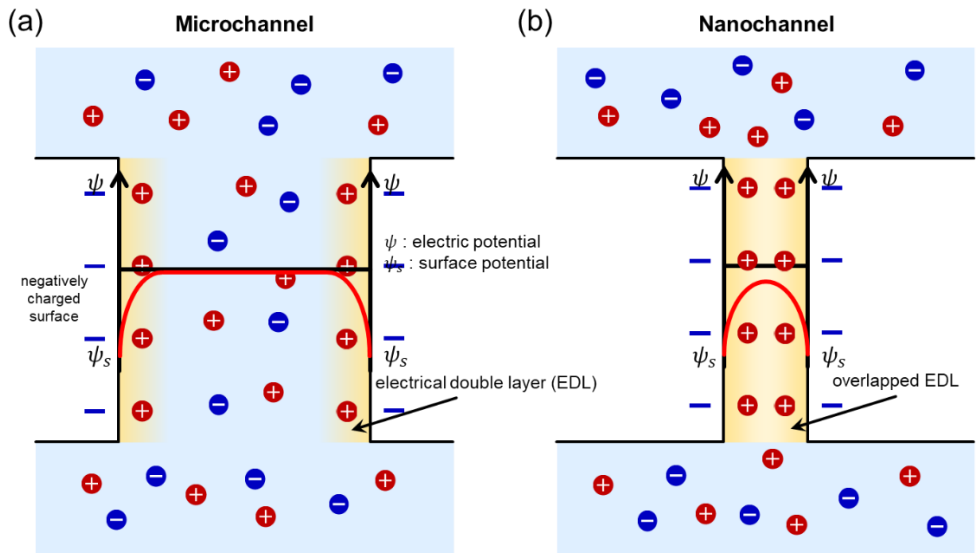

Figure 1.1. The schematic diagram of the ion distribution and the electric potential distribution inside (a) a microchannel and (b) a nanochannel.

1.2. Ion Concentration Polarization

Using ion selectivity induced by nanochannel, unique phenomena have been reported. One of the phenomena is ion concentration polarization (ICP). ICP refers to a phenomenon described next. When voltage is applied across an ion exchange membrane immersed in electrolyte, due to ion selectivity, counterions pass through the membrane by the electric field while co-ions are blocked at the exchange membrane. In the case of cation exchange membrane, anions in the cathodic electrolyte are moved to the cathode side of the membrane by the electric field. Since anions on the cathode side cannot pass to the anode side of the membrane, anions accumulate on the cathode side. Due to the electric neutrality, the concentration of cations also increases on the cathode side and the region is called ion enrichment zone. On the other hand, anions on the anode side of the membrane are moved to the anode by the electric field so that the concentration of anions decreases since the anions on the cathode side of the membrane cannot pass to the anode side. To maintain the electric neutrality, the concentration of cations also decreases in the anode side of the membrane. As a result, the ions are depleted in the anode side of the cation exchange membrane and the region is called ion depletion zone (IDZ) as shown in Figure 1.2[4]. The detailed study utilizing this phenomenon would be explained in Chapter 2 and 3.

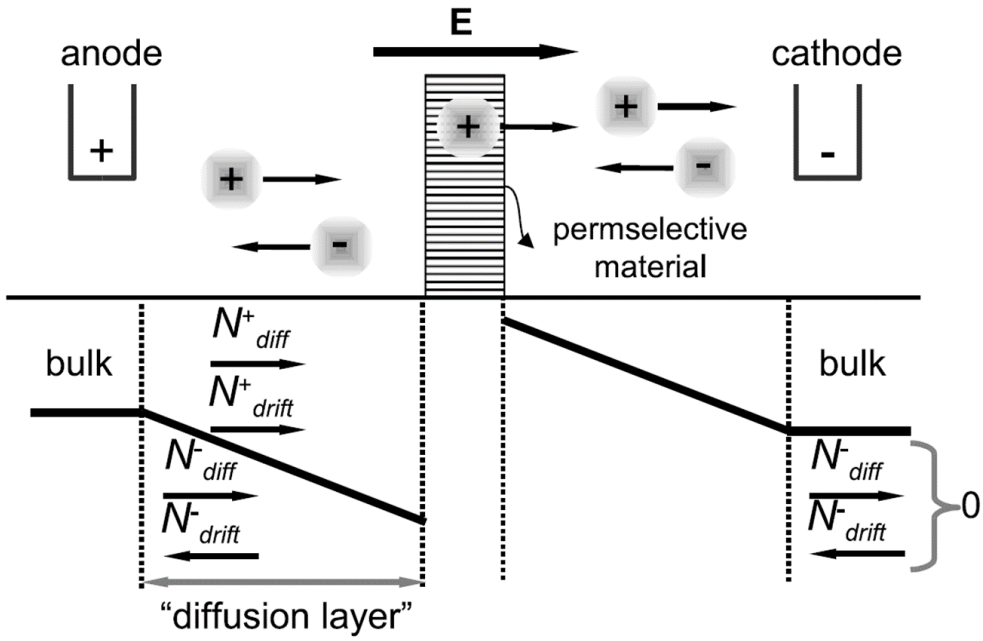

Figure 1.2. The schematic diagram of ion concentration polarization[4].

1.2.1. Mechanisms of Overlimiting Conductance

In the early stage of electrokinetic study about the overlimiting conductance, electric currents through a nanoporous membrane was predicted to be saturated to a constant value due to the decrease of the ion concentration in the anode side, which is called limiting current. However, it has kept to be reported that the current increases over the limiting current as a function of the applied voltage. Under this circumstance, the current exceeds the limiting current, called overlimiting current. Thus, the slope of the overlimiting current as a function of applied voltage would give a overlimiting conductance. While several mechanisms have been suggested, Bazant et al mainly categorized the mechanism for overlimiting conductance as surface conduction (SC), electroosmotic flow (EOF) and electroosmotic instability (EOI) as shown in Figure 1.3[5].

Whether SC, EOF or EOI is the main mechanism of overlimiting conductance in an ICP platform is determined by the ion transport pathway. In a microfluidic channel, ions are mainly transported by wall transport or bulk transport. The characteristic length scale of the microchannel is the main factor for determining the proportion of wall transport in the total ion transport. If the width and length of the microchannel are sufficiently long, convection in the microchannel is suppressed as the microchannel depth decreases so that the effect of bulk transport becomes negligible and the effect of wall transport becomes dominant in the platform, which is called the SC regime. Conversely, as the depth of the microchannel increases, the effect of bulk transport increases so that the ions are transported by both wall and bulk transport, which is called the EOF regime. Finally, when the microchannel depth becomes extremely high, the effect of bulk transport becomes dominant and

the wall transport becomes negligible in the platform so that the platform eventually lies in the EOI regime. These mechanisms would be discussed later in Chapter 2.

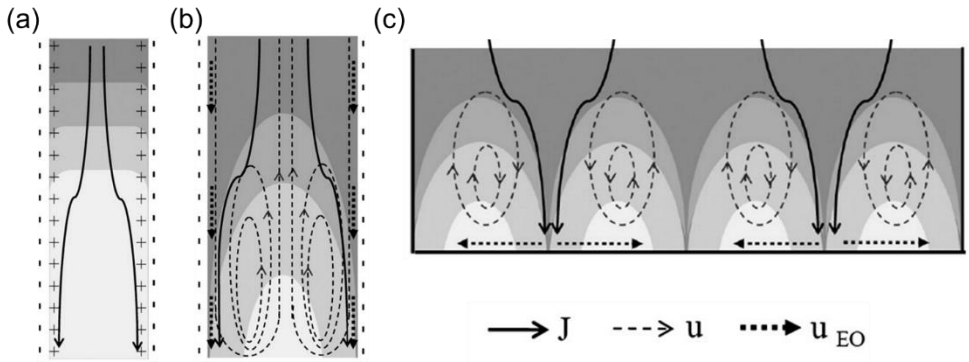

Figure 1.3. The schematic diagram of the mechanisms of ion concentration polarization: (a) surface conduction, (b) electroosmotic flow and (c) electroosmotic instability[5].

1.2.2 Electroconvection

In the EOI regime, the ions are transported through the vortices formed in IDZ like the EOF regime. However, unlike the vortices are formed by the EOF at the wall in EOF regime, the vortices are formed by the EOF induced at the surface of the ion exchange membrane in EOI regime, which is called electroconvection. EOF induced at the membrane surface is determined by the competition of two mechanisms: Dukhin's mode and Rubinstein's mode[6].

When the membrane is heterogeneous (i.e. undulated surface or impermeable patterns on membrane surface), EOF at the membrane surface is formed in specific directions and positions by the focused electric field induced by the membrane heterogeneity. Due to the EOF parallel to the direction of the membrane surface and mass conservation, vortices are formed in specific directions, which is called Dukhin's mode[7].

On the other hand, electroconvection occurs even when the ion exchange membrane is homogeneous. When IDZ initiates, small fluctuations in the extended space charge layer occur randomly. The fluctuation induces the electric field in the direction parallel to the membrane. Then EOF is induced in the direction of the tangential electric field. Above a critical threshold voltage, the EOF increases the size of fluctuation and a large vortex is formed in consequence of positive feedback, which is called Rubinstein's mode[8].

As the applied voltage across the membrane increases, the formation of electroconvection in Rubinstein's mode becomes more active and the electroconvection in IDZ becomes unstable, which is called the chaotic regime. In chaotic regime, has been reported that the current value fluctuates due to the

instability in electroconvection which contributes to the ion transport[9-11]. The detailed study using electroconvection would be discussed in Chapter 2 and 3.

1.3. Diffusiophoresis

Diffusiophoresis refers to the spontaneous motion of particles in an electrolyte with a concentration gradient[12, 13]. The diffusiophoretic migration of particles is caused by two mechanisms. The first one is called chemiphoresis. When a charged particle exists in electrolyte, an EDL is formed around the particle due to the surface charge of the particle in the same way of a channel wall described in section 1.1. If concentration gradient is formed in the electrolyte, EDL on the higher concentration side of the particle becomes shorter than one on the lower concentration side due to the dependence of Debye length and ion concentration as shown in Figure 1.4 i. In the case of a negatively charged particle, the charge density becomes higher in the higher concentration side. Consequently, an electric field is induced by the nonuniform distribution of charge density as shown in Figure 1.4 ii. Then, as shown in Figure 1.4 iii, the particle is moved by the electric field, and the movement is called chemiphoresis[14]. The other mechanism is an induced electrophoresis by the difference of cation's and anion's diffusion through an electrolyte with the concentration gradient29. However, in this thesis, the induced electrophoresis was not considered since induced electrophoresis was negligible compared to chemiphoresis. The detailed study utilizing this phenomenon would be explained in Chapter 4.

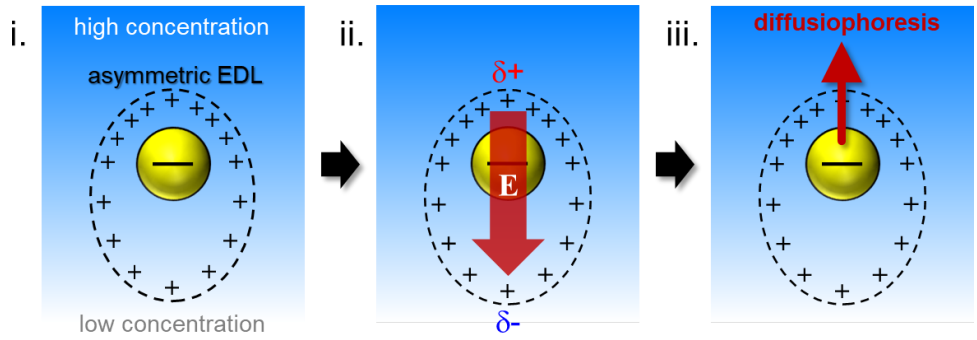

Figure 1.4. The schematic diagram of the mechanism of diffuiophoresis. i. Formation of asymmetric EDL due to concentration gradient in electrolyte. ii. Electric field induced by nonuniform charge distribution. iii. Diffusiophoretic migration of particle.

Chapter 2. Adhesive Lift Method for Patterning Arbitrary-shaped Thin Ion-selective Films in Micro/nanofluidic Device

2.1. Introduction

A micro/nanofluidic platform has been often employed as a fundamental research tool, because it has a number of superior points to a traditional platform. For example, one can easily perform unit operations such as feeding nutrient to cells[15], washing buffer solutions[16, 17], precise controlling pH[18, 19] and implementing mechano-transductions[20], etc. Among these benefits, we would like to focus on direct visualization. Due to the excellent scalability of the platform, one may build a high-throughput application by "integral" of the platform[21, 22]. Reversely, a high-throughput application, which one cannot observe incidents inside, can be "differentiated" into a micro/nanofluidic shell[23]. Furthermore, the platform is usually built with a transparent substrate so that one can directly observe incidents inside the small-scale world[4]. Consequently, one can study an operation in a macro-scale system without building the macro system by itself. Representing example of such a way is studying an electro-desalination system based on ion concentration polarization (ICP) which is different from the traditional desalination method such as reverse osmosis. Desalination typically refers to the techniques which pure water can pass through and salts are mostly rejected to pass through the ion-selective membranes. Compared to this, ICP desalination method doesn't need

for water to pass through the membrane. Charged impurities can be removed from brine by the repulsive force of ion depletion zone (IDZ) that was developed due to a rapid proton hopping through ion selective films. Note that small-throughput desalination/purification strategies were studied by ourselves, for example, spontaneous diffusiophoretic purification by ion exchange of Nafion and an artificial kidney device by ICP purification mechanism extended with 3D printing[24-27]. Another representing example of electro-desalination is electrodialysis (ED) which utilizes both anion selective- and cation selective- membranes[28, 29]. It is extremely hard to watch *in operando* operation of such macro-scale desalination devices, but a micro/nanofluidic ICP platform enables to tell us a number of interesting stories about electroconvective instability, mechanism of overlimiting current and ion separation, *etc*. by the direct visualization[29]. In such studies, ion selectivity is the key feature to be utilized for removing impurity.

Ion selectivity described in section 1.1 refers to a phenomenon in which only either cations or anions can freely move in the region where electrical double layers overlap each other. The electrical double layer is a layer formed at the surface of a channel in a nanometer-scale by the surface charge of the channel[1]. In order to induce ion selectivity, the channel requires to be fabricated in a nanometer-scale so that the electrical double layers in the channels to be overlapped. Therefore, in conventional micro/nanofluidic platforms, nanoscale structures have been implemented in various ways to induce ion selectivity.

One of the methods is constructing a nanochannel on the main substrate such as glass or silicon with employing a semiconductor manufacturing process[30-32]. This method allows the fabrication of the nanochannels with precise positions and shapes. However, since a complex and sophisticated semiconductor manufacturing process

is employed, the process takes a long time and high cost to fabricate the nanochannels. In addition, the ion selectivity is low because the surface charge of the substrate is significantly low compared to the concentration of the buffer solution[33, 34]. Thus, salt removal has not been accomplished in electro-desalination system assembled with nanochannels when the ion concentration of brine solution is high. Consequently, the nanochannels have been replaced with highly-charged nanoporous membranes in previous researches.

In the case of nanoporous membranes consisting of polymeric components such as Nafion, nanostructures are formed due to random arrangement of molecular structures in the form of pores in the nanometer scale, unlike lithographical fabrication of nanochannels[3]. Since the surface charge of the Nafion film is significantly higher than that of the nanochannels made of glass or silicon, the ion selectivity is maintained even when the ion concentration of the buffer solution is high. For example, the Donnan concentration of Nafion is three-time higher than seawater concentration so that one would able to expect nanofluidic phenomenon in seawater solution with Nafion-based platform[35, 36]. Additionally, the soft-lithographical fabrication using Nafion solution is very simple and low-cost compared to the direct implementation of nanochannels[4, 37, 38]. However, since the cutting and assembling are performed manually, the position of the Nafion film cannot be accurately determined and the shape has been limited[35]. Thus, the platforms with ion selective films still have limitations in terms of dissimilarity to practical macro-scale systems. While the system may involve spacers between membranes or uneven surface of the membrane, *etc*.[39-41], the up-to-date soft-lithographical nanofabrication method of micro/nanofluidic platform has unable to reflect those features. Therefore, we propose a nanoporous film fabrication method

which enables the fabrication of a micro/nanofluidic network as similar as a realistic system.

In this chapter, the fabrication was carried out in the following process. First, a microchannel block was treated with oxygen plasma treatment to increase the wettability of the surface to be coated with nanoporous film. Then, the film was patterned by spin coating Nafion in the intended area. Subsequently, the Nafion film in the unintended area was detached with the adhesive lift method. Using the method, nanoporous films were successfully patterned along the arbitrarily-shaped boundaries of the microchannels with various waveform shapes and depth of the microchannel could vary from 5 μm to 150 μm, which is a conventional range of practical micro/nanofluidic system.

The operation of films was demonstrated by direct visualization of ICP. In particular, the mechanisms of ICP are divided into three types mainly depending on the characteristic length scale of the fluidic components[5]. The mechanism corresponding to surface conduction (SC) was observed through the device with a depth of $O(1)$ μm, electroosmotic flow (EOF) through the device with a depth of $O(10)$ μm, and electroosmotic instability (EOI) through the device with a depth of $O(100)$ μm. Through a direct visualization, we confirmed that an IDZ extends in the direction perpendicular to the electric field regardless of the shape of the microchannel boundary in the SC regime and EOF regime. However, in the case of the EOI regime, we observed that as the wavelength of the waveform at the boundary of the ion selective film was shorter, IDZ was formed at the position of the trough of the waveform, and the zone was expanded from the position. These visualizations associated with the electrical measurement of overlimiting conductance lead that overlimiting conductance is independent of the shape of the ion selective film in the

EOF regime, while it significantly depends on the shape of it in the EOI regime. Also, we confirmed that overlimiting current regime easily initiates with the undulated film especially in EOI regime. In conclusion, here we present a simple but useful soft-lithographical nanofabrication method that can pattern a highly charged nanoporous film at a precise location along the arbitrary shaped microchannel boundary. The presenting method would be an effective way to fabricate a realistic micro/nanofluidic system as close as possible.

2.2. Methods

2.2.1. Fabrication of Micro/Nanofluidic Device with Arbitrary-shaped Membrane

Figure 2.1. showed the schematic process of fabricating a micro/nanofluidic device incorporated with arbitrary-shaped nanoporous membrane. Detailed descriptions of each step were elucidated as follows.

(i) Preparation of microchannel network

The targeting device developed in this chapter was fabricated by sandwiching an ion exchange membrane between a microchannel block and a slide glass. The microchannel block was prepared by soft lithographical process. First, microchannel structure was patterned on a silicon wafer with SU8 photoresist (Microchem, USA). While nanochannels are connected to microchannels in lithographical nanofabrication, only microchannels are patterned on the master in the case of soft lithography and, then, the microchannels are connected later by nanoporous membrane. Therefore, only two microchannels were patterned on the polydimethyl-siloxane (PDMS) block as shown in Figure 2.1(i). One of the microchannels is a ground channel connected to a cathode, and the other microchannel is a main channel connected to an anode. Since IDZ is formed in the main channel, one of main channel's edge was designed in an arbitrary-shape shown in Figure 2.1(i).

After preparation of the master, PDMS polymer solution was prepared by mixing PDMS base and curing agent (Sylgard 184 silicone elastomer kit, Dow Corning, USA) in a ratio of 10:1. Then, the mixed PDMS solution was degassed in a vacuum

chamber for 1 hour to prevent the formation of the air bubbles in the microchannel block. After degassing, the PDMS solution was poured on the master and baked in the oven at 75ºC for 5 hours. The cured PDMS was detached from the master and cut into a block with a razor blade. Then, the PDMS block was punched at positions of reservoirs with a biopsy punch.

(ii) Masking with adhesive tape for plasma treatment

The nanoporous film in the targeting device was designed to connect microchannels at the position where the edge of the main channel is undulated. Therefore, the film was positioned only on the region between the ground channel and main channel. In addition, the microchannel regions were also coated with Nafion. Since the main channel is undulated in a microscale and the masking tape was attached manually, the masking of the microchannel regions cannot be performed precisely. Hence, the excess amount of film was covered on the entire device and the excess film was removed later by adhesive tape. Except for that intended area, the reservoirs should be covered by adhesive tape (3M, USA) to prevent leaking a Nafion solution (Sigma Aldrich, USA). This Nafion solution will be the nanoporous film after drying the solvent of it as shown in Figure 2.1(ii).

Then, the masked PDMS block was exposed to oxygen plasma (CuteMP, Femto Science, Republic of Korea) with a power of 50 W for 6 sec to increase adhesion between the block and the Nafion film. Plasma treatment is known to increase the wettability of a surface. In particular, it has been reported that the PDMS surface becomes hydrophilic and the contact angle decreases when plasma treatment is performed on the surface[42]. Therefore, if oxygen plasma was not treated on the PDMS surface, the nanoporous film was not fully coated up to the microchannel boundary as shown in Figure 2.2(a)-i. On the other hand, in the case of plasma-

treated surface, Nafion was coated up to the arbitrary boundary of the undulated microchannel as shown in Figure 2.2(a)-ii.

(iii) Spin coating of Nafion solution to form a nanoporous film

After plasma treatment, the PDMS block was placed on a silicon wafer, and then 100 μL of 20% or 5% Nafion solution was dropped on the plasma-treated surface of the block. 20% and 5% Nafion solution was utilized for the microchannel depth above 15 μm and below 15 μm, respectively (Figure 2.1(iii)). The 5% Nafion solution was prepared by diluting the 20% Nafion solution with isopropyl alcohol (Sigma Aldrich, USA, 99.5%). After dispensing the Nafion solution, the block was pre-spun at 500 rpm for 10 sec with acceleration at 100 rpm/s to spread the Nafion on the entire surface of the block. Then, the spin speed increased to 4000 rpm with the acceleration at 300 rpm/s and kept for 30 sec. After the spinning at 4000 rpm, the rotation was dropped to zero with a deceleration at 800 rpm/s. When the block was coated with 20% Nafion solution, a thicker Nafion film was coated than one with 5% Nafion solution. The thicknesses of Nafion films were measured with a profilometer (Alpha-step 500, Tencor Instruments, USA) and the thicknesses of films which were coated with Nafion 5% and Nafion 20% solution were measured as 0.58 μm and 4.22 μm, respectively. If 20% Nafion solution was used for a microchannel depth less than 15 μm, the film would not be clearly removed along the microchannel boundary as shown in Figure 2.2(b)-i. Hence, 5% Nafion solution should be used for microchannels of depth less than 15 μm. As a result, even in the case of a thin microchannel, Nafion film was successfully left along the arbitrary shaped microchannel boundary as shown in Figure 2.2(b)-ii.

One can concern about the step coverage of the films coated with spin coating.

However, reasonable step coverage is guaranteed since the dispensing of 100 μL Nafion solution can almost fully cover the intended area and the neighboring microchannel area. The spin coating process was employed just for the uniform and thin film thickness. Furthermore, even if the step coverage is poor, it could be neglected because the Nafion film on the microchannel area is removed after the '(vi) Removal of unnecessary film with adhesive tape' step.

(iv) Detachment of masking tape

The masking tapes attached before the plasma treatment was removed after the Nafion coating (Figure 2.1(iv)). Then, the Nafion film was left on the intended area and the microchannel inside. If the film inside the microchannel is not removed, the ions in the buffer solution are transported through the membrane remained on the wall rather than the buffer solution in the microchannel when the ion concentration of the buffer solution is lower than 30 mM. Therefore, the films on the microchannel inside should be removed by the adhesive lift method described in the next step.

(v) Attachment of tape for adhesive lift

To prevent damaging the film on the intended area after removing the films on the microchannel inside, another adhesive tape were attached to the block parallel to the microchannel. Note that the edge of the tape is located in the middle of the microchannel as shown in Figure 2.1(v). Then, the attached tapes were adhered only to the films on the microchannel regions and not adhered to the films on the intended area as shown in a cross-sectional view of Figure 2.1(v).

(vi) Removal of unnecessary film with adhesive tape

Since there is a height difference between the film on the intended area and the film on the microchannel inside, they are disconnected as shown in the cross-sectional view of Figure 2.1(v). Therefore, the Nafion films coated inside the patterned

microchannel can be removed with the attached tape, without damaging the membrane on the intended area as shown in Figure 2.1(vi). Thus, the presenting fabrication method must coat the Nafion on the PDMS block with a microchannel network so that the Nafion film can be cut with the shape of complex microchannel edge. In the case of the spinning of Nafion on the flat glass slide, the shape of Nafion film edge would be just flat. Also, the position of the membrane in the fabricated platform would be imprecise since the micro/nanofluidic platform is assembled manually. Furthermore, the Nafion films should be precisely patterned along the microchannel edge so that the additional effects due to the overlap of the film area and the microchannel area studied by ourselves[35] can be neglected.

(vii) Plasma treatment on the film

The Nafion film only on the intended area was left along the edge of both microchannels. Therefore, the shape of the film should follow the shape of microchannel edge, *i.e*. arbitrary shaped edge. After removing the adhesive lift tape, the Nafion-coated PDMS block was treated with oxygen plasma with a power of 50 W for 50 sec as shown in Figure 2.1(vii). Since the oxygen plasma in this step was treated for the bonding, the exposure time was longer than the treatment for the increase of wettability in step (ii).

(viii) Flip and bonding the PDMS block to a glass slide

The treated PDMS block was flipped and bonded to a slide glass as shown in Figure 2.1(viii). For the bonding, the slide glass was also exposed to oxygen plasma with a power of 50 W for 50 sec. After bonding, the micro/nanofluidic device was baked at 95ºC for 5 hours to increase the bond strength between the glass and the microchannel block. Then finally, the microchannels were filled with electrolyte and Ag/AgCl electrodes were inserted to the reservoirs for applying external voltage.

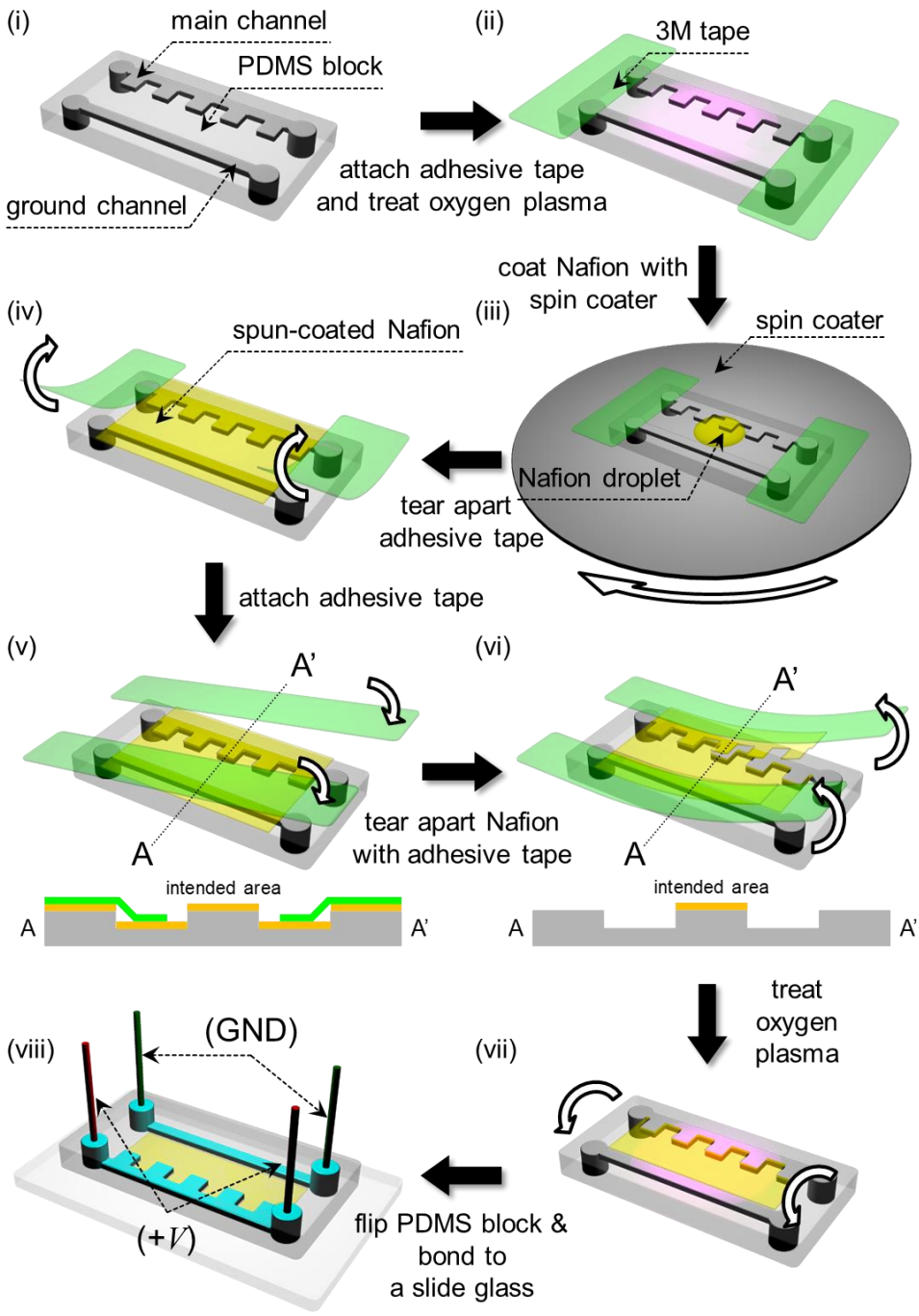
(i)
main channel
PDMS block
ground channel
(ii)
3M tape
attach adhesive tape
and treat oxygen plasma
coat Nafion with
spin coater
(iii)
spin coater
Nafion droplet
(iv)
spun-coated Nafion
tear apart
adhesive tape
attach adhesive tape
(v)
A'
A
intended area
A
A'
tear apart Nafion
with adhesive tape
(vi)
A'
A
intended area
A
A'
treat
oxygen
plasma
(vii)
flip PDMS block &
bond to
a slide glass
(viii)
(GND)
(+V)

Figure 2.1. The schematic diagram of the fabrication process of the micro/nanofluidic platform with arbitrary-shaped nanoporous film. (i) Preparation of microchannel network. (ii) Masking with adhesive tape for plasma treatment. The PDMS block was treated with oxygen plasma to increase wettability of the block. (iii) Spin coating of Nafion solution to form a nanoporous film. The Nafion solution was coated with spin coater for uniform thickness of the Nafion film. (iv) Detachment of masking tape. (v) Attachment of tape for adhesive lift. The tape as attached for adhesive lift of the nanoporous film on the microchannel area. (vi) Removal of unnecessary film with adhesive tape. (vii) Plasma treatment on the film. (viii) Flip and bonding the PDMS block to a glass slide.

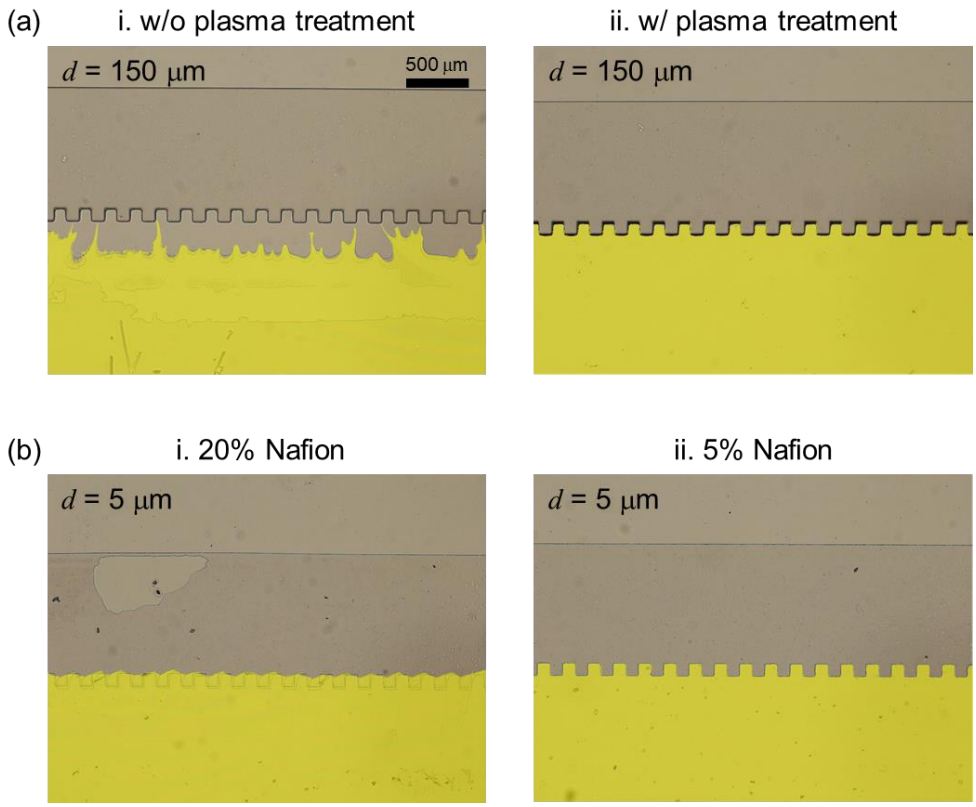

Figure 2.2. (a) The nanoporous film (colored in yellow) coated along the microchannel with 150 μm depth in case of the microchannel block is i. not treated with oxygen plasma and ii. treated with oxygen plasma. The film was not completely coated on the intended region when oxygen plasma is not treated on the block while the film was completely coated along the microchannel block with plasma treatment. (b) The nanoporous film coated along the microchannel with 5 μm depth in case of the coated polymer solution is i. 20% Nafion and ii. 5% Nafion. The Nafion film on the microchannel region was not removed accurately when 20% Nafion was coated on the block while the film was removed along the boundary of the microchannel when 5% Nafion was coated on the block.

2.2.2. Chemicals and Experimental Setup

To show the expandability of our adhesive lift method, poly(3,4-ethylenedioxythiophene) polystyrene sulfonate (PEDOT:PSS) 3-4% in H_2O (Sigma Aldrich, USA) was also used. All of the above fabrication steps in Figure 1 were applied to PEDOT:PSS, except conditions in step (ii) and (iii). In step (ii), the PDMS block was exposed to oxygen plasma with a power of 50 W for 15 sec so that the PEDOT:PSS film was fully coated on the block. In step (iii), the PEDOT:PSS solution was coated with a spin speed of 500 rpm and the spread solution was dried at room temperature for 10 minutes. This spin coating process was repeated twice in succession to increase the thickness of the PEDOT:PSS film.

For visualization experiments, 1 mM KCl (Sigma Aldrich, USA) + 100 μM Sulforhodamine B (Thermofisher, USA) solution was utilized as buffer solution. Before the injection of the buffer solution, the devices were degassed for 30 minutes to prevent the formation of the air bubbles in the microchannel. To induce ICP in the microchannel, external voltage (source measure unit, Keithley 236, USA) was applied with connecting Ag/AgCl electrodes to buffer solution. The anode and cathode were connected to the main channel with the undulated surface, and the ground channel on the opposite side, respectively. For direct visualization of ICP, the repulsion of the fluorescent dye in IDZ was recorded under an inverted fluorescence microscope (IX53, Olympus, Japan) and the CellSens program (Olympus, Japan).

For an I-V measurement, the currents were measured by applying constant voltage for 10 minutes to ensure that IDZ inside the main channel is fully developed. Then the next voltage was applied. This process was iterated from 1 V to 10 V at the interval of 1 V, except 0.5 V as an initial point. Simultaneously, the buffer solution

was continuously injected through the ground channels by a syringe pump (Fusion 100, Chemyx, USA) to maintain a constant bulk electrolyte concentration. The flow rate was 0.5 μL/min and 0.1 μL/min for the channel depth of 150 μm and 15 μm, respectively.

2.3. Results and Discussion

2.3.1. Arbitrary-shaped Nanoporous Membrane along the Main Channel

First result was the fabricated device. Micro/nanofluidic devices with the various arbitrary-shaped nanoporous films were fabricated for demonstrating our fabrication method. As shown in Figure 2.3(a), the Nafion film was patterned between main and ground channel, and one side of the membrane along the main channel was undulated in waveform shape. As shown in Figure 2.3(b), the sides of main channel were undulated in the shape of square, sine, sawtooth, triangle, and fractal-shaped (4^{th} order Koch curve) waveforms. These various shapes were designed to demonstrate that the nanoporous films can be patterned in arbitrary shapes using the presenting fabrication method. Furthermore, as shown in Figure 2.3(c) and 2.3(d), micro/nanofluidic devices with PEDOT:PSS films were also fabricated to demonstrate the expandability of the presenting patterning method. To ensure that the films were accurately patterned, *in situ* visualization of ICP (or an IDZ) was conducted. A charged fluorescent dye would be repelled from the membrane if the nanoporous membrane properly worked. The results in main channel with various shapes of waveform and microchannel depths were followed in the next section.

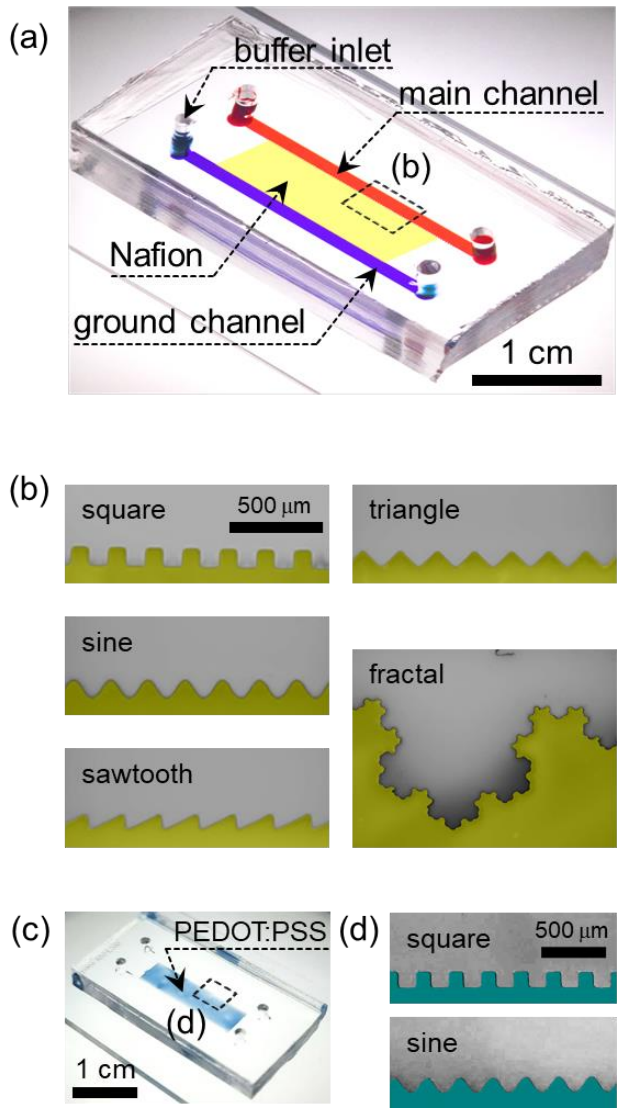

Figure 2.3. (a) Image of the device experimented for the visualization of ICP in the microchannels with arbitrary-shaped nanoporous films. (b) Images at the boundaries of the main channels and the nanoporous films which were patterned along the main channels with square, sine, sawtooth, triangle and fractal waveform shape. (c) Image of the device with PEDOT:PSS films. (d) Images at the boundaries of PEDOT:PSS films and the main channels with square and sine waveform shape.

2.3.2. An IDZ along Arbitrary-Shaped Membrane

As mentioned in section 1.2, when an electric field is applied across a nanoporous membrane (Nafion or PEDOT:PSS in this chapter), only counter-ions can pass through the membrane due to the ion-selectivity. Whereas, co-ions are expelled from the membrane to satisfy electroneutrality. Consequently, the ion concentration on the anodic side of the membrane sharply reduces to form an IDZ in the case of a negatively charged membrane. Inside IDZ, charged particles or charged molecules including fluorescent dyes are also rejected to maintain electroneutrality[43]. Since IDZ generates at the surface of the membrane, the fluorescent molecules are repelled from the edge of Nafion. Therefore, observing the initiation of IDZ from the edge of the membrane would be key evidence of conformal patterning of the film. If the film was not conformally patterned, IDZ formed irregularly as shown in Figure 2.4(a) and 2.4(b). In both cases, Nafion was partially patterned along the edge of the main channel so that IDZ would not grow from the black area where Nafion was failed to be patterned. Note that the film was intentionally removed in Figure 2.4(a) and a plasma treatment shown in Figure 2.1(ii) was not implemented in Figure 2.4(b). Therefore, we demonstrated the successful patterning by examining the growth of IDZ from the entire edge of the membrane, but IDZ expands in several ways as shown in Figure 2.4(c). The appearance of IDZ expansion mainly differs as a function of the depths of the microchannels (d), if width and length are much larger than depth. The difference is resulted by the dominant mechanism of overlimiting conductance.

In the early stage of electrokinetic study about the overlimiting conductance, electric current through a nanoporous membrane was predicted to be saturated to a

constant value due to the decrease of the ion concentration in the anode side, which is called a limiting current[44]. However, it has kept to be reported that the current increases over the limiting current regime as a function of the applied voltage. Under this circumstance, the current exceeds the limiting current, called overlimiting current. Thus, the slope of the overlimiting current as a function of applied voltage would give a overlimiting conductance. While several mechanisms have been suggested, Bazant *et al* mainly categorized the mechanism for overlimiting conductance as SC, EOF and EOI[5]. Whether SC, EOF or EOI is the main mechanism of overlimiting conductance in an ICP platform is determined by the medium of ion transport. In a microfluidic channel, ions are mainly transported either by wall transport or bulk transport. The characteristic length scale of the microchannel is the main factor for determining the proportion of wall transport in the total ion transport. If the width and length of the microchannel are sufficiently long, convection in the microchannel is suppressed as the microchannel depth decreases so that the effect of bulk transport becomes negligible and the effect of wall transport becomes dominant in the platform, which is called the SC regime. Conversely, as the depth of the microchannel moderately increases, the effect of bulk transport increases so that the ions are transported both by wall and bulk transport, which is called the EOF regime. Finally, when the microchannel depth becomes extremely large, the effect of bulk transport becomes dominant and the wall transport becomes negligible in the platform so that the platform eventually lies in the EOI regime. In the case of electrolyte of 1 mM KCl solution, the characteristic length scales to determine SC, EOF, and EOI regime are $O(1)$ μm, $O(10)$ μm, and $O(100)$ μm, respectively[45, 46]. Therefore, for the observation of each mechanism, the devices with various depths (5 μm, 15 μm and 150 μm) were fabricated and IDZs in

each device were visualized as shown in Figure 2.4(c). Since the experiments used the buffer solution as 1 mM KCl solution, 5 μm belongs to the SC regime, 15 μm to the EOF regime, and 150 μm to the EOI regime, respectively.

In the case of the microchannels with 5 μm or 15 μm depths, the fluorescent particles started to be repelled from the edge of the microchannel in specific shapes according to the microchannel shapes at time t = 0.25 s as shown in "square", "sine" and "sawtooth" of Figure 2.4(c). Since the ion transport is dominantly affected by side walls in SC and EOF regime (relatively free from complex fluid motion), IDZs stably expand along the side walls. Therefore, the expansion of IDZ was stable over time and the boundary of IDZ became perpendicular to the direction of the applied electric field at t = 2 s. One small difference observed in the case of d = 15 μm was the appearance of vortices at t = 2 s. Since a convective flow was not completely suppressed in EOF regime, the remnant electroosmotic flow would interact with the undulated surface so that fluorescent dye would accumulate on specific locations as shown (Figure of 2.4(c) of t = 2 s of d = 15 μm). On the other hand, the bulk transport becomes dominant in the microchannel depth of 150 μm. In this EOI regime, the formation of IDZ is determined by the competition of EOF between two modes: Rubinstein's mode and Dukhin's mode[6]. In Rubinstein's mode, small fluctuations in the extended space charge layer randomly occur when IDZ initiates, and EOF is induced by the local expansion of the extended space charge layer[8]. On the contrary, when the membrane is heterogeneous (*i.e.* undulated surface or impermeable patterns on membrane surface), EOF in IDZ is formed in specific directions and positions by the focused electric field induced by the membrane heterogeneity, which is called Dukhin's mode[7]. Therefore, IDZ was initially

formed by Dukhin's mode at the position of the trough of the waveform in the microchannels with 150 μm depth at t = 0.25 s as shown in "triangle" and "fractal" of Figure 2.4(c). However, when Rubinstein's mode becomes dominant in IDZ formation (*i.e*. fluctuation of extended space charge layer), the expanded IDZ shows unstable fluidic motion. Hence, as shown in t = 2 s, IDZ was expanded from the trough position and soon deformed to an irregular shape in the EOI regime.

Furthermore, the successful patterning of arbitrary-shaped PEDOT:PSS film was demonstrated through the direct visualization of the expansion of IDZ. As shown in Figure 2.5, the IDZ inside microchannels with square and sine wave shaped edge was formed and expanded from the trough positions of the PEDOT:PSS films. Therefore, we could confirm that the PEDOT:PSS films were also successfully patterned along the arbitrary-shaped microchannels, as similar as in the case of Nafion films. Consequently, it was demonstrated that the presenting fabrication method can be applied not only to Nafion but also to general nanomaterials if the materials exist in a liquid state.

In summary, the direct visualizations of ICP phenomenon in all SC, EOF and EOI regimes were successfully accomplished using the micro/nanofluidic platforms with the arbitrary-shaped nanoporous films. Furthermore, using the presenting fabrication method, one can visualize the operation of electro-desalination processes in the platform which includes practical structures of the nanoporous membranes. This will be elucidated in the following section with the relationship of overlimiting conductance.

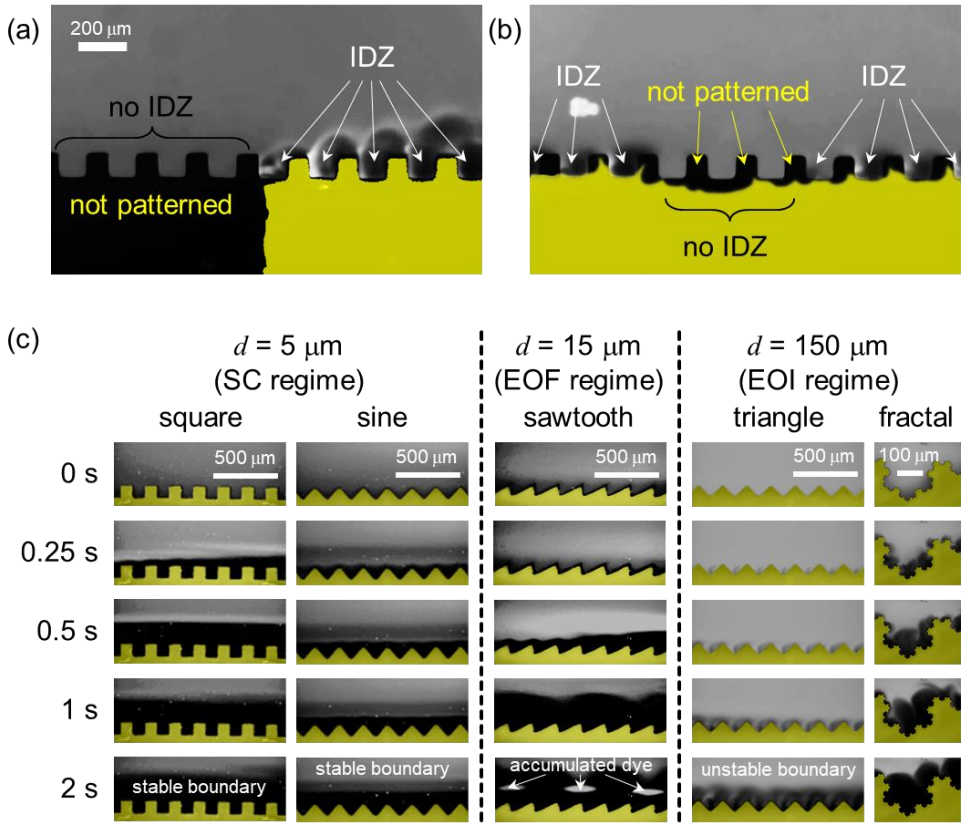

Figure 2.4. Snapshots of IDZ visualized by the repulsion of the SRB fluorescent dye (colored in white gray) when the nanoporous film was (a) partially patterned and (b) patterned without plasma treatment in step of Figure 2.1(ii). (c) Snapshots of IDZ initiated at the main channel boundaries with square, sine wave shape in SC regime (5 μm depth), sawtooth wave shape in EOF regime (15 μm depth), and triangle, fractal wave shape in EOI regime (150 μm depth). Each series of the snapshots were captured from a single video at times of 0 s, 0.25 s, 0.5 s, 1 s and 2 s.

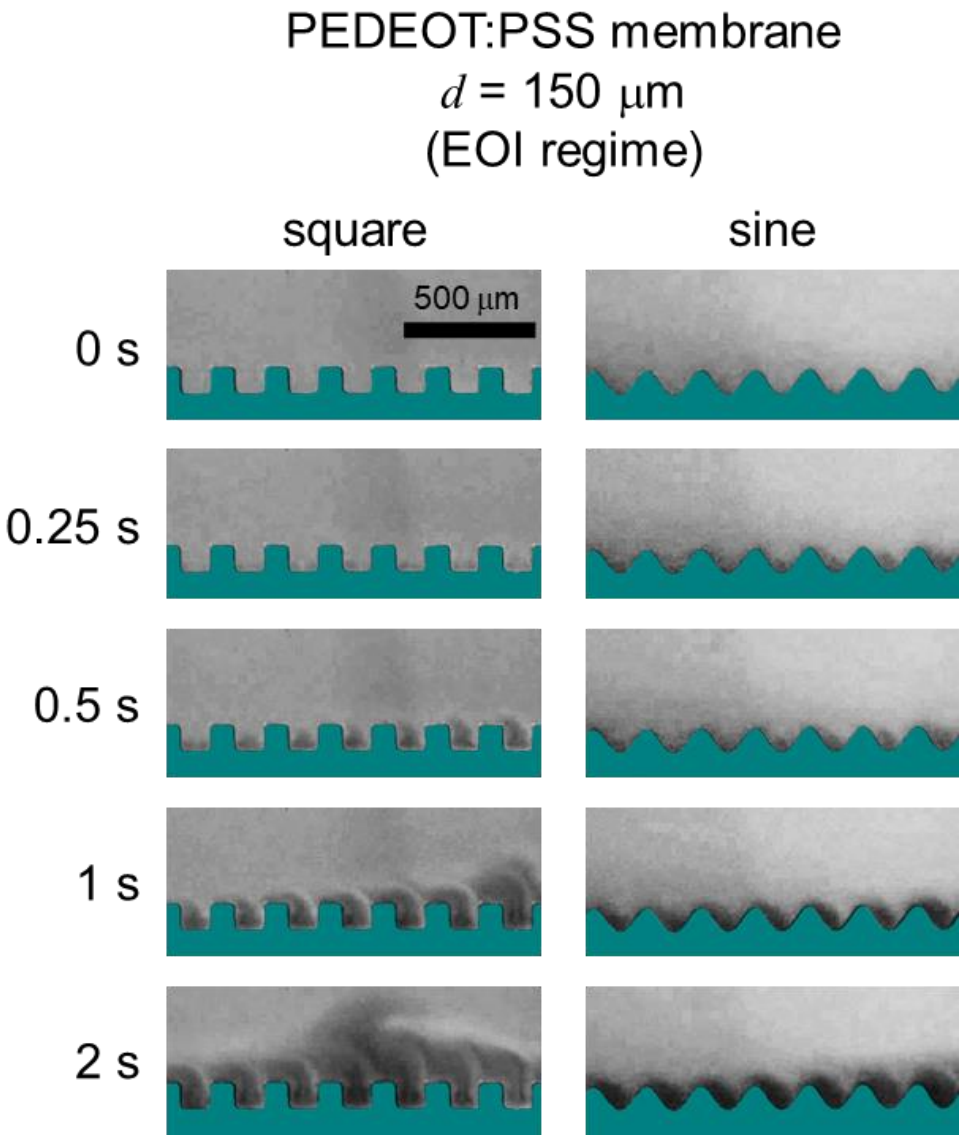

Figure 2.5. Snapshots of IDZ initiated at the boundaries between PEDOT:PSS films and main channels with square and sine wave shape in EOI regime.

2.3.3. Near-practical Electro-desalination Platform using the Arbitrary-shaped Membrane

2.3.3.1. Device Configuration

The ion exchange membranes in the practical electro-desalination systems include additional structures which are not implemented in micro/nanofluidic platforms in previous researches. The examples of the additional structures include a support structure for the maintenance of the physical structure of the practical membrane or a spacer structure for prevention of electrical short between the membranes[39, 47]. Despite the effects of these structures have been reported[48], the structures have been minimally mimicked in previous micro/nanofluidic platforms due to the limitation in fabrication techniques. One of the critical aspects of those structures is that the surfaces of the commercial ion exchange membranes are undulated, unlike the previous studies that assumed the shape of a nanoporous membrane to be flat[40]. However, the undulated membrane can be fabricated with the presenting arbitrary-shaped membrane patterning technique as demonstrated in the previous section. Therefore, in order to mimic the operation of the near-practical membrane on a micro-scale, a micro/nanofluidic device with a nanoporous membrane undulated in the shape of a sinusoidal wave was fabricated as shown in Figure 2.6(a). The nanoporous membrane was patterned along the undulated main channel and the ground channel as shown in Figure 2.6(b), simulating a rough surface of a practical membrane. Here Q is the flow rate of fresh electrolyte through the buffer channel and the ground channel. It was 0.5 μL/min and 0.1 μL/min for the case of main channel depth of 150 μm and 15 μm. In addition, a spacer structure was implemented between the main channel (200 μm width × 2 mm length × either 15 μm or 150 μm

depth) and the buffer channel. For the electric conduction and ion transportation between the main and buffer channel, an array of microchannels between the spacers connects the main and buffer channel. The dimension of the connecting microchannel is 15 μm width, 100 μm length and either 5 μm or 15 μm for main channel depth of 15 μm or 150 μm, respectively. The depth of 15 μm and 150 μm represented EOF and EOI regime, respectively. Since the sizes of the connecting microchannels are much smaller compared to the size of the main and buffer channel, the hydraulic resistance of the connecting microchannel is $O(10^3)$ times higher than the ones of the main channel and the buffer channel. Therefore, the convection in the buffer channel and the convection in the main channel is separated, unlike the real system. However, the separation of convection prevented the expansion of IDZ from the main channel to the buffer channel. Consequently, the effect of the waveform of the nanoporous membrane surface on IDZ in the main channel can be solely visualized.

For the generation of IDZ, a voltage was applied to both ends of the buffer channel, and the ground at both ends of the ground channel using Ag/AgCl electrodes. Simultaneously, the buffer solutions were continuously injected through buffer and ground channel using a syringe pump. Therefore, the ion concentration at the boundary between the main channel and the buffer channel was maintained as the known concentration of the buffer solution.

To evaluate the effect of the smoothness of the membrane on ICP formation, the boundary of main channel was undulated in the form of sine waves with wavelengths (L) of 100 μm, 200 μm, 500 μm, 1000 μm and ∞(flat) as shown in Figure 2.6(c). For all cases, the amplitude of the sine wave was kept to be 25 μm.

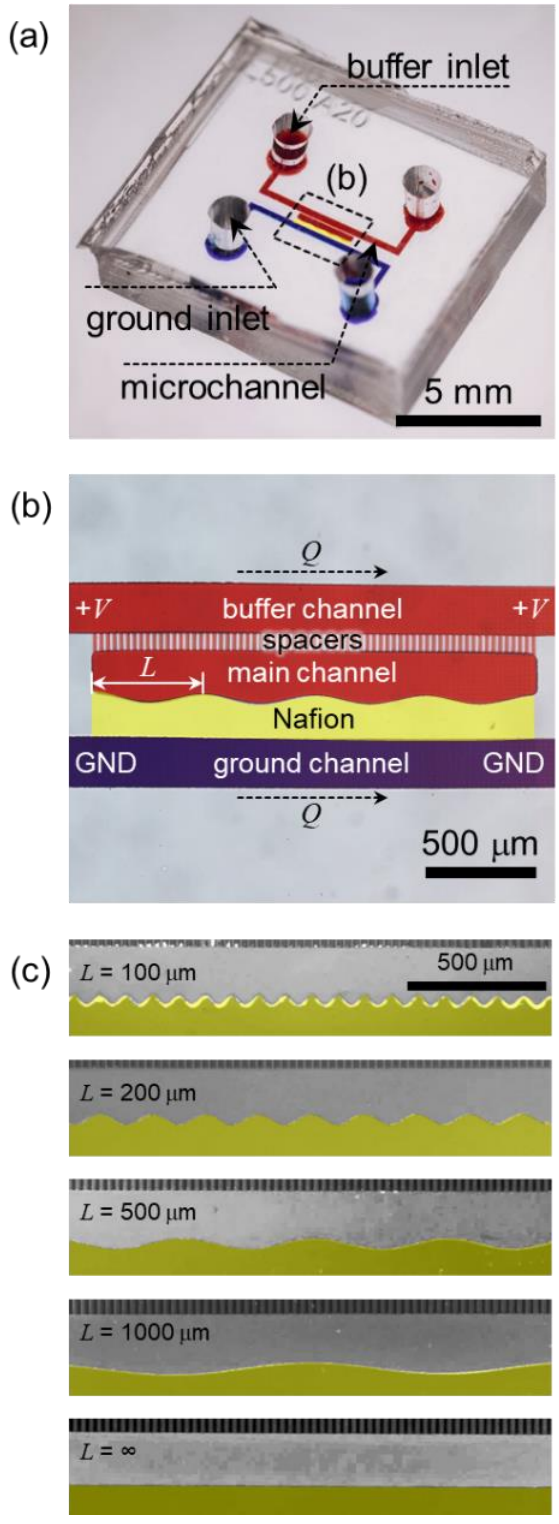
(a)
buffer inlet
(b)
ground inlet
microchannel
5 mm
(b)
Q
+V
buffer channel
+V
spacers
L
main channel
Nafion
GND
ground channel
GND
Q
500 μm
(c)
L = 100 μm
500 μm
L = 200 μm
L = 500 μm
L = 1000 μm
L = ∞

Figure 2.6. (a) Image of the device experimented for operation of the electro-desalination platform with the spacer structure and the undulated surface. (b) The zoomed image of the experimented device. The voltage was applied across the nanoporous membrane with continuous injection of the buffer solution into buffer channel and ground channel. The main channel was connected to the buffer channel with an array of thinner and shallower microchannels compared to the main and buffer channels. The Nafion membrane was patterned on the region between the main channel and the ground channel. The surface of the main channel was undulated in the shape of sine wave with wavelength of L. (c) Images at the boundaries of microchannels and nanoporous membranes which are patterned along microchannels with wavelength of 100 μm, 200 μm, 500 μm, 1000 μm and ∞(flat). The wave height of each wave was fixed to 50 μm.

2.3.3.2. Direct Visualization of IDZ in Near-practical Electro-desalination Platform

In the case of the EOI regime, IDZs were spaced apart from each other due to dominant bulk transport as shown in Figure 2.7(a), called fingering. Since the amplitude of the undulations are the same, the local slope of the membrane surface, which can be estimated as wave height divide by half of wavelength, steepens as the wavelength decreases. As the slope increases, the focusing of the electric field in IDZ increases so that Dukhin's mode becomes dominant as the wavelength decreases. Thus, the fluorescent dye started to be depleted at the trough as the wavelength of the microchannel boundary was shorter (See L = 100 μm, 200 μm and 500 μm of Figure 2.6(c)). Furthermore, as shown in t = 10 s, IDZ expanded around the location where the zone initially formed. In contrast, Rubinstein's mode becomes predominant over Dukhin's mode so that the expanded IDZ moves back and forth when L exceeds threshold values (*i.e.* L = 500 μm and ∞ of Figure 2.7(a)).

On the other hand, the initial positions of IDZ are not determined by the focused electric field in the case of the EOF regime (*i.e.* d = 15 μm), because the wall transport is dominant over the ion transport. Therefore, the formation of IDZ is not affected by the local slope of the nanoporous membrane surface, unlike in EOI regime. Consequently, IDZs were uniformly formed along the edges of the membrane regardless of the wavelength and maintained for substantial time as shown in Figure 2.7(b). As shown in t = 10 s, IDZs expanded still in flat regardless of the wavelength of the membrane boundary. These unique differences between EOI

and EOF regimes were also verified by the overlimiting conductance of each case, as follows.

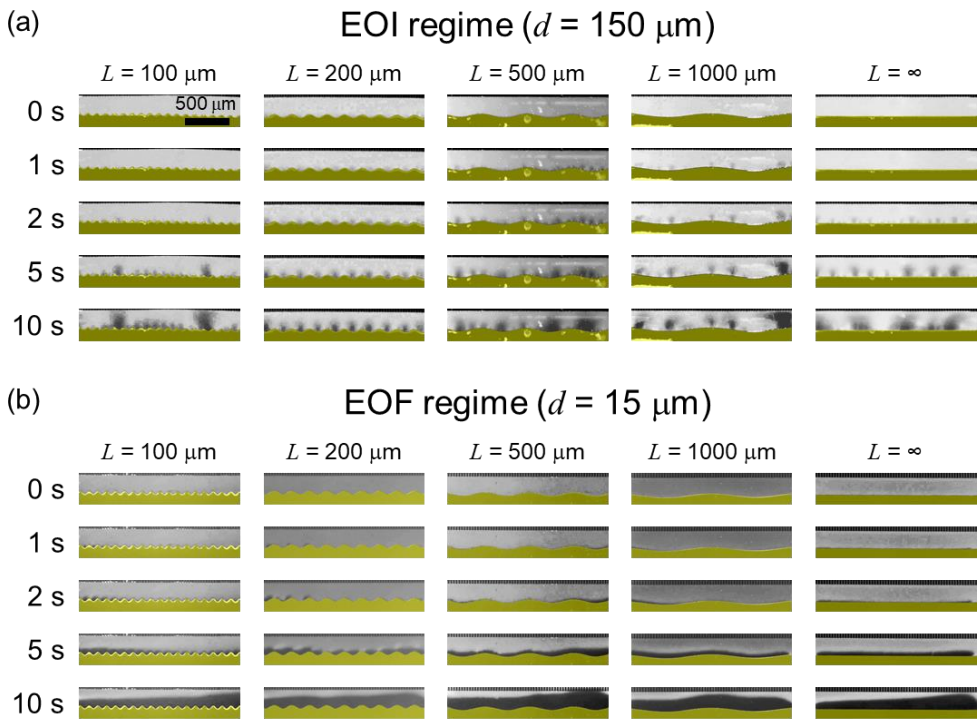

Figure 2.7. (a) Snapshots of IDZ induced at the main channel boundaries of sine wave with various wavelengths (L = 100 μm, 200 μm, 500 μm, 1000 μm and ∞(flat)) in EOI regime (150 μm depth), and (b) snapshots of IDZ in EOF regime (15 μm depth). Each series of the snapshots were captured from a single video at times of 0 s, 1 s, 2 s, 5 s and 10 s.

2.3.3.3. Overlimiting Conductance in EOI and EOF Regime

As mentioned in the section of "An IDZ Formation along Arbitrary-Shaped Membrane", the mechanisms of the overlimiting conductance in the EOI and EOF regime are significantly different from each other. In both cases, the extended space charge layer (ESCL) inside IDZ is uniformly growing at low voltage. As the external voltage increases further, ESCL is still uniform in EOF regime, while the layer can be fluctuated in a system of larger characteristic length scale (*i.e*. EOI regime). The fluctuation leads non-negligible perturbation of Coulombic force across ESCL so that it generates a vortical fluidic motion to satisfy a mass conservation[49]. This vortex becomes larger and eventually drags ions in bulk into the membrane surface. The vortex competes against neighboring vortices so that the location on membrane where ions can transport could be randomly distributed, which is the simple description of EOI and the initiation of overlimiting current. Therefore, controlling the vortices or the fluctuations may lead a significant effect on an overlimiting conductance, either higher or lower. In the light of the results shown in Figure 2.7(a), we can expect that the overlimiting conductance can be affected by the membrane morphology as the positions of the vortices were controlled as a function of the wavelength in the EOI regime[50]. Thus, we measured the overlimiting conductance of devices with 150 μm depth at various L. To calculate the overlimiting conductance, I-V curves were measured first. See details in Experimental Setup section. As shown in Figure 2.8(a), the lowest current curve was obtained in the case of flat membrane ($L = \infty$) in EOI regime. To calculate the overlimiting conductance, we sampled the difference of the current values at 5 V and 10 V since the overlimiting current appeared from the voltage larger than 2 V. Then, the overlimiting conductance as a

function of L was plotted as shown in Figure 2.8(b). The overlimiting conductance at L = 100 μm and 1000 μm was higher than the one at the flat membrane (dashed line) while the overlimiting conductance of the other cases (L = 200 μm and 500 μm) was as similar as the one of the flat case. Therefore, we confirmed that the overlimiting conductance was largely affected by the wavelength of the undulated membrane surface in the EOI regime. Note that these experimental results shows a different trend from ones of previous researches[51, 52]. We presumably assume that the difference resulted from the limitation of the device employing the Nafion film, which is patterned only on the bottom side of the microchannel. Because the major scope of this chapter is demonstrating a new nanofabrication method and its applicability, we may leave the detailed fluid dynamic interpretation as a future work. Despite, this experiment demonstrated that nanoporous films were successfully patterned along microchannels with different wavelengths in the EOI regime. More interestingly, completely different results of the overlimiting conductance were obtained when the same measurements were conducted in the EOF regime.

In the case of the EOF regime, ESCL is uniform even in high external voltage due to the much shorter characteristic length, unlike the EOI regime. In the EOF regime, a vortical fluidic motion is induced by the electroosmotic slip and conservation of mass[5]. In the same way of the EOI regime, the overlimiting current is initiated by the drag of ions induced by the vortices. However, unlike the EOI regime, the effect of the membrane surface on the overlimiting conductance is negligible since the positions of the vortices were fixed by the sidewalls as confirmed in Figure 2.7(b). Therefore, one may expect that there was no difference in the current value in the device with 15 μm depth regardless of the wavelength of the membrane surface. As similar as the calculation procedures in the EOI regime, the overlimiting

conductance was extracted from I-V plot (Figure 2.8(d)) and plotted as a function of L as shown in Figure 2.8(e). It confirmed that there was no variation in the overlimiting conductance even with any perturbation of membrane morphology.

Besides the overlimiting conductance, one of the clear evidence which can be extracted from I-V curves to discriminate EOI and EOF regime is the difference in onset voltage. As shown in Figure 2.8(a), the voltage range of limiting regime is 1 ~ 2 V in EOI regime and the interval of measurement was 1 V so that the onset voltages were not clearly shown in the graph. However, it can be expected that the onset voltage of Dukhin's mode is lower than one of Rubinstein's mode because heterogeneity in Dukhin's mode can promote the onset of overlimiting current[53]. In the magnified view shown in Figure 2.8(c) and 2.8(f), we can extract the onset voltage by crossing two regression curves; one from last two points of Ohmic regime and the other from initial two points of overlimiting regime. There was a large difference of the onset voltage between the Dukhin's mode ($V_{\text{onset, }100}$) and Rubinstein's mode ($V_{\text{onset, }\infty}$) in EOI regime (Figure 2.8(c)) while there was no difference in EOF regime (Figure 2.8(f)).

In summary, here we confirmed the effect of the undulated surface on the electro-desalination platforms in the EOI regime is significantly different from the EOF regime through the direct visualization and the electrical measurements. These demonstrations showed that the presenting new nanofabrication method is feasible to realize the micro/nanofluidic devices with realistic structures.

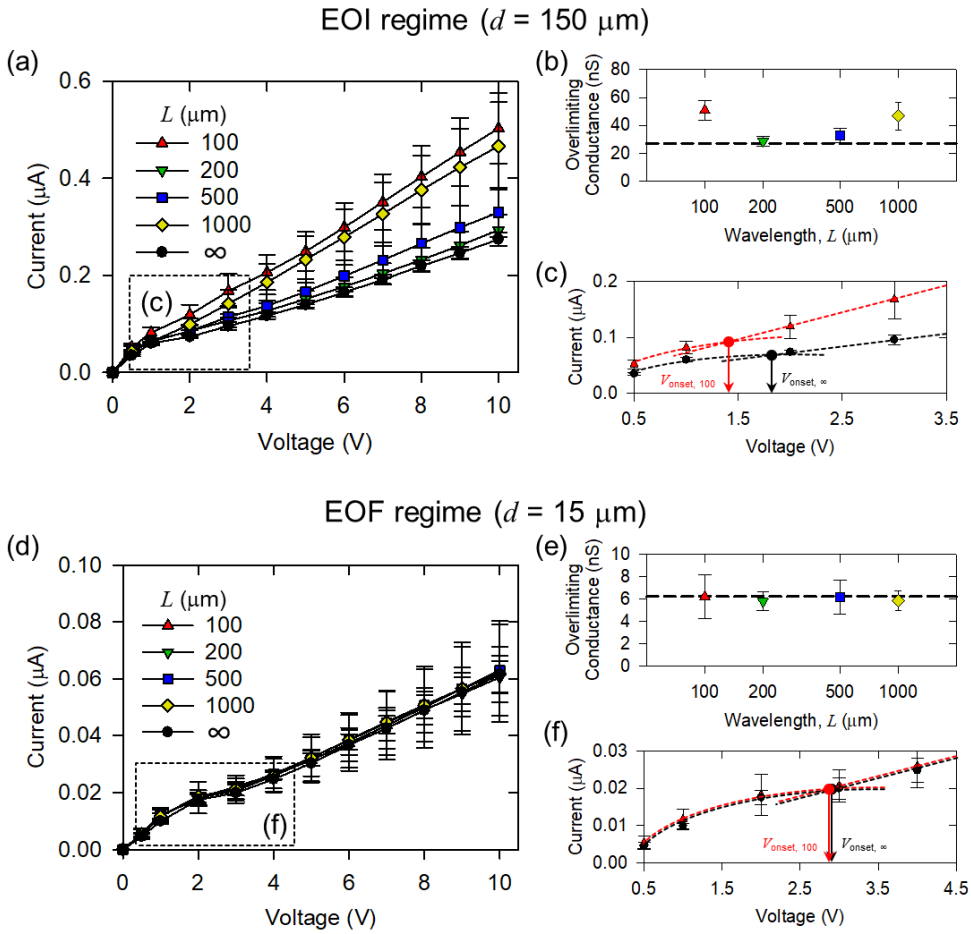

Figure 2.8. (a) I-V characteristics depending on the wavelength and (b) the overlimiting conductance as a function of the wavelength in EOI regime and (c) the zoomed graph which shows V_{onset} of L = 100 μm and ∞(flat). (d) I-V characteristics depending on the wavelength and (e) the overlimiting conductance as a function of the wavelength in EOF regime and (f) the zoomed graph which shows V_{onset} of L = 100 μm and ∞(flat).

2.4. Conclusions

In this chapter, we presented a new adhesive lift method for the fabrication of micro/nanofluidic platform incorporated with an arbitrary-shaped nanoporous film. Utilizing oxygen plasma treatment and spin coating, the presenting method enables the conformal patterning of the nanoporous film on the microchannel network that has arbitrary shaped walls, including square, sine, sawtooth, triangle and fractal wave-shapes. The fabricated micro/nanofluidic device can persist for long term since the nanoporous film was squeezed between PDMS and glass by plasma bonding. Moreover, the I-V curves shown in Figure 2.8 were measured from applying constant voltage over 2 hours, and the curves were measured for 5 times per each experimental device. Thus, the voltage was applied on each experimental device for a total of 10 hours, maintaining a small deviation of the measured electric current. This would be the evidence for the long-term durability of presenting method. In the meantime, the films can be patterned on the microchannels with various depths from 5 μm to 150 μm, which has been mainly utilized in conventional micro/nanofluidic platforms. The conformal patterning was confirmed by direct visualization of fluidic motion in IDZ so that the three mechanisms of ICP (SC, EOF and EOI) was observed by initiating ICP in microchannels with depth of 5 μm, 15 μm and 150 μm, respectively. Furthermore, we conducted the operation of the micro/nanofluidic device with near-practical structures of commercial ion selective membranes such as undulated surface and spacer structure. Consequently, it was confirmed that the effect of the nanoporous membrane surface on ICP in the EOF regime is different from the EOI regime through direct visualization and electrical measurements of the overlimiting conductance.

In addition, the presenting method would be applicable to the fabrication of micro/nanofluidic platforms for biosensing. DNA sensing micro/nanofluidic platform using the physisorption of DNA on anion exchange membrane has been developed[54]. To fabricate this biosensing platform, it requires the nanoporous membrane to be partially patterned on the microchannel region. The partially patterned membrane can be fabricated using the presenting fabrication method with adapting the position and direction of adhesive tapes in step (ii) and step (v) of 'Fabrication of Micro/Nanofluidic Device with Arbitrary-shaped Film' section. Moreover, we expect Nafion can be utilized for biosensing platform since previous researches have been reported biosensing platforms using the functionalization of Nafion membrane surface[54, 55].

Therefore, proposed nanofabrication method would be highly useful for studying electrokinetic phenomena in macro-scale fluidic systems by mimicking a shell of such system and for developing various types of biosensors.

Chapter 3. Non-negligible Effects of Reinforcing Structures inside Ion Exchange Membrane on Stabilization of Electroconvective Vortices

3.1. Introduction

Ion exchange membrane has a property called ion-selectivity that enables only counter-ion to pass through it. The ion-selectivity lets the membranes be a key component in developing electrochemical platforms such as fuel cells [56-58], electrodialysis (ED) [29, 59-61], reverse electrodialysis [47, 62-65], removing heavy metals [66] and electrolysis [67], *etc*. One of the most important phenomena that occurs with the ion exchange membrane is CP. One way of initiating CP is applying an external voltage across the membrane [4, 9, 68-70]. In the case of a cation exchange membrane, for example, cations can pass through the membrane and move toward the cathode, while anions which tend to move to the anode are blocked by the membrane so that anions at the anodic side of the membrane are largely depleted. Consequently, cations are also expelled from the anode side to satisfy electroneutrality. Thus, both ions are depleted in the anodic side to form a zone of extremely low electrical conductivity, called an ion depletion zone (IDZ) [71-73].

The conductance of the entire CP system is mainly affected by the formation of IDZ since the ion concentration in IDZ is much lower than in another region in the system. Due to the high resistance of IDZ, most of the voltage drop occurred across the zone so that the applied electric field is significantly amplified inside IDZ [74, 75]. The amplified electric field can induce an increase of the drift ionic transport through IDZ, despite the low-abundant ions on the anodic side limiting the electric current. Therefore, a layer called extended space charge layer (ESCL) where only cations exist is formed near the membrane to satisfy the continuity of electric current [76]. While the layer is theoretically flat along the membrane, a small perturbation such as heterogeneity of the membrane surface can distort the flatness of ESCL. This distortion leads to a concentration gradient tangential to the membrane and eventually results in an electric body force also tangential to the membrane, even with an applied electric field normal to the membrane. Consequently, the electric body force forms a fluidic motion which is tangential to the membrane. This fluidic motion and the mass conservation leads to the formation of vortices pairs inside IDZ and the vortices are called electroconvection (EC) of Dukhin's mode [7].

The formation of EC in Dukhin's mode is resulted from the heterogeneity of the membrane, either in geometry or physico-chemistry. However, it has been reported that EC is formed even when the membrane geometry is homogeneous. When ESCL is formed, unavoidable perturbations such as thermal agitation or microscale geometric variation such as small rounding differences deforms ESCL. Then the same scenario with Dukhin's mode repeats to lead to rapid vortices pairs except for

the locations of vortices are random with the homogeneous membrane. This mode of EC formation in a random position is called Rubinstein's mode [8]. Moreover, if the applied voltage exceeds a threshold value, the random formation of EC becomes chaotic [11, 77-79]. This chaotic EC can pump ions at the bulk into the membrane so that the conductance of the entire CP system can be significantly enhanced. However, due to the inherent nature of chaotic behavior, the conductance enhancement also has a large fluctuation called instability which is a major nuisance in engineering developments. [8, 49]. Furthermore, energetically inefficient operation becomes more important problems recently. [80] Besides CP system, EC has been actively utilized in electrodeposition and sample preconcentration, *etc*. [81-83]

Therefore, micro/nanofluidic platforms with additional microstructures have been suggested for the stabilization of EC. For instance, the effect of additional structures inside microchannels (*i.e*. dielectric pillar array or non-uniform microfin network, *etc*.) which guide the direction of the electroconvective flow have been reported [84, 85]. In addition to the examples using microstructures, the systems with heterogeneous nanoporous membranes have been also suggested to induce EC of Dukhin's mode. For example, periodically modified patterns on the membrane surface based on the concept of ion exchange funneling [86] or undulated membrane surface have been utilized for the alignment of electroconvective vortices [10, 51, 87-90]. However, most of these studies have been focused on the modification of the

surface of the membrane, which means additional fabrication processes and costs should be involved. On the other hand,

the industrial-grade ion exchange membranes inherently have a reinforcing structure in the form of reinforcing filaments (or clothes) that mechanically sustains the membrane [91-94]. In other words, the reinforcing structures have been utilized as mechanical components in the membranes, in a similar way of steel bars in reinforced concrete structures. In the meantime, the structure acts as an insulator so that the ions should bypass the structure. Therefore, a careful design of the reinforcing structure would be able to control the ion transportation through the membrane. For example, the EC of Dukhin's mode due to the ion exchange funneling can be induced by the reinforcing structures even on homogeneous membranes, because an electric field can be focused between the reinforcements, *i.e*. there is a conductivity difference between an ion selective resin and the reinforcing cloth.

Based on this idea, in this chapter, we demonstrated the stabilization of EC near ion exchange membranes with insulated reinforcing structures. In the numerical simulations, the reinforcement domain was configured as a void domain in which ions cannot pass through the domain. In the micro/nanofluidic experimental device, Nafion solution was patterned excluding the regions of the reinforcements. Both studies simultaneously pointed out that the vortices were aligned to the positions of the reinforcements as the reinforcing structure was wide and close to IDZ. The alignment of vortices was also demonstrated in chaotic regime as well. Through the

extraction of ion concentration profiles from the simulations, the stabilization of vortices was visualized with the peaks of the profiles. In the case of the experiments, the stabilization of EC was visualized with the fluorescence intensity profiles extracted from the direct visualization of IDZ. Moreover, EC alignment was quantitatively tested with the standard deviation of the values in the time-averaged profile. As a result, chaotic EC was aligned like the stable regime, when the reinforcement was wide and close to the anodic bulk. Additionally, the stabilization in chaotic regime was demonstrated with electrical measurements. In both the numerical simulations and the experiments, the electric current was stabilized without temporal fluctuations when EC was stabilized, leading to stable electric power output. Thus, the key findings in this chapter would provide an effective and useful way to stabilize EC in various CP systems including not only macro-scale ED system but also mesoscale bio-molecular preconcentrator because the reinforcing structures are already included in the industrial-grade membranes.

3.2. Methods

3.2.1. Numerical Methods

Numerical domain was set as shown in Figure 3.1, to model symmetric binary aqueous electrolyte near a cation-exchange membrane including reinforcing structures. The dimensionless heights of the membrane and the electrolyte on both sides of the membrane were fixed as 1, and the dimensionless width of the entire domain was set to 4. Inside the membrane domain, reinforcements were periodically placed in the horizontal direction (x-axis). The geometry of the reinforcements was a critical parameter for the stabilization of EC in this chapter. The dimensionless height of the reinforcement was fixed at 0.1 and the dimensionless width of the reinforcement was defined using L_{inter}, which is the length of the gap between the reinforcements. The spacing distance between the center of the reinforcements, which is the sum of the width of the reinforcement and L_{inter} was defined using L. The vertical position of the reinforcements was defined using H. L, L_{inter} and H are adjustable parameters in this chapter. For example, the case of $H / L = 0$ is a partially impermeable membrane on the anodic side and the case of $L_{\text{inter}} / L = 0$ refers to a membrane completely blocked by reinforcements. The fluidic motion in the electrolyte is blocked at the membrane and the ion transports are blocked at the boundaries between the membrane and the reinforcements so that the model simulates EC in electrolyte around a cation-exchange membrane with a reinforcing structure.

The domain is governed by the nondimensionalized form of Poisson's equation, Nernst-Planck equation, the conservation of fluid mass and the incompressible Stokes equations. The domains of electrolytes are governed by

$$-\nabla^2\phi = \frac{1}{2\lambda_D^2}\left(c_+ - c_-\right), \tag{1}$$

$$\frac{\partial c_\pm}{\partial t} = -\nabla\cdot\left(-\nabla c_\pm \mp c_\pm \nabla\phi + c_\pm \mathbf{u}\right), \tag{2}$$

$$\nabla\cdot\mathbf{u} = 0 \quad \text{and} \tag{3}$$

$$\frac{1}{\mathrm{Sc}}\frac{\partial \mathbf{u}}{\partial t} = -\nabla p + \nabla^2\mathbf{u} - \frac{\kappa}{2\lambda_D^2}\left(c_+ - c_-\right)\nabla\phi \tag{4}$$

, where ϕ is the electric potential, λ_D is Debye length, c_+ and c_- are the concentration of cations and anions respectively, t is the time, $\mathbf{u}$ is the velocity, Sc is Schmidt number (the ratio of kinematic viscosity to the diffusion coefficient) as $\mathrm{Sc}=\frac{\mu}{\rho D}$, μ is the dynamic viscosity, D is the diffusion coefficient of ionic species, p is the pressure, κ is the electrohydrodynamic coupling constant (the ratio of the electric body force to the viscous force) as $\kappa=\frac{\varepsilon V_T^2}{\mu D}$ [11], ε is electrical permittivity and V_T is thermal voltage as $V_T \approx 26$ mV at room temperature. On the other hand, the fluidic motion could be neglected inside the cation exchange membrane with considering

extremely low water permeability of the membrane so that the transport phenomena inside the membrane is governed by

$$-\nabla^2\phi = \frac{1}{2\lambda_D^2}\left(c_+ - c_- - N\right) \quad \text{and} \tag{5}$$

$$\frac{\partial c_\pm}{\partial t} = -\nabla\cdot\left(-\nabla c_\pm \mp c_\pm \nabla\phi\right) \tag{6}$$

, where N is Donnan concentration (the ion exchange capacity of the membrane) which was set to 20. We assumed that the membrane was fully hydrated for the numerical convenience, while the water can be transported into the membrane since the membrane can be deficiently hydrated in reality. In fact, the electroconvective instability can be affected by the water transport into the membrane. [95] However, the transport effect was neglected because we intended to focus on the effect of reinforcing structures on electroconvection only as well as to avoid numerical complexity. Equations of (1) – (6) were nondimensionalized by the length of the membrane height L_0, the bulk concentration c_0, the diffusion time $t^* = \frac{L_0^2}{D}$, the diffusion velocity $u^* = \frac{D}{L_0}$, the dimensionless pressure $p^* = \frac{\mu D}{L_0^2}$ and the thermal voltage V_T. Since the domain inside reinforcement was remained as void, the domain was not governed by any equations (*i.e.* interfaces between the membrane and the reinforcing structure were treated as impermeable surfaces).

Dimensionless boundary conditions at the anodic bulk are given by

$$\phi = V_{app}, \ \mathbf{u} \approx \mathbf{0} \ \text{ and } \ c_{\pm} = 1 \tag{7}$$

, where V_{app} is the applied voltage. In the case of cathodic bulk, the nondimensionalized boundary conditions are given by

$$\phi = 0, \ \mathbf{u} \approx \mathbf{0} \ \text{ and } \ c_{\pm} = 1. \tag{8}$$

For the boundaries at the left and right sides of the membrane and electrolyte domains, we applied a periodic boundary condition. At the interfaces of the electrolyte domains and the membrane domain, no-slip condition ($\mathbf{u} \approx \mathbf{0}$) is given for the flow field and flux continuity conditions are applied for electric field ($\mathbf{n} \cdot \left(-\nabla\phi\right)\big|_{\text{electrolyte}} = \mathbf{n} \cdot \left(-\nabla\phi\right)\big|_{\text{membrane}}$) and ion concentration ($\mathbf{n} \cdot \left(-\nabla c_{\pm} \mp c_{\pm}\nabla\phi + c_{\pm}\mathbf{u}\right)\big|_{\text{electrolyte}} = \mathbf{n} \cdot \left(-\nabla c_{\pm} \mp c_{\pm}\nabla\phi\right)\big|_{\text{membrane}}$). For the interfaces of the membrane and the reinforcements, no-penetration conditions are given for the electric field ($\mathbf{n} \cdot \left(-\nabla\phi\right) = 0$) and the ion concentration ($\mathbf{n} \cdot \left(-\nabla c_{\pm} \mp c_{\pm}\nabla\phi\right) = 0$). The values of λ_D, Sc and κ was set to 0.001, 1000 and 0.5 respectively under the assumption of thick boundary layer condition for typical aqueous solutions which have been widely employed for the numerical convergence in the previous numerical researches about electroconvective instability [10, 11, 49, 68, 87, 95-101]. Furthermore, the effect of κ on critical voltage and critical wavenumber is negligible [102]. All governing equations of equation (1) – (6) with boundary conditions including equation (7) – (8) were solved by COMSOL Multiphysics software.

‘Poisson’s Equation’ module, customized ‘General Form PDE’ module and ‘Creeping Flow’ modules were simultaneously solved with time-dependent solver.

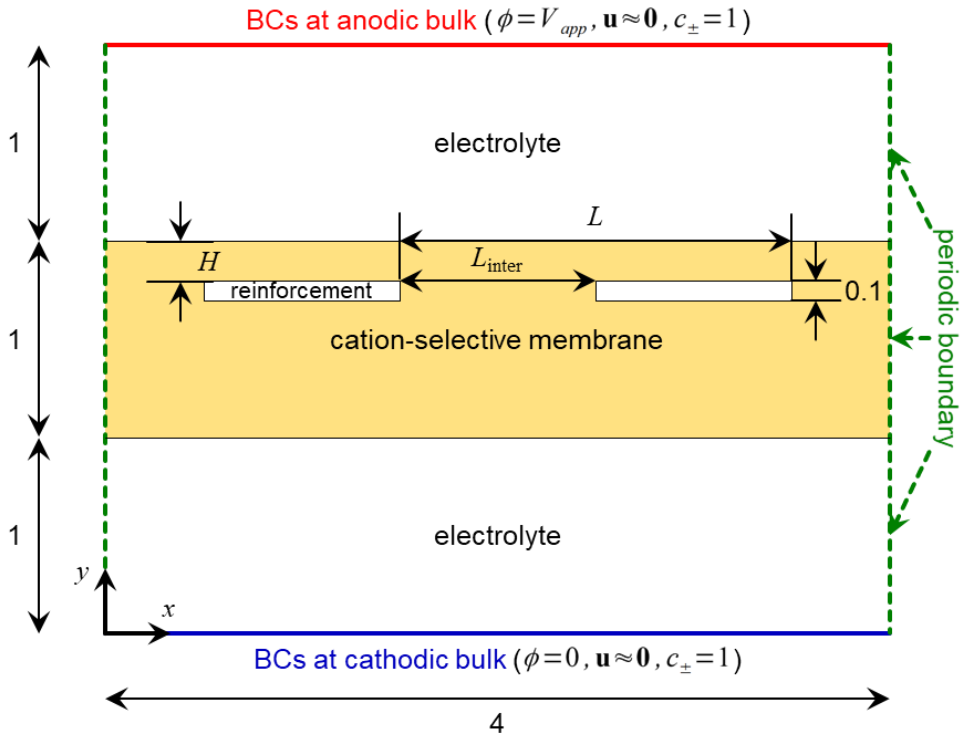

Figure 3.1. The schematic diagram of numerical domain for a concentration polarization system with ion exchange membrane including reinforcing structures.

3.2.2. Experimental Methods

As shown in Figure 3.2(a), the micro/nanofluidic device was prepared by sandwiching an ion exchange membrane with two polydimethylsiloxane (PDMS) (Sylgard 184 elastomer kit, Dow Corning, USA) blocks. The PDMS blocks were fabricated by soft lithography method. Briefly, microchannel structure was patterned on a silicon wafer. Then, PDMS solution was prepared with mixing PDMS base and curing agent in a ratio of 10:1, and the solution was poured on the microchannel-patterned wafer. The ion exchange membrane was patterned on the PDMS block 1 with Nafion solution (Sigma Aldrich, USA) by adhesive lift method developed by our group [103]. In PDMS block 1, rectangular pillar structures with a thickness of 50 μm are patterned on the membrane area to implement reinforcing structures. Therefore, the ion transports are blocked at the pillar area in the fabricated device so that the area can be utilized as reinforcing structures. To prevent incomplete bonding between two PDMS blocks, a straight microchannel with a depth of 100 μm is patterned on the PDMS block 2. The microchannel area was designed to include only the pillar area, neither main channel nor ground channel. After bonding two PDMS blocks with oxygen plasma treatment (CuteMP, Femto Science, Korea), another degassed PDMS solution was injected into the microchannel on the PDMS block 2 to prevent the leakage of buffer solution into the microchannel. Since there is no overlap between the straight microchannel on PDMS block 2 and the microchannel network on PDMS block 1, the injected PDMS solution was not leaked into the

microchannel network. After the injected PDMS solution was cured, the PDMS block and a slide glass were bonded with an oxygen plasma bonder.

The description of the microchannel network was as followings. There is a main channel (200 μm of height, 1.6 mm of length and 200 μm of depth) in the middle of the buffer channel (200 μm of height, 2.8 mm of length and 200 μm of depth). They were connected with an array of microchannel with dimensions of 20 μm height, 100 μm length and 15 μm depth. The reason why the main channel was separated from the buffer channel was that one need to isolate the EC only inside the main channel so that the ion concentration at the upper boundary of the main channel can be maintained at 1 mM. The Nafion membrane was patterned on a region between the main channel and a ground channel (200 μm of height, 2.8 mm of length and 200 μm of depth) with a dimension of 200 μm width and 1.6 mm length, indicated in yellow in Figure 3.2(b). The height of the reinforcing structure inside the membrane was fixed to 40 μm. On the other hand, the length of the reinforcing structure was varied with the value of L_{inter}, which is defined as the distance between the reinforcing structures. In other words, when L_{inter} is long, the length of reinforcement is short. The vertical position of the reinforcements was varied with the value of H, which was defined in Figure 3.1. The device had three reinforcing structures of full size in the middle and half size on both sides as shown in Figure 3.2(b). The horizontal positions of the centers of the reinforcements were aligned at the middle of the membrane for the full-sized structure and both endpoints of the membrane for the half-sized structures.

For visualization experiments, 1 mM KCl (Sigma Aldrich, USA) + 100 μM Sulforhodamine B (Thermofisher, USA) solution was used as sample solution. The devices were degassed for 30 minutes before the injection of the sample solution to prevent air bubbles formed in the microchannels. As shown in Figure 3.2(b), the sample solution was injected into the buffer and ground channel each with flow rate of 0.5 μL/min by a syringe pump (Fusion 100, Chemyx, USA). Ag/AgCl electrodes were connected to the buffer and ground channel and the external voltage (source measure unit, Keithley 236, USA) was applied to the electrodes. Then, the formation of IDZ was directly visualized by recording the repulsion of the fluorescent dye in the main channel under observation by an inverted fluorescence microscope (IX53, Olympus, Japan) and the CellSens program (Olympus, Japan) was utilized for recording the images. The line profile of fluorescent intensity of the Sulforhodamine B dye was extracted by ImageJ program.

For electrical measurement experiments, the same sample solution was used. The electric current was measured by maintaining the applied voltage at a constant level for 5 minutes to ensure the saturated development of IDZ. Also in chronoamperometry, the voltage was measured by maintaining the applied electric current at a constant level for 5 minutes. To obtain I-V curves, the measurement was iterated from 1 V to 20 V at the interval of 1 V. Reproducibility of the result was ensured by repeating the same experiment at least 25 times (5 trials for a device and 5 devices for a case).

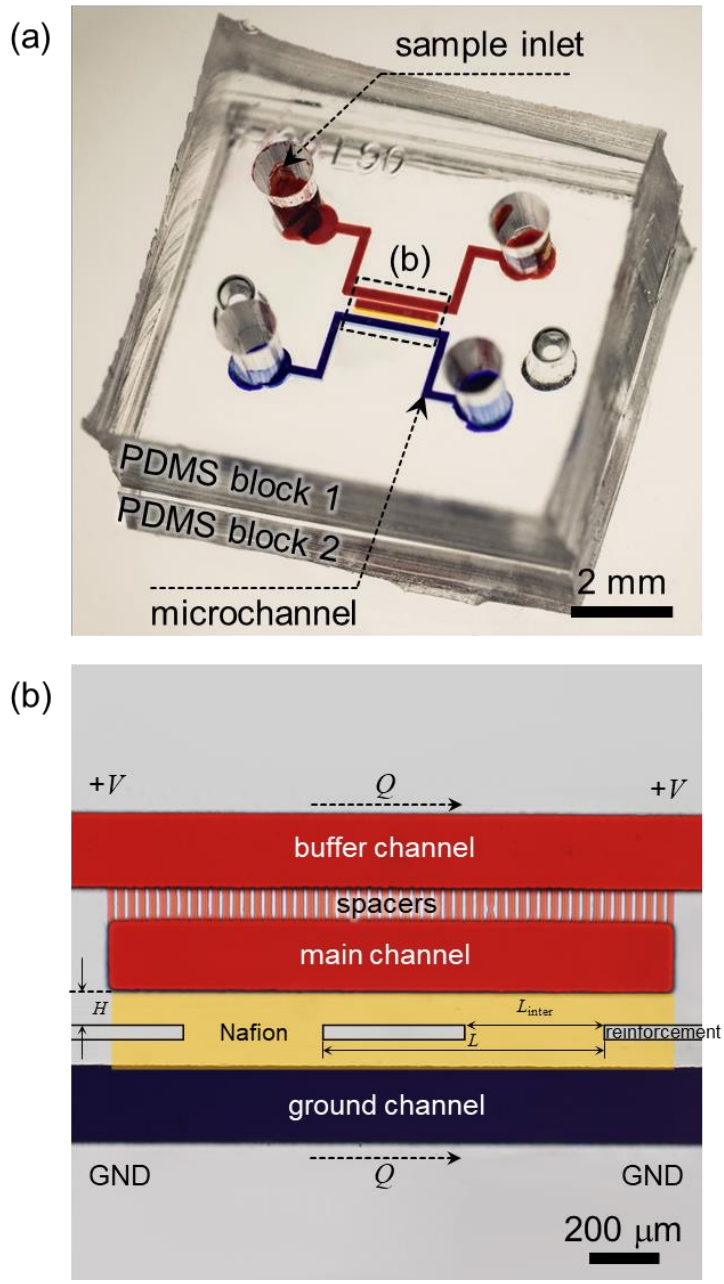

Figure 3.2. (a) The image of micro/nanofluidic device with nanoporous membrane including reinforcing structures and (b) the microscopic image at the nanoporous membrane between the main and ground channel.

3.3. Results and Discussion

3.3.1. Demonstration of Electric Field Focusing due to Reinforcing Structure

Previously, Rubinstein's mode and Dukhin's mode have been suggested for the major mechanisms of EC. Rubinstein's mode refers to EC induced by growth of small concentration fluctuation by positive feedback mechanism [8, 104]. On the other hand, Dukhin's mode refers to EC occurred by the focusing of electric field induced by the heterogeneity in the membrane [7]. In this work, we utilized Dukhin's mode induced by the electric field focusing with the insulation of the reinforcing structures inside the ion exchange membrane which are shown in Figure 3.1 and 3.2.

In the absence of the reinforcing structures (Figure 3.3(a)), the ions are being transported just normal to the cation exchange membrane before the initiation of EC since the external electric field only has a normal component to a homogeneous cation exchange membrane. Therefore, the tangential component of the electric field is zero on the dissected horizontal line inside the cation exchange membrane (y = 1.905, A-A′) and on the dissected horizontal line at ESCL (y = 2.001, B-B′) as shown in Figure 3.3(a)-(i) and 3.3(a)-(ii). However, when the ions are being transported across the membrane with the reinforcing structures inside, the ions are blocked at the interfaces between the reinforcing structures and the membrane since the reinforcements are insulated. Consequently, all the ionic current reroutes at the surface of the reinforcements and eventually flows through the gaps between the

reinforcements. Therefore, the ionic current paths in the membrane are focused around the gaps between the reinforcing structures. Due to the focused current path under the constant electrical conductivity (σ) of the nanoporous membrane, the electric field is also focused at the gaps as shown in Figure 3.3(b)-(i) since the electric current density (**J**) is proportional to the electric field (*i.e*. $\mathbf{J} = \sigma\mathbf{E}$). Previous works would provide distinct evidence of the curved electric field around the reinforcing structure [105-107]. As shown in Figure 3.3(b)-(ii), the tangential component (E_x) of the electric field is relatively weak compared to E_y or $|\mathbf{E}|$ since most of the voltage drops across ESCL (*i.e*. the electric field is significantly intense in ESCL). Although, as shown in the inset of Figure 3.3(b)-(ii), the focused electric field inside the membrane also slightly affects the electric field in ESCL so that the distribution of the *x*-component of the electric field at ESCL shows a similar distribution of E_x at A-A′ which is shown in Figure 3.3(b)-(i). This weak tangential electric field in ESCL plays a seeding role of the formation of EC. Therefore, one can expect that EC could be aligned with the reinforcing structures inside the membrane so that we demonstrated this EC alignment with the reinforcements through the numerical simulations first.

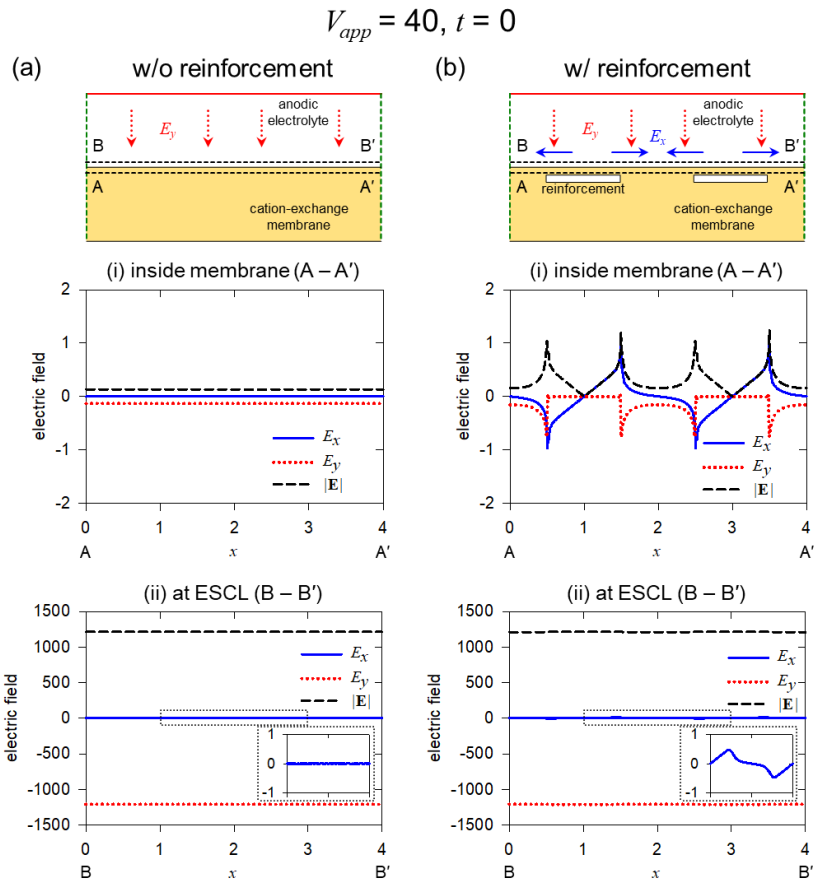

Figure 3.3. The schematic diagram of the numerical domain with omitted cathodic electrolyte in the cases of (a) the membrane without reinforcement and (b) the membrane with reinforcement. The red dotted arrows and the blue solid arrows indicate the y component of the electric field and the x component of the electric field, respectively. A-A′ lines and B-B′ lines in the schematics are dissected at y = 1.905 and y = 2.001, respectively. The graphs show the profiles of the electric field extracted from (i) A-A′ lines and (ii) B-B′ lines. The insets in graphs of the profiles at B-B′ lines show the graph with the y-axis scaled from −1 to 1 and the x-axis scaled from 1 to 3.

3.3.2. Demonstration of EC Alignment depending on Geometry of Reinforcing Structure

Here, we demonstrated that the alignment of stable EC depends on the geometric parameters of the reinforcing structures inside the nanoporous membrane. First of all, the effect of the spacing between the centers of the reinforcements (L) on the patterns of EC was investigated with the numerical simulation results as shown in Figure 3.4. To have an identical mechanical strength of the reinforcements, the total sum of the reinforcement length was the same regardless of L. To induce stable EC, the numerical simulation was conducted for dimensionless time (tD / L_0^2) of 1 with an applied voltage of V_{app} = 40. The patterns (direction and location) of EC were depicted with the cyan lines which express the streamlines of the flow field. Note that the magnitudes of the flow field were not reflected in the cyan lines. The cathodic electrolyte (lower electrolyte domain in Figure 3.1 or ground channel in Figure 3.2) was omitted in Figure 3.4 since there was any notable flow field or cation distribution in the electrolyte. In the case of the membrane without the reinforcements (Figure 3.4(a)), EC was formed at random positions and electroconvective vortices expanded to the anodic bulk boundary as shown in Figure 3.4(a). While the centers of the vortices seem to be pinned in the specific locations in the Figure, the pinned positions of the centers keep to be varied at every trial of simulation (see 2nd and 3rd run of Figure 3.4(a)), meaning that there might be a large run-to-run deviation in those systems. When the reinforcements are included in the membrane (from Figure 3.4(b) to Figure 3.4(e)), however, the positions of the

vortices tend to align on the reinforcements at every simulation trial. Our hypothesis expected that the tangential flows converge toward the centers of gaps between the reinforcements so that the upward flows are formed at the centers of the gaps and the downward flows are formed at the centers of the reinforcements (indicated by the solid black arrows). Therefore, as shown in the case of $L = 2$ (Figure 3.4(c)) and $L = 1$ (Figure 3.4(d)), the solid black arrows were aligned and pinned at the centers of the reinforcements. However, in the case of $L = 4$ (Figure 3.4(b)), one pair of vortices was misaligned with the reinforcement so that the downward flow was misaligned with the reinforcement (indicated by the dotted black arrows) while another black solid arrow was aligned with the reinforcement. Thus, if the spacing between the centers of the reinforcements is too long, all electroconvective vortices would not be affected by the focused electric field. Conversely, the dotted black arrows were misaligned with shorter reinforcing structures (see $L = 0.5$ of Figure 3.4(e)). This result shows that the electroconvective vortices were misaligned with the tangential electric field when the spacing distance between the reinforcements is too short. From these results, we could confirm that EC can be aligned with the focused electric field by the reinforcing structures and the focusing can be affected by the spacing of the reinforcing structures since the electric field is focused around the gaps between the reinforcements. Besides of spacing, how deep the reinforcements are buried in the membrane is another important parameter that manufacturers and consumers must consider. Therefore, we need to investigate the alignment of EC depending on H and L_{inter} as well through numerical simulations and experiments.

The alignment of stable EC was evaluated with changing the width of the reinforcements (L_{inter} / L = 0.1, 0.3, 0.5, 0.7 or 0.9), and the vertical position of the reinforcements (H / L = 0.05, 0.1 or 0.2) as shown in Figure 3.5(a). For better understanding, note that L_{inter} / L = 0 and 1 is the case of the membrane was completely separated by the reinforcements and the case of the membrane without the reinforcements, respectively. The phase diagram shows that EC was aligned as H and L_{inter} decreased since the electric field was focused more as the gap between the reinforcements became denser and the gap was closer to the anodic side. To demonstrate the focusing of the electric field depending on the geometry of the reinforcements, the magnitude of the electric field ($|\mathbf{E}|$) along A-A′ line and the tangential component of the electric field (E_x) at ESCL along the A-A′ line was extracted from the simulations as shown in Figure 3.5(b). Note that B-B′ lines were dissected 0.005 above the reinforcements (*i.e.* $y = 2 - H + 0.005$). To compare the effect of L_{inter} and H on the electric field along those lines, the cases of L_{inter} / L = 0.1 ~ 0.9, H / L = 0.05 and the cases of L_{inter} / L = 0.1, H / L = 0.05 ~ 0.2 were analyzed and shown in Figure 3.5(b)-(i) and Figure 3.5(b)-(ii), respectively. Since the electric field is focused around the gap between the reinforcements, the electric field at the gaps increases as L_{inter} decreases so that the absolute value of the tangential electric field increases as shown in Figure 3.5(b)-(i). Therefore, EC was aligned as L_{inter} decreased as shown in Figure 3.5(a). Moreover, the electric field at the gaps increases as H decreases so that the tangential electric field strengthens at the ESCL as shown in Figure 3.5(b)-(ii) since the effect of focusing in the anodic electrolyte increases as

the vertical position of the gap becomes closer to the anodic electrolyte. Consequently, EC was aligned as the vertical distance between the reinforcement and the anodic electrolyte decreased as shown in Figure 3.5(a).

As a further investigation, unaligned EC and aligned EC of the extreme cases were visualized through the numerical simulations and the experiments. In the case of the simulations, when the reinforcement was installed far from the anodic electrolyte and the spacing was long ($H = 0.4$ and $L_{inter} = 1.8$), four pairs of stable EC was formed while only two reinforcements were included in the membrane so that two of the downward flow in the vortices were misaligned to the reinforcements as shown in Figure 3.6(a)-(i). On the other hand, when the reinforcement was close to the anodic electrolyte and the spacing was short ($H = 0.1$ and $L_{inter} = 0.2$), the x-position of the downward flow in the electroconvective vortices coincided with the x-position of the midpoints in the reinforcements ($x = 1$ and 3). Furthermore, only one pair of vortices was formed per one midpoint of the reinforcement as shown in Figure 3.6(a)-(ii). Hence, in the simulation, EC was aligned when the reinforcement was longer and closer to the IDZ. The extreme case ($H = 0$) has a resemblance with a 2D-patterned ion exchange membrane which was reported in both simulation [108] and experiment [109]. Since our scenario is needed to be verified by experiment as well, the following section shows the alignment of EC depending on the geometry of the reinforcing structures with the shape of IDZ.

When IDZ initiates, it has been reported that charged particles are repelled from the depletion zone due to electric neutrality [4, 110]. Thus, streamlines shown in

numerical simulations are hard to be visualized. Instead, the boundary of IDZ has been visualized either with fluorescent charged particles or fluorescent dyes [111, 112]. Consequently, the electroconvective vortices can be indirectly visualized by the shape of IDZ since the vortices determine the boundary of IDZ. Here, the positions of EC were trapped with the repelled fluorescent dye in this chapter. To induce a stable EC, the applied voltage was set to be V = 10 V. When the reinforcement was far from the main channel and the spacing distance was long (H = 140 μm, L_{inter} = 720 μm), the repelled fluorescent dyes were isolated in the positions independent of the reinforcements (indicated by dotted arrows), and the positions were kept to be moved over time as shown in Figure 3.6(b)-(i). On the contrary, when the reinforcement was closer to the main channel and the spacing was shorter (H = 60 μm, L_{inter} = 80 μm), the repelled fluorescent dye was fixed near the middle of each reinforcement (indicated by solid arrows in Figure 3.6(b)-(ii)). From these comparisons, we confirmed that EC can be stably aligned with wider reinforcements nearer to the anodic electrolyte. This conclusion was drawn under a stable EC condition (*i.e*. lower applied voltage) so that we need to evaluate the effect of the reinforcements in a chaotic EC regime as well.

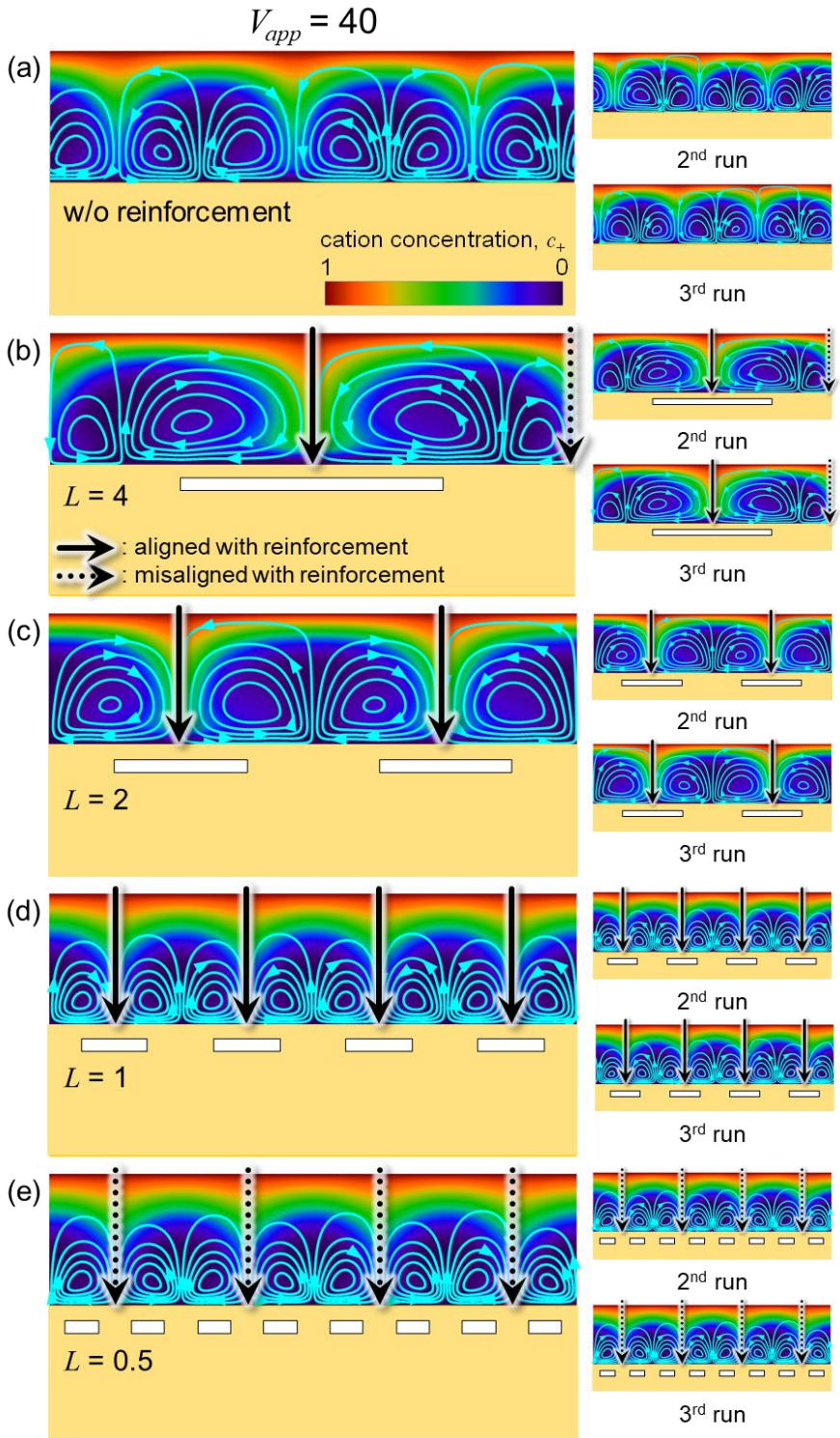
V_{app} = 40
(a)
w/o reinforcement
cation concentration, c_+
1
0
2nd run
3rd run
(b)
L = 4
: aligned with reinforcement
: misaligned with reinforcement
2nd run
3rd run
(c)
L = 2
2nd run
3rd run
(d)
L = 1
2nd run
3rd run
(e)
L = 0.5
2nd run
3rd run

Figure 3.4. The snapshots of EC (a) when reinforcement is not included in the membrane and included in the membrane and the snapshots of EC with the reinforcing structures were conducted when the spacing distance between the reinforcements is (b) $L = 4$, (c) $L = 2$, (d) $L = 1$ and (e) $L = 0.5$. The streamlines of EC were expressed as the cyan lines. The black arrows indicate the horizontal positions of flow with direction into the membrane. The dashed arrows and dotted arrows indicate the flow which is aligned with the reinforcements and unaligned with the reinforcements, respectively.

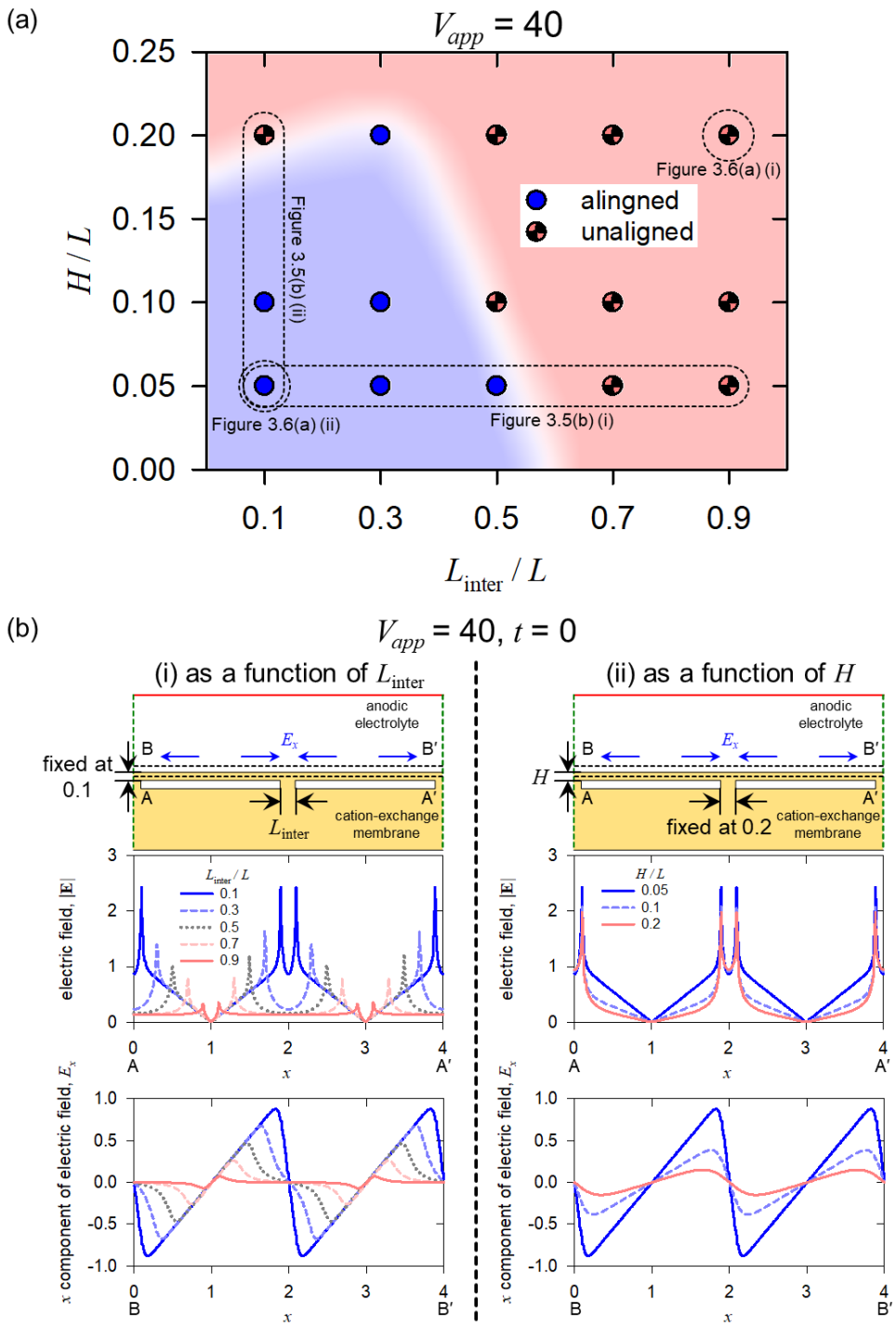
(a)
V_{app} = 40
0.25
0.20
0.15
0.10
0.05
0.00
H / L
0.1
0.3
0.5
0.7
0.9
L_{inter} / L
alingned
unaligned
Figure 3.6(a) (i)
Figure 3.5(b) (ii)
Figure 3.6(a) (ii)
Figure 3.5(b) (i)
(b)
V_{app} = 40, t = 0
(i) as a function of L_{inter}
(ii) as a function of H
anodic electrolyte
fixed at 0.1
fixed at 0.2
cation-exchange membrane
E_x
L_{inter}
H
electric field, |E|
L_{inter} / L
H / L
x component of electric field, E_x
x

Figure 3.5. (a) The phase diagram of the alignment of stable electroconvective vortices depending on the reinforcement geometry. (b) The schematic diagrams of numerical domain as a function of (i) L_{inter} (H was fixed at 0.1) and (ii) H (L_{inter} was fixed at 0.2) and the plots of the magnitude of the electric field at A-A′ and the graphs of the x component of the electric field at B-B′ when $t = 0$ with applied normalized voltage of $V_{app} = 40$.

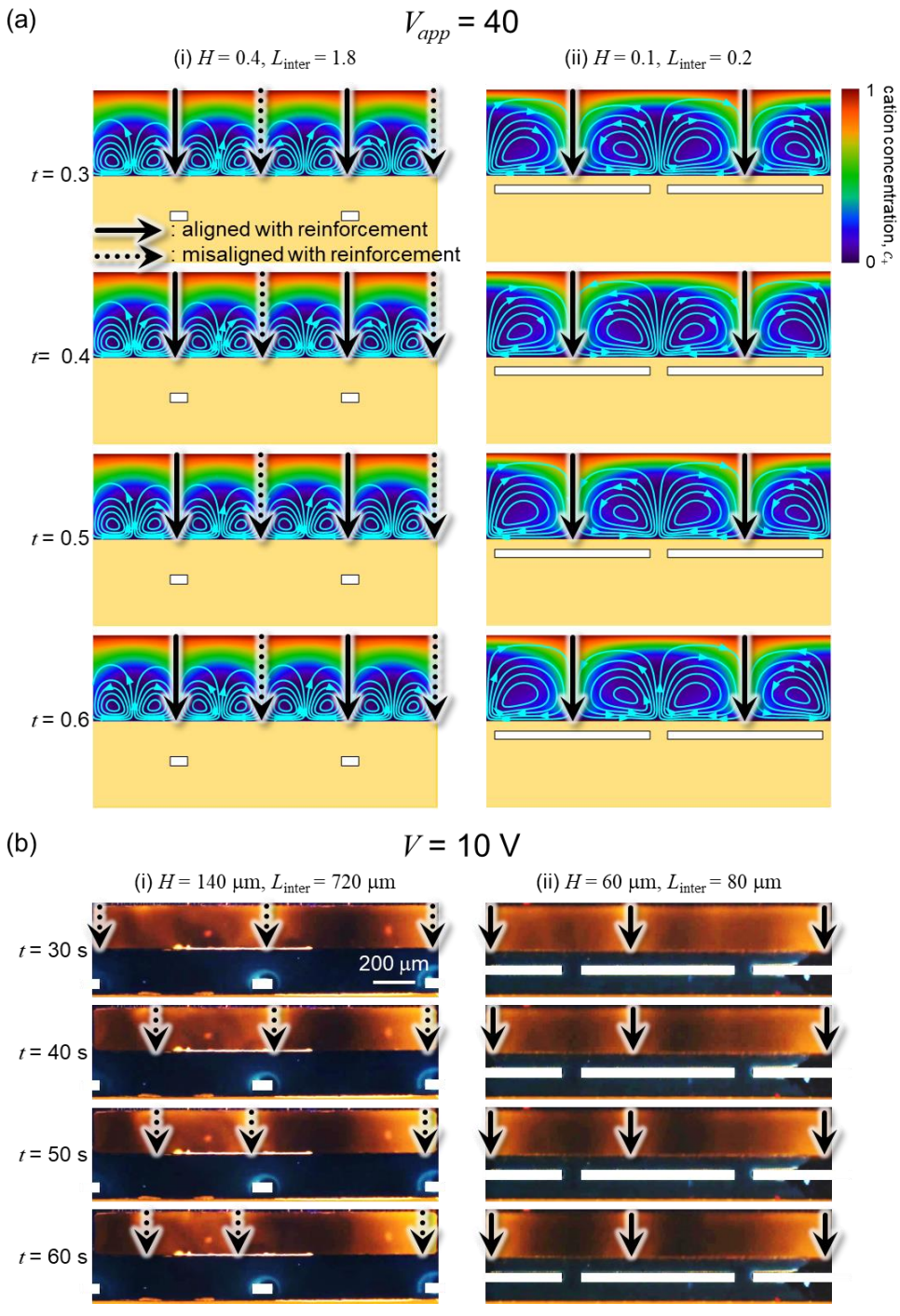
(a)
V_{app} = 40
(i) H = 0.4, L_{inter} = 1.8
(ii) H = 0.1, L_{inter} = 0.2
1
cation concentration, c_+
0
t = 0.3
: aligned with reinforcement
: misaligned with reinforcement
t = 0.4
t = 0.5
t = 0.6
(b)
V = 10 V
(i) H = 140 μm, L_{inter} = 720 μm
(ii) H = 60 μm, L_{inter} = 80 μm
t = 30 s
200 μm
t = 40 s
t = 50 s
t = 60 s

Figure 3.6. (a) The snapshots of EC in simulation when the vortices were ((i) H = 0.4, L_{inter} = 1.8) not aligned and ((ii) H = 0.1, L_{inter} = 0.2) aligned at t = 0.3, 0.4, 0.5 and 0.6. The streamlines of EC were expressed as the cyan lines. The black arrows indicate the horizontal positions of the flow from the bulk to the membrane. The dashed arrows and dotted arrows indicate the flow which is aligned with the reinforcements and misaligned with the reinforcements, respectively. (b) The snapshots of IDZ near the membrane with reinforcements when vortices were ((i) H = 140 μm, L_{inter} = 720 μm) not aligned and ((ii) H = 60 μm, L_{inter} = 80 μm) aligned at t = 30 s, 40 s, 50 s and 60 s. The black arrows indicate the horizontal positions of the repelled fluorescent dye.

3.3.3. Alignment of EC by Reinforcing Structures in Chaotic Regime

Industrial ED systems have been known to operate with the current value between 80% of limiting current [80] and the initial stage of overlimiting current [29]. However, chaotic EC has attracted attention for the fundamental study of EC and the control of the unexpected formation of EC in ED systems [21, 113-116]. Therefore, we need to investigate chaotic EC by increasing the applied voltage over stable EC condition. In the chaotic regime, Rubinstein's mode is more dominant than Dukhin's mode so that the vortices in IDZ were vigorously stirred [9, 49]. Consequently, it has been reported that the chaotic EC induces the instability of the electric power efficiency or the instability of the shape of IDZ [117]. Thus, we used the aforementioned alignment scheme to stabilize the chaotic EC.

For the formation of chaotic EC, the external voltage was applied with a nondimensionalized voltage of $V_{app} = 60$ for the numerical simulation and $V = 20$ V for the experiments. The applied voltage of 20 V in the experiments forms a similar condition with $V_{app} = 60$ in the simulations since the voltage drop across the main channel is estimated as 1.529 V ($\approx 58.80 V_T$). In the numerical simulations, we employed the ion distribution induced by the convective transport of EC to visualize the stabilization. In electroconvective vortices, the upward flow away from the membrane transports the depleted electrolyte to the bulk, while the downward flow into the membrane transports the electrolyte of c_0 from the bulk [118]. Therefore, the

ion concentration is higher in the region where the electrolyte flows downward than the one of the region where the electrolyte flows upward [10, 100]. Consequently, the position of electroconvective vortices can be tracked by the profile of the ion concentration. The line profile of the ion concentration was extracted at y = 2.5 (C-C′). As a result, when the reinforcements were sufficiently wider, the ion concentration profile was invariant as a function of time and the profile peaked at the middle of the reinforcements as shown in Figure 3.7-(i). On the contrary, when the reinforcement was insufficiently long, the profile of the ion concentration fluctuated over time as shown in Figure 3.7-(ii).

These tendencies were also verified by the visualization experiments. The stabilization of electroconvective vortices was visualized with the fluorescence intensity profiles in the main channel, since the electroconvective vortices can be visualized by the void of the fluorescent dye (*i.e.* dark area in Figure 3.7-(iii) and Figure 3.7-(iv)). To extract the fluorescence intensity profile, a horizontal line was dissected in the middle of the main channel (100 μm above the edge of the membrane, D-D′). As shown in Figure 3.7-(iii), when the reinforcements were wide, the vortices were aligned so that the fluorescence intensity profiles were fixed over time. Conversely, the fluorescence intensity fluctuated over time when the reinforcing structure was insufficient for the vortex alignment as shown in Figure 3.7-(iv).

Since we verified that stable EC was aligned as H and L_{inter} decreases in the ‘Demonstration of EC Alignment depending on Geometry of Reinforcing Structure’ section, it can be expected that the chaotic EC would be more stabilized as H and

L_{inter} decreases. Therefore, we quantified the stabilization of the electroconvective vortices as a function of H and L_{inter} with the time-average of the extracted profiles. In the cases of the alignment, the positions of peaks at each time are overlapped so that the standard deviation of the time-averaged profiles is high. On the other hand, since the positions of the peaks keep shifting over time when the profiles were unaligned, the time-averaged profiles must be flat so that the standard deviation should be relatively small compared to the aligned case. Therefore, the standard deviation of the time-averaged profiles of the ion concentration and the fluorescence intensity was higher when the reinforcements becomes wider and closer to the anodic electrolyte as shown in the phase diagram of Figure 3.7. From these results, we confirmed that the chaotic EC was also stabilized with the reinforcements. Since the chaotic EC in ED system results in the instability of the electrical conductance of the system, one can expect that the reinforcing structures inside the membrane can stabilize the electric power consumption of the ED system as well in chaotic regime. Therefore, we need to re-verify the stabilization of EC in chaotic regime by electric current measurements.

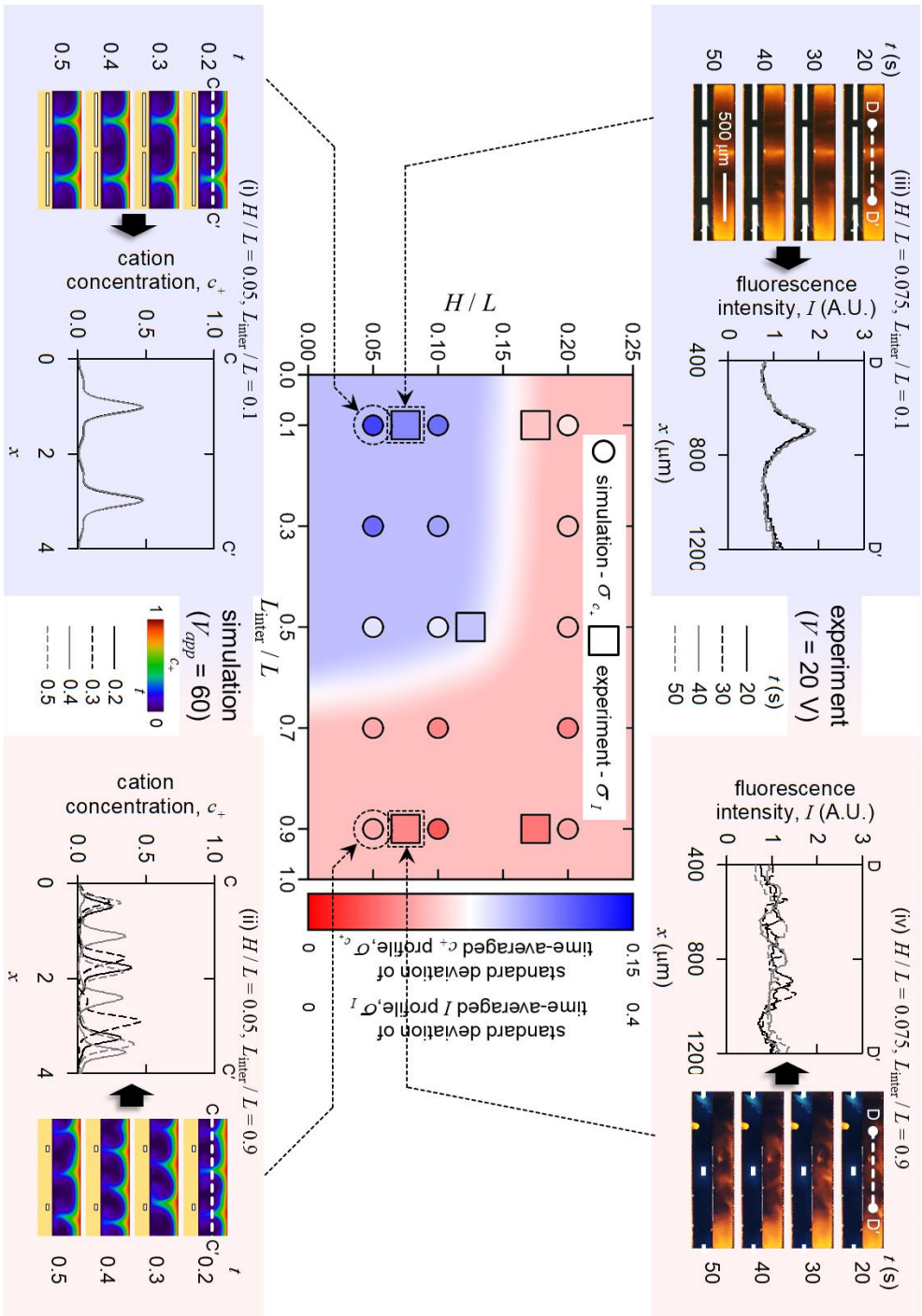
(iii) $H/L = 0.075$, $L_{inter}/L = 0.1$
t (s)
D
D'
500 μm
fluorescence intensity, I (A.U.)
x (μm)
experiment (V = 20 V)
t (s)
20
30
40
50
(iv) $H/L = 0.075$, $L_{inter}/L = 0.9$
H/L
L_{inter}/L
simulation - σ_{c_+}
experiment - σ_I
time-averaged I profile, $\bar{G}_I$
standard deviation of
time-averaged c_+ profile, $\bar{G}_{c_+}$
(i) $H/L = 0.05$, $L_{inter}/L = 0.1$
(ii) $H/L = 0.05$, $L_{inter}/L = 0.9$
C
C'
cation concentration, c_+
x
t
simulation (V_{app} = 60)
c_+
1
0
0.2
0.3
0.4
0.5

Figure 3.7. The insets at bottom show the snapshots of IDZ in the simulations when vortices were aligned ((i) H / L = 0.05, L_{inter} / L = 0.1) and unaligned ((ii) H / L = 0.05, L_{inter} / L = 0.9) at t = 0.2, 0.3, 0.4 and 0.5. The white dashed line in the insets of (i) and (ii) shows the dissected line in the middle of the anodic electrolyte and the graphs in those insets show the ion concentration profiles along C-C′ line extracted from each snapshots. The insets at top show the snapshots of IDZ in the experiments when vortices were aligned ((iii) H / L = 0.075, L_{inter} / L = 0.1) and unaligned ((iv) H / L = 0.075, L_{inter} / L = 0.9) at t = 20 s, 30 s, 40 s and 50 s. The white dashed line in the insets of (iii) and (iv) shows the dissected line in the middle of the main channel and the graphs in those insets show the fluorescence intensity profiles along D-D′ line extracted from each snapshots. The graph in the middle shows the phase diagram of the standard deviation of the time-averaged cation concentration profiles and the time-averaged fluorescence intensity profiles as a function of L_{inter} and H.

3.3.4. Stabilization of Electric Current using Reinforcing Structures in Chaotic Regime

In the anodic electrolyte, the "fingers" of relatively high ion concentration (greenish and reddish color) are formed as shown in Figure 3.7 since downward flow in EC transports electrolyte of c_0 from the bulk to the membrane. Thus, the electric current density in the region of fingers is higher than the one of the region of IDZ (blueish color) since an ion concentration is higher in the fingers, *i.e.* higher conductivity. Therefore, the electric current fluctuates when the thickness of the fingers changes or the fingers form and disappear due to the instability of chaotic EC. Thus, the stabilization of EC can result in the stabilization of the electric current value.

This scenario was verified through the simulations first. In the cases of EC without reinforcement and EC with insufficient reinforcement, the electric current density fluctuated over time since the fingers were continuously deformed due to the unaligned vortices as shown in Figure 3.8(a) and Figure 3.8(b). The insets show that only thin fingers are formed when the electric current density reached valleys, while thick fingers are formed when the electric current density reached peaks. Conversely, the electric current density was stabilized in the aligned EC case as shown in Figure 3.8(c). Two thick fingers are stably formed over time as shown in the insets.

In a similar way of the simulations, the electric current fluctuated over time when reinforcement was not included or EC was unaligned in the experiments, while the

electric current was stabilized without temporal fluctuation when the vortices were aligned as shown in Figure 3.8(d). Moreover, chronoamperometry of 0.5 μA was conducted for the unaligned EC case and the aligned EC case. As shown in Figure 3.9, there were smaller fluctuations of the voltage value when EC was aligned with the wide reinforcements compared to the unaligned case. Furthermore, despite the insulation of the reinforcing structures, there was a negligible effect on the average electric current value and the average voltage value since the conductivity of the ion exchange membrane is extremely higher than the one of IDZ. Therefore, the electric power of the CP system can be stabilized with the reinforcing structures without a loss since the electric power is calculated as the product of the voltage and electric current value.

In previous researches, it has been reported that there is an instability of the electric current of CP system in chaotic regime [9, 11, 79]. Therefore, the I-V characteristics of the CP systems show wide error bars in chaotic regime. Figure 3.10(a) shows the I-V curve of the experimental devices in Ohmic (0~1 V), limiting (1~2 V), stable EC (2~15 V) and chaotic (15~20 V) regime when the applied voltage was swept from 0 to 20 V. Note that the two representative I-V curves which are plotted in Figure 3.10(a) were each measured from a single device of each EC alignment case to reveal the clear difference between the aligned EC case and the unaligned case since there were nonnegligible errors between the experimental devices. The error bars in the curves indicate the range from the minimum to the maximum value of the 5 iteration results from a single experimental device of each

EC alignment case. In other words, the narrower error bar in chaotic regime means that EC and the electric current were stabilized. To show the width of error bars in chaotic regime, the chaotic regime of the I-V curves was zoomed as shown in Figure 3.10(b). When EC was unaligned, the error bar broadens in chaotic regime as shown in Figure 3.10(b)-(i) since the electric current fluctuates due to the instability of EC. Conversely, in the case of aligned EC, the I-V curve shows a narrow error bar even in chaotic regime as shown in Figure 3.10(b)-(ii). From these results, we can conclude that the reinforcing structures can be utilized for the electric stabilization of CP systems by the alignment of electroconvective vortices.

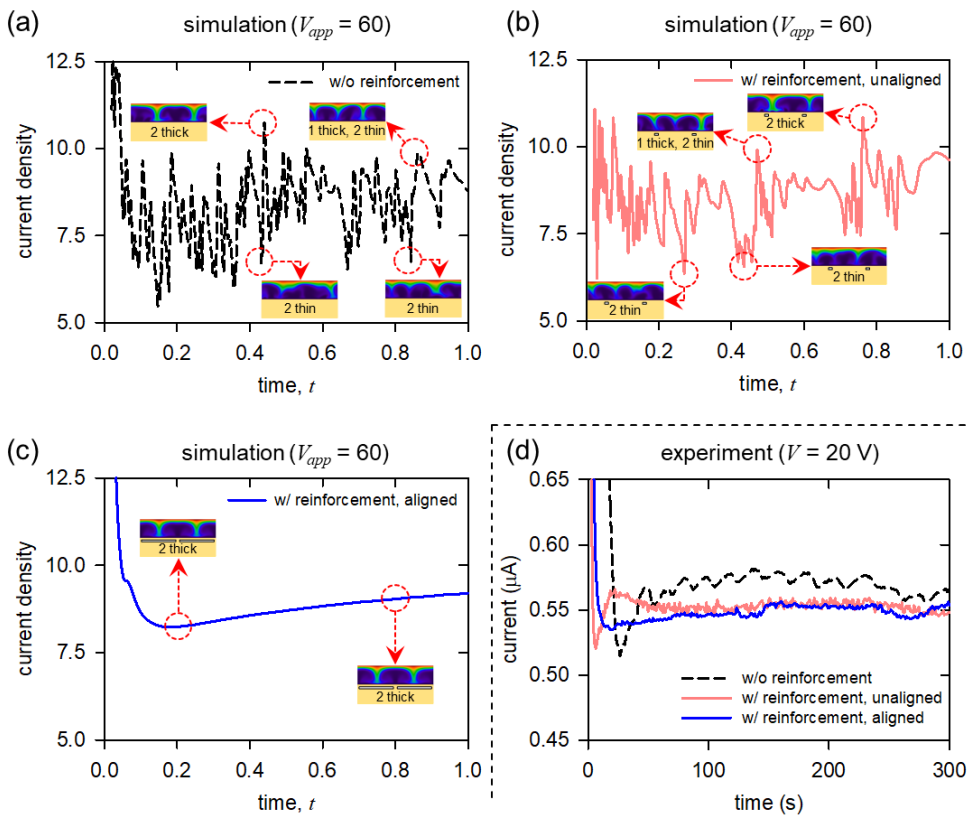

Figure 3.8. The plots of I-t curves in the cases of EC (a) without reinforcing structures, (b) unaligned EC and (c) aligned EC extracted from the numerical simulations. The insets of each graphs show the snapshots at each corresponding time. (d) The graph of I-t curves in the cases of EC without reinforcing structures, unaligned EC and aligned EC measured from the experiments.

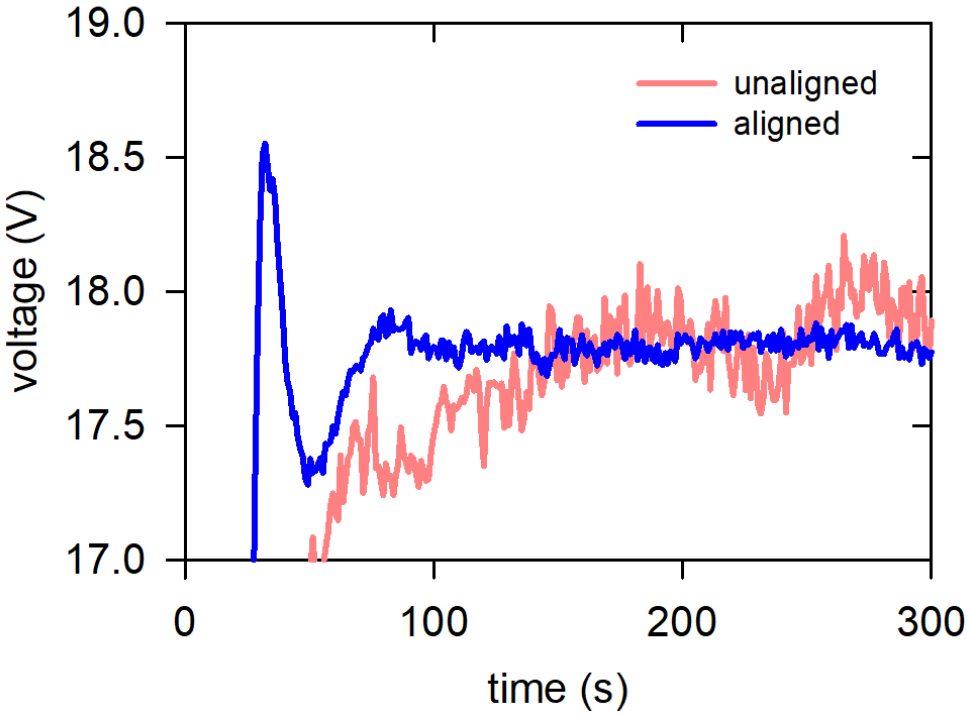

Figure 3.9. The chronoamperometry plot for the cases of unaligned EC and aligned EC.

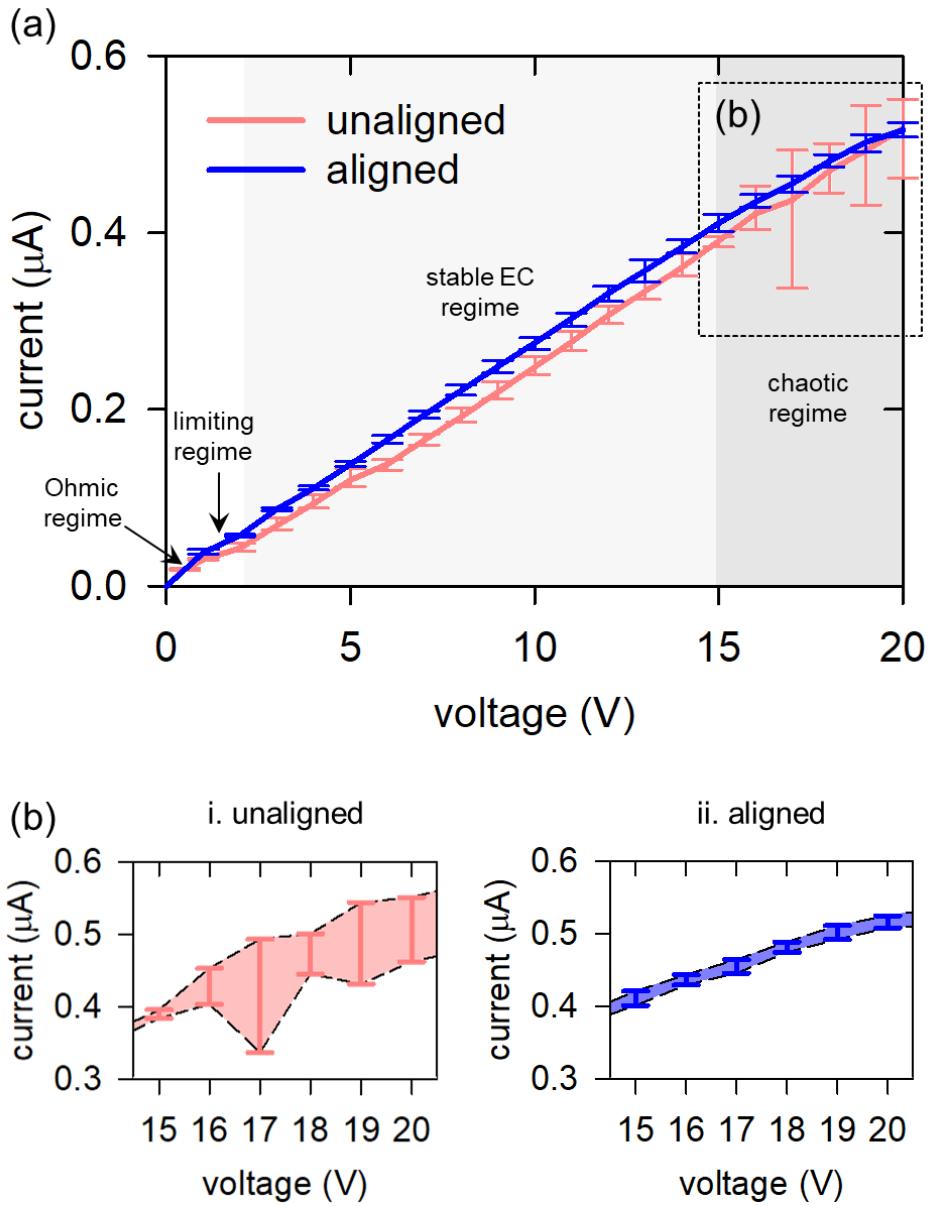

Figure 3.10. (a) The plot of I-V curves with error bars in the cases of unaligned EC and aligned EC measured from the experiments. (b) The graph zoomed at chaotic regime which shows the error bars of the electric currents in chaotic regime when EC is (i) unaligned and (ii) aligned.

3.4. Conclusions

In previous researches, it has been widely studied to stabilize CP systems using EC of Dukhin's mode induced by heterogeneous ion exchange membrane. Such researches have been employed the geometry or the physicochemical property of the membranes and, however, the internal structures of the membranes have not been utilized for the stabilization of EC. Therefore, in this chapter, we investigate the role of the internal reinforcing structure for stabilizing EC. Here, we numerically and experimentally demonstrated the alignment of electroconvective vortices using the focusing of the electric field induced by the reinforcing structures inside ion exchange membrane (Figure 3.1 – 3.3). The stable EC was aligned when the reinforcing structure was adequately wide and close to the anodic electrolyte (Figure 3.4). Additionally, the geometry of the reinforcements for alignment of stable vortices was confirmed by the simulations (Figure 3.5 and 3.6). Furthermore, the electroconvective vortices were aligned depending on the reinforcement geometry even in chaotic regime. To visualize the stabilization of the chaotic EC, ion concentration profiles were extracted from the simulations and fluorescence intensity profiles were extracted from the experiments. As a result, the stabilization of vortices in chaotic regime was successfully visualized with aligned peaks in the profiles. Furthermore, the alignment of EC in chaotic regime was quantified with the standard deviation of time-averaged profiles of the cation concentration and the fluorescence intensity. Similar to the results with the stable vortices, when the reinforcement is wider and closer to the anodic electrolyte, the chaotic vortices were

aligned more (Figure 3.7). Moreover, we demonstrated that the electric current and the electric power were also stabilized when EC was aligned in IDZ (Figure 3.8 – 3.10). Although our scenario was validated in a micro/nanofluidic platform, it can be applied to macro scale systems considering the scalability of the micro/nanofluidic system. Therefore, this result would be worth noting not only for the researchers interested in the fundamentals of EC but also for the manufacturers of the industrial ion exchange membranes.

Chapter 4. Continuous and Spontaneous Nanoparticle Separation by Diffusiophoresis

4.1. Introduction

Efficient particle separation techniques are an essential sample preparation step in the most of bio(medical)- and chemical-analysis. While filters[119, 120], gels[121-123] and centrifugation[124] have been conventionally utilized in those analyses, recently introduced micro/nanofluidic technologies opens new era of high-efficient separation[125-129]. Represented technology is an inertial microfluidic separation[130-132]. It employed a delicate force balance between inertia- and convective-migration of particles so that the particles proceeds designated positions inside a microchannel. While the platform can separate particles in high throughput manner, this technique required a high-pressure hydraulic source. In addition, inertial migrations have a limitation that extremely high flow rate should be required for separating nanoparticle of less than O(100) nm due to Brownian motion[127]. Instead of using mechanical stimulations, electrical nanoparticle separation methods have been reported using an anisotropic nano sieve[34, 126] or ion concentration polarization phenomenon that induces concentration gradient adjacent to a permselective membrane under a dc electric field[133-139]. Those methods can be operated without a high pressure pump, but, however, serious clogging in nanofilter and undesirable instability[117, 140, 141] due to an ion depletion zone impeded their applicability in practical applications.

As per a mechanism without mechanical or electrical stimuli, diffusiophoresis described in section 1.3 has been actively utilized for the particle separation[142, 143]. It refers to the spontaneous motion of particles in an electrolyte with a concentration gradient. The diffusiophoretic migration of particles is caused by two mechanisms. The first one is called chemiphoresis, which occurs by the asymmetric charge density inside an electrical double layer due to the concentration gradient[144]. The other mechanism is an induced electrophoresis by the difference of cation's and anion's diffusion through an electrolyte with the concentration gradient[14]. Thus, it is known that the diffusiophoretic velocity of a particle is affected by the ratio of a particle radius to Debye length[145].

For generating diffusiophoresis, various methods have been suggested to develop the concentration gradient. The simplest method is the injection of electrolytes with different concentrations[146-148] or dissolvable gas[149]. However, these methods required an additional control for the injections. Most recently, a highly charged ion exchange medium was utilized to spontaneously develop the concentration gradient[150-152]. The medium spontaneously drives an exchange between ions from the electrolyte and ones from the medium. This method has an advantage that there is no need of any external apparatus so that it is useful in resource limited settings. Our group has reported a spontaneous particle separation[153, 154] and a spontaneous water purification[152, 155] with diffusiophoresis induced by the ion exchange. These demonstrations were shown in the condition of zero Sherwood number, *i.e*. no tangential flow along the ion exchange medium, so that it requires multiple operation/extraction steps to recover the meaningful volume of the separated (or purified) samples. In order to overcome the limitations, a continuous diffusiophoretic desalination device using the tangential flow has been reported[152],

but its performance was limited to microparticle purification. Furthermore, the previous work based on ion exchange is limited in practical applicability since the release of protons from cation exchange membrane developed an acidic environment.

Therefore, in this chapter, we present a method for continuous and spontaneous nanoparticle separation method based on diffusiophoresis induced by an enhanced concentration gradient. Small addition of Tris-buffer can not only steepen the concentration gradient but also regulate pH so that multiple nanoparticles were successfully separated at physicochemical pH condition. In addition, we confirmed that the previously developed model of diffusiophoretic particle movement[150, 152] so that we were able to demonstrate the separation of nanoparticles with various diffusiophoretic mobilities. Thus, the presenting method would be an efficient platform for analyzing various nano-meter scale bio-particles.

4.2. Materials and Methods

4.2.1. Fabrication of Diffusiophoretic Separation Device

As shown in Figure 4.1(b), the micro/nanofluidic device consisted of the ion exchangeable medium patterned on a polydimethyl-siloxane (PDMS) block and a slide glass. PDMS solution was prepared by mixing PDMS base and curing agent (Sylgard 184 silicone elastomer kit, Dow Corning, USA) in ratio of 10:1. The solution was degassed at vacuum for 1 hour and poured onto a pre-defined silicon wafer to construct the microchannel. The separation channel had the dimension of height 15 μm × width 600 μm × length 18 mm. Two inlets, one was for particles and the other for buffer, had the dimension of height 15 μm × width 60 μm × length 2.5 mm and height 15 μm × width 540 μm × length 2.5 mm, respectively. Nafion (Sigma Aldrich, USA) was used as the ion exchangeable medium. It was patterned with arbitrary-shaped nanoporous membrane patterning method discussed in section 2.2. The PDMS block of the separation microchannel and a slide glass was irreversibly bonded with oxygen plasma treatment (CuteMP, Femto Science, Korea).

4.2.2. Chemical Preparation

The sample solution was prepared by mixing 1 mM NaCl solution (Sigma Aldrich, USA) with 40 nm (em. 532 nm; green), 200 nm (em. 650 nm; red) and 2 μm (em. 580 nm; yellow) carboxylate-modified fluorescent particles (Invitrogen, USA). The buffer solutions used in the experiments shown in Figure 4.4 were prepared by mixing 1 mM NaCl and 1 mM NaCl + 1 mM Tris-base (Sigma Aldrich, USA) solution at various weight percent. For pH measurement, 1 % global pH indicator (Hydrion, USA) was mixed with 1 mM NaCl solution and 1 mM NaCl + 1 mM Tris solution.

4.2.3. Experimental Setups

The solutions were injected with a syringe pump (Harvard apparatus, PHD2200). The migrations of the fluorescent particles were observed under an inverted fluorescence microscope (IX53, Olympus, Japan) and recorded by CellSens program (Olympus, Japan). The fluorescent intensity of each particle stream was measured by ImageJ program. To measure the exclusion distance and separation resolution, fluorescent signal intensity at various L was averaged over 3 minutes.

The pH of solutions was measured at macroscopic scale in 1 mL e-tube for clear visualization. A Nafion sheet (thickness 50 μm × width 1 cm × length 1 cm, Sigma Aldrich, USA) was immersed in the e-tube and the pH changes were measured after 10 seconds under the consideration of the interface between the large area of Nafion sheet and bulk electrolyte.

4.3. Results and Discussion

4.3.1. Concept of Diffusiophoretic Separation

The overview of our proposed continuous and spontaneous diffusiophoretic nanoparticle separator was shown in Figure 4.1(a). The bottom side of the microchannel was connected with a film of cation-exchange medium. Electrolyte with sample particles was injected from lower inlet microchannel, while buffer solution was injected from top inlet microchannel. The flow rates from these two inlets were adjusted so that the linear velocity of solution inside the separation channel was kept to be constant. It is known that an ion exchange process changes ionic concentrations at the interface of an electrolyte and an ion exchange medium. Since the diffusion of the exchanged protons from the medium is faster than one of cations in the electrolyte, the ion concentration near the exchange medium becomes lower than one in the buffer[150]. As the solution flows along the horizontal direction, a concentration boundary layer is developed from the surface of the medium as shown in Figure 4.1(a). The colloidal particles inside the layer migrate away from the medium along diffusiophoretic velocity ($\mathbf{U}_{DPH}$; blue arrow) due to this concentration gradient. In the meantime, convective drag ($\mathbf{U}_{conv}$; black arrow) migrates particles along the direction of flow. Thus, the combination of two velocities results in a slanted directional movement of $\mathbf{U}_{net}$ (yellow arrow). Then, one can define exclusion distance (δ_{ex}) as the longitudinal distance between the medium and the colloidal particle suspension. Due to the difference of diffusiophoretic mobility which is a function of zeta potential and the radius of the particle, *etc*., the particle suspensions were focused at their distinguishable δ_{ex}s. To experimentally observe aforementioned particle motions induced by diffusiophoresis, a microfluidic

chip was fabricated as shown in Figure 4.1(b). The detailed fabrication process was described in the method section.

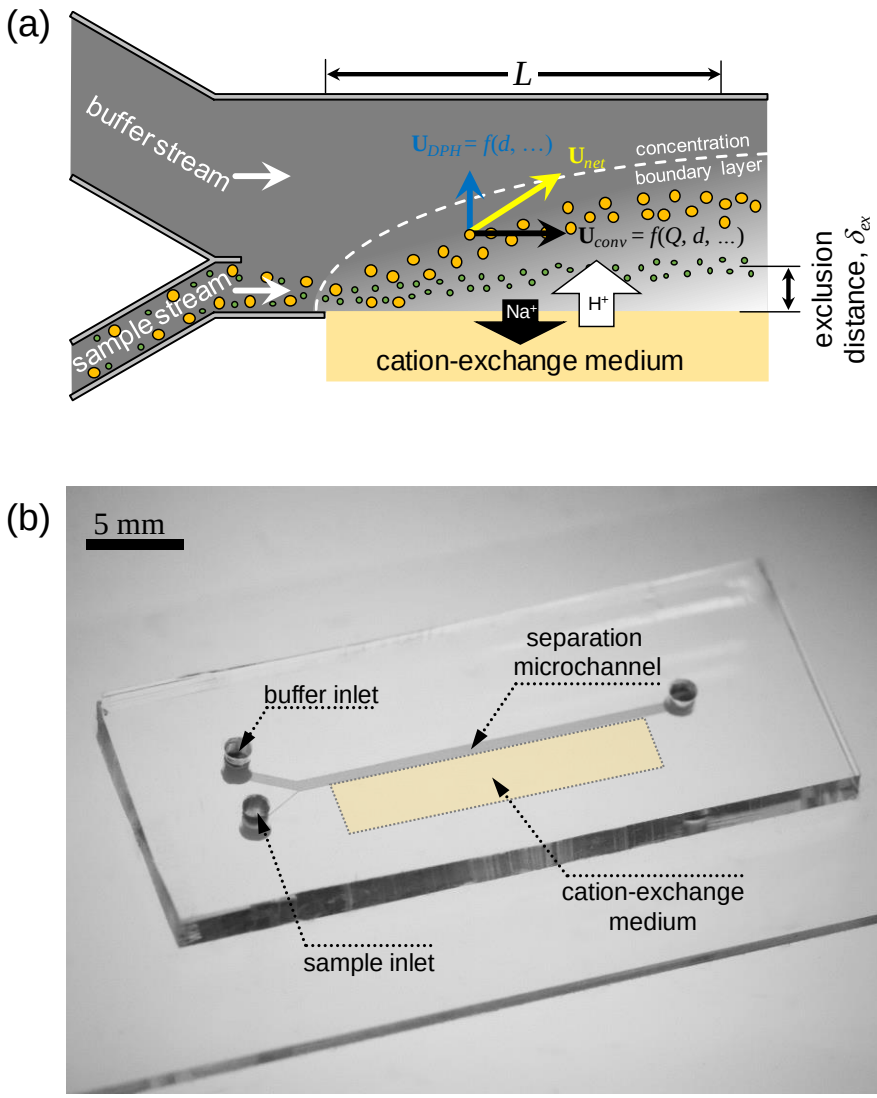

Figure 4.1. (a) The schematic diagram of a nanoparticle separator utilizing the diffusiophoresis induced by spontaneous ion exchange inside concentration boundary layer. The colloidal particle migrates by two velocity components. $\mathbf{U}_{conv}$ is convective drag by flow in microchannel, and $\mathbf{U}_{DPH}$ is diffusiophoretic velocity. (b) Image of the device experimented in this chapter.

4.3.2. Diffusiophoretic Exclusion near Ion-exchange Medium

As shown in Figure 4.2(a), we demonstrated the diffusiophoretic migration of 40 nm-diameter spherical colloids passing through the separation microchannel. Since a concentration gradient was spontaneously induced by the ion exchange process at the cation-exchange medium (*i.e.* Na^+ in the microchannel was exchanged with H^+ in the exchange medium), the immersed particles were diffusiophoretically repelled from the medium. Previous literature reported a model to predict diffusiophoretic velocities of cylindrical particles with arbitrary thickness of electrical double layer when concentration gradient is imposed in transverse direction of the particles[156]. Comparing this non-spherical model with the spherical model[145], the difference of diffusiophoretic velocities between spherical and cylindrical particles increases when the ratio of the particle size to Debye length decreases. However, when the ratio of the particle size to Debye length is over 10, the difference due to the particle shape becomes negligible. For example, one can neglect the difference with 100 nm particles in the thicker electrolyte concentration than 1 mM, *etc*. The concentration gradient diminished outside the concentration boundary layer so that diffusiophoresis should occur only within the layer. At L = 0 mm, the dispersive width of the focused particle stream was about 35 μm. However, the particle stream was broadening with 80 μm due to the diffusion at L = 4 mm. Nevertheless, there was no particle from the ion exchange medium up to the particle stream. Thus, δ_{ex} was defined as the length between the ion exchange medium to the brightest point of the particle stream as depicted in the second panel of Figure 4.2(a).

Figure 4.2(b) showed exclusion distances (δ_{ex}) as a function of horizontal distance (L) at various input flow rates. The exclusion distance was longer when the flow rate

was slower and *vice versa*. The thickness of the concentration boundary layer (δ_c) is a function of the external flow rate of which scaling law was reported as $\delta_c \sim (Dx / S)^{1/3}$ where D is the diffusivity of solute, x is the horizontal position of particle and S is the shear rate near the exchange medium[157]. S was linearly proportional to an injection speed so that higher flow rate resulted in thinner concentration boundary layer. Similar to the concentration boundary layer, δ_{ex} was depending on the external flow rate as shown in Figure 4.2(b). Florea and coworkers suggested that when there is no shear flow, δ_{ex} can be represented as

$$\delta_{ex} = 2\mu_{DP}\sqrt{t_0 t}\,\frac{\nabla c\left(\delta_{ex}\left(t_0\right), t_0\right)}{c_0} \tag{4.1}$$

where μ_{DP} is the diffusiophoretic mobility, t_0 is the arbitrary reference time, t is the time, c is the electrolyte concentration and c_0 is the bulk concentration[150]. Note that the concentration gradient is a function of the exclusion distance and the arbitrary reference time. Their work had been conducted on dead-end geometry and had no need to consider the effect of the external flow on δ_{ex}, while δ_{ex} in our platform would be perturbed by the external flow. However, the flow was always exerted on tangential direction along the cation-exchange medium (*i.e.* x-direction) so that the flow had a negligible effect to the normal motion of particles. Thus, the direction of diffusiophoretic migration was always normal to the medium (*i.e.* y-direction). As a result, t of equation (4.1) was approximately replaced by L / U_{mean} where U_{mean} is the averaged external flow speed. Intuitively, in this chapter, L / U_{mean} implied that the exclusion distance is determined by the horizontal distance that particle moved along the medium, not time (t) for which particles were repelled by diffusiophoresis. Thus, equation (1) can be rewritten as

$$\delta_{ex} \cong 2\mu_{DP}\sqrt{t_0}\,\frac{\nabla c\left(\delta_{ex}\left(t_0\right),t_0\right)}{c_0}\sqrt{\frac{L}{U_{mean}}}\,. \tag{4.2}$$

In equation (2), t_0 and $\nabla c\left(\delta_{ex}\left(t_0\right),t_0\right)/c_0$ were constants[150] so that

$$\delta_{ex} \propto \mu_{DP}\sqrt{\frac{L}{U_{mean}}} \tag{4.3}$$

As shown in the inset of Figure 4.2(b), the experimental points were collapsed on a single line, confirming the scaling law of equation (4.3). More interestingly, equation (4.3) taught one that the exclusion distance is proportional to the diffusiophoretic mobility which is a function of particle zeta potential and particle size, *etc*. Practically, a very high ionic strength can significantly affect the ion exchange capacity and diffusiophoretic movement. Previously, our group has reported experimental and theoretical results of the ion exchange capacity at the wide range of buffer concentrations from 1 mM to 100 mM[152]. We had analyzed the effect of buffer concentration using the Sherwood number which is proportional to U_{mean} / L. If one needed to use 100 times thicker buffer concentration, it was required to set the Sherwood number 5 times lower, *i.g*. operating the device at 5 times slower U_{mean} or with 5 times longer L, *etc*. In addition, this diffusiophoretic movement could be ineffective under a very high ionic strength because the Debye screening is so strong that the resulted zeta potential of a particle is too low. This problem may also cause troubles for bio-particles with much less surface charges compared to the highly charged carboxylated particles used in this study. However, the diffusiophoretic separation capacity would diminished after ~1,800 hours at 1 mM and ~18 hours at 100 mM, respectively according to the previously developed analytical expression[152] so that extremely long separator can overcome this issue.

Theoretically the separator of 3.6 meter-long would keep the diffusiophoretic force all along the microchannel with current U_{mean} of 54 μm/sec. Another potential solution for this issue could be adding an upstream dilution unit before the diffusiophoretic separation unit, if one needs to separate concentration-insensitive bio-particles such as DNA. Unless, one could connect a diverging microchannel with multiple collection branches after the diffusiophoretic separation unit so that the finer collection would help to enhance the separation efficiency. Note that the numerical results about Taylor dispersion is described in Appendix A. Therefore, discussions in this section proposed the practical possibility of continuous diffusiophoretic particle separation.

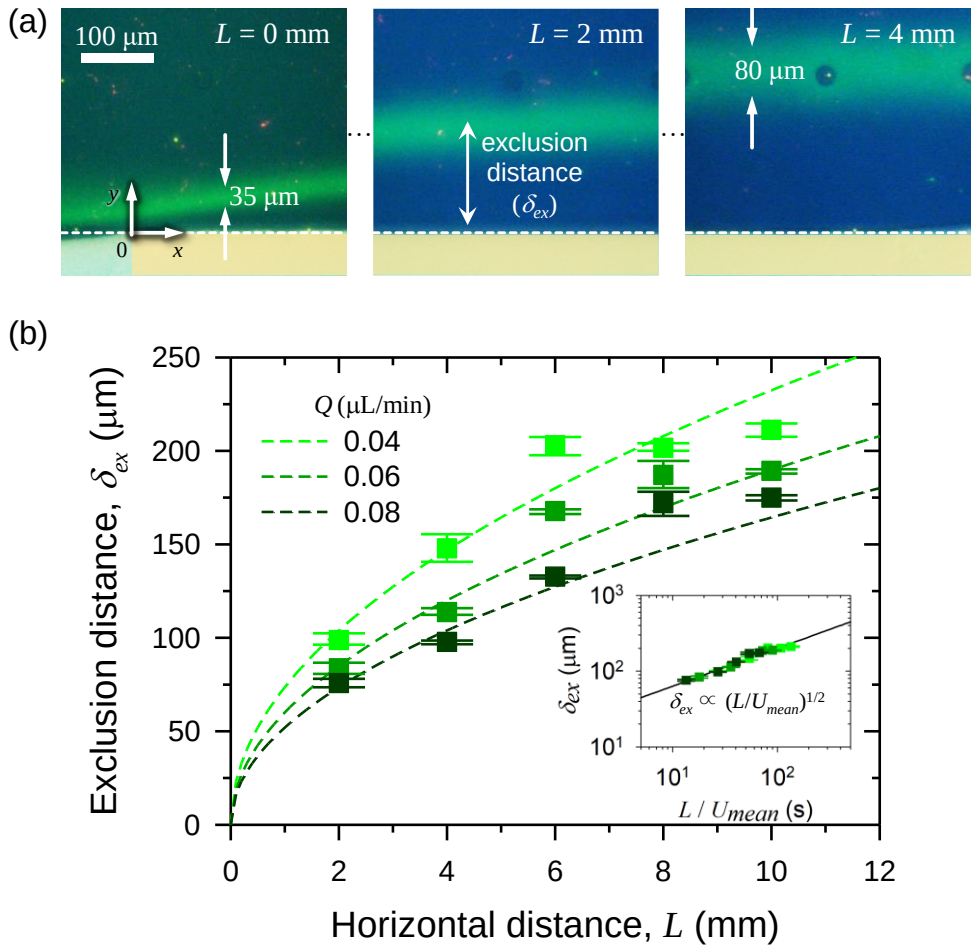

Figure 4.2. (a) The exclusion of 40 nm carboxylate-modified particles at L = 0 mm, 2 mm and 4 mm, respectively. The exclusion distance is the distance between the edge of the ion exchange medium and the average position of the particle suspension. (b) Exclusion distance of 40 nm particle suspension as a function of horizontal distance L with various flow rate inside the microchannel. The inset showed the scaling law of δ_{ex} and L / U_{mean}.

4.3.3. Continuous Separation of Nano-sized Colloidal Suspensions

As discussed in previous section, the exclusion distance, δ_{ex} was varied with diffusiophoretic mobility, μ_{DP} as the material property of colloidal particle. Especially, if the thickness of Debye length, κ^{-1} is much smaller than the particle radius, a (*i.e.* the limit of thin electric double layer, $\kappa a \rightarrow \infty$), μ_{DP} is independent from the particle size and is solely determined by zeta potential or surface charge density of the particle[14]. However, in the case of nano-sized particle, it has been known that μ_{DP} is significantly affected by the particle size due to thick double layer limit. When the ratio of particle size to Debye length increases, μ_{DP} increases as well[145]. Utilizing this size dependency, several batch type nanoparticle separation methods have been demonstrated [146, 153].

In this chapter, we employed carboxylate-modified polystyrene particles of which diameters were 40 nm (green), 200 nm (red) and 2 μm (yellow) for demonstrating continuous nanoparticle separation. Figure 4.3(a) showed the spontaneously separated particle streams as a function of L at the external flow rate of 0.04 μL/min. The larger particle was, the further it was excluded from the cation-exchange surface as predicted[145]. Since 1 mM NaCl solution was injected and its concentration significantly dropped inside the concentration boundary layer, κ^{-1} was comparable to the particle size and, then, the diffusiophoretic mobilities were proportional to the sizes of particle. The size-dependent mobility[158] was given as

$$\mu_{DP} = \frac{\varepsilon \zeta_p^{\,2}}{\eta}\left(1 - \frac{5}{2}(\kappa a)^{-1} + O\left((\kappa a)^{-2}\right)\right) \tag{4.4}$$

where ε is the electrical permittivity of water, ζ_p is the particle zeta potential and η is the viscosity of water. This formula implied that smaller particle retains smaller

diffusiophoretic mobility. Therefore, our observations were in-line with this classical transport theory as shown in Figure 4.3(b). In addition, these experimental points of each particles were laid on each straight line as shown in the inset of Figure 4.3(b), which indicated that the diffusiophoretic mobilities of each particle were different (*i.e*. parallel lines but different *y*-intercept).

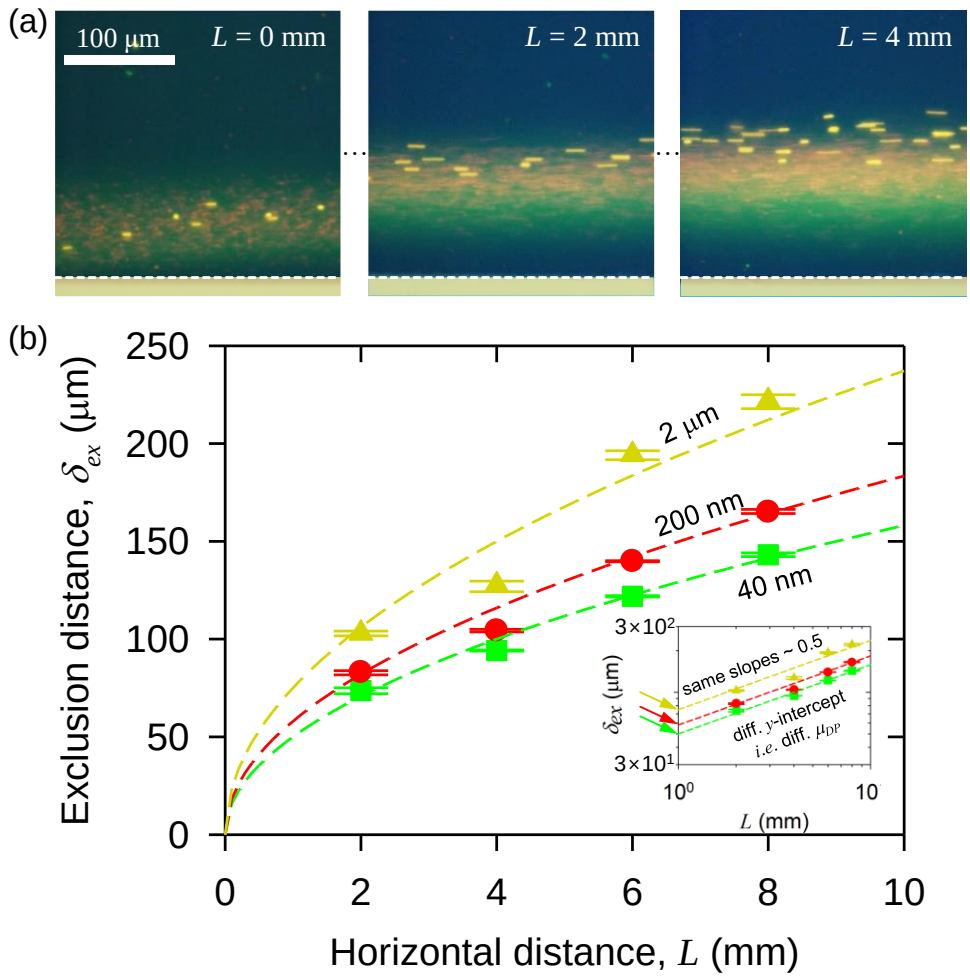

Figure 4.3. (a) The exclusion and separation of particles with diameter of 40 nm, 200 nm and 2 μm at L = 0 mm, 2 mm and 4 mm each. (b) The exclusion distance of particles with different sizes as function of horizontal distance L. The inset showed the scaling law of δ_{ex} and L, denoting the same slope (*i.e.* the same power) and different y-intercepts (*i.e.* different μ_{DP}).

4.3.4. Separation Efficiency Improvement by Enhanced Concentration Gradient

The particle suspension was dispersed over 100 μm width as shown in Figure 4.2(a) and 4.3(a), even if the suspension was injected through the sample stream of which width was 60 μm. They were dispersed by inevitable hydrodynamic broadening and diffusion[159]. Thus, multiple groups of nanoparticles with different average positions should be overlapped by this dispersion so that one need to increase the exclusion distance for enhancing the separation efficiency by steeper concentration gradient. In order to achieve this, Tris buffer as a proton scavenger was added in the buffer solution, not in sample solution. Exchanged H^+ from the ion exchange medium was rapidly taken by Tris so that Tris can further reduce the concentration of H^+ inside the concentration boundary layer, *i.e*. achieving steeper concentration gradient. As a result, the exclusion distance for each nanoparticle significantly increased. As shown in Figure 4.4(a), the exclusion distance of 40 nm particles increased by 65 %, 200 nm particles increased by 76 % and 2 μm particles increased by 85 % in the case of NaCl + Tris solution. The snapshots were taken at L = 6 mm. The inter-particle distance between 40 nm – 200 nm particle suspensions increased by 270 %, 200 nm – 2 μm particle suspensions increased by 600 % and 20 nm – 2 μm particle suspensions increased by 260 %.

The separation resolution (R_s) is a parameter, defining the amount of particles that are overlapped. We calculated R_s to estimate the separation efficiency between each particle suspensions. The particle bandwidth (w) and the intensity peak position (p) were obtained from the Gaussian fitting to calculate separation resolution

($R_s = \frac{2(p_2 - p_1)}{w_1 + w_2}$)[160]. R_s over 0.5 means that two groups are overlapped less than 15.8 %. As shown in Figure 4.4(b), R_s between particles groups increased and saturated as the concentration of Tris in buffer solution increased. Because the amount of H^+ from the medium was limited, the higher concentration of Tris than 1 mM was ineffective to the enhancement, leading to the saturation behavior. Note that the numerical results about the ion concentration with injection of Tris is described in Appendix A.

Furthermore, Tris can play an effective role to regulate pH inside the concentration boundary layer. Because H^+ is continuously released from the medium, significantly low pH has been regarded as a nuisance in this spontaneous diffusiophoretic separation method[152, 155]. Tris has been conventionally used in biochemistry and molecular biology as a component of pH buffer, holding pH values between 7.1 and 9.1 at room temperature[161]. The effect of Tris addition on pH changes was shown in Figure 4.5. The pH of produced NaCl solution was 4, which is not appropriate to be used as physiological buffer. However, in presence of Tris in the buffer solution, pH of produced solution was 7.5 so that it was compatible for pH-sensitive bio-samples. In addition, ΔpH of NaCl+Tris solution was half of that of NaCl solution. From these observations, we can conclude that the use of Tris in buffer solution can not only promote the separation efficiency but also provide bio-compatible environment in continuous and spontaneous diffusiophoretic separation method.

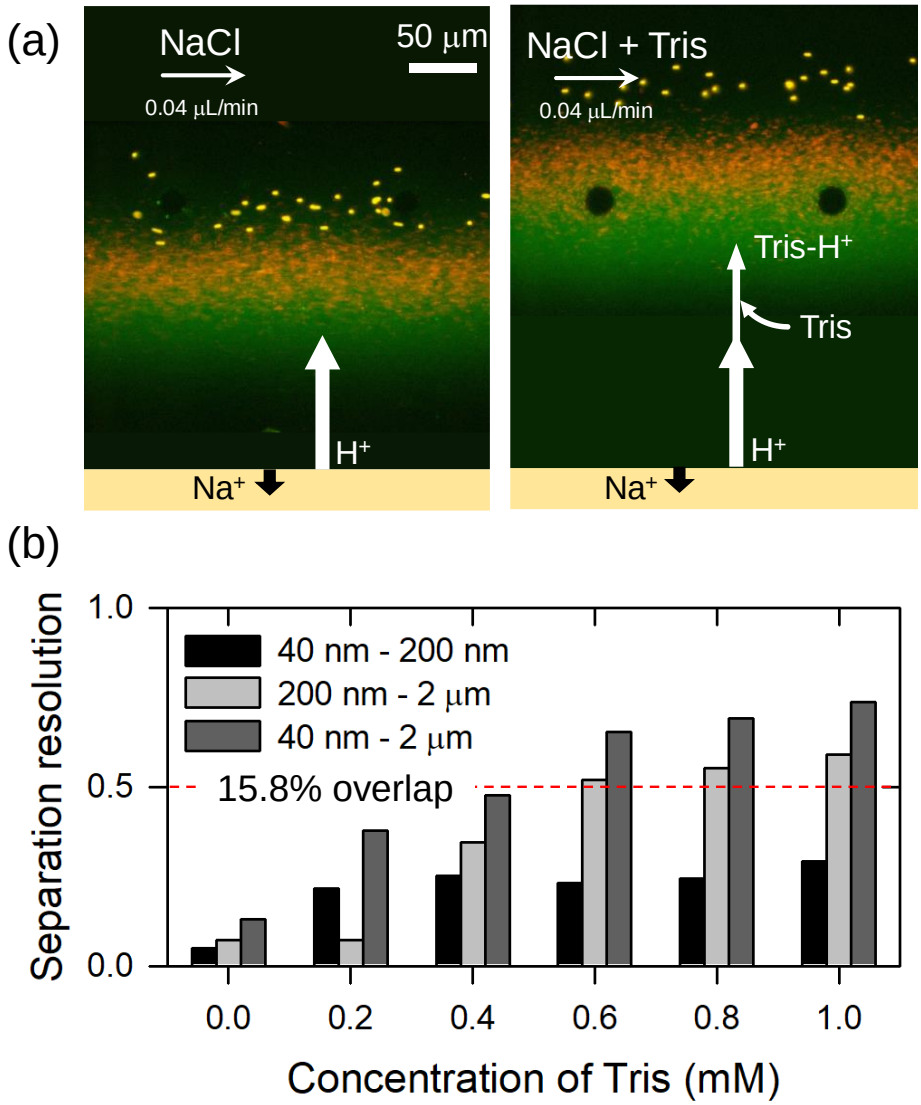

Figure 4.4. (a) Snapshots of multiple particle separation in NaCl and NaCl + Tris solution. At the same longitudinal position, the exclusion distance of particle suspensions and the distance between each particle suspensions increased. (b) Separation resolution of inter-particles as a function of the concentration of Tris contained in the buffer solution.

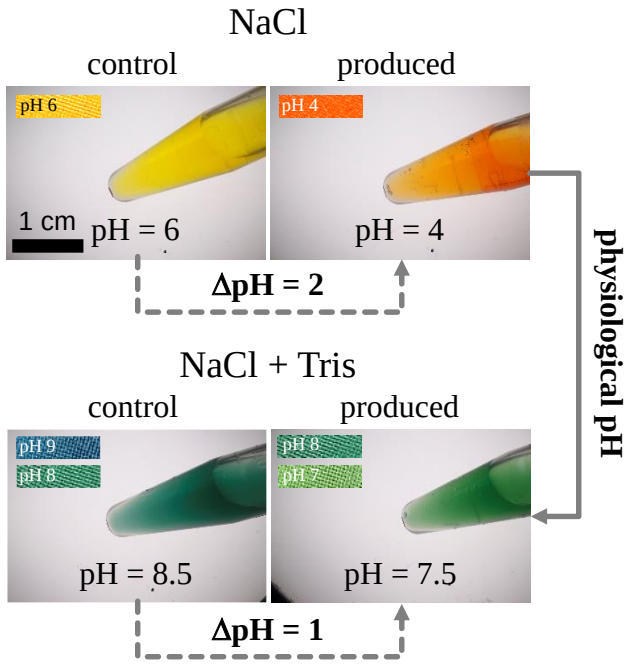

Figure 4.5. The pH of the control and the produced solutions of 1 mM NaCl solution and 1 mM NaCl + 1 mM Tris solution, respectively.

4.4. Conclusions

In this chapter, we demonstrated a continuous separation based on diffusiophoresis with spontaneously generated concentration gradient in a microfluidic platform. The exclusion distance of particles was shown to follow the scaling law of the conventional diffusiophoretic system. From this scale law, we found that particle with different μ_{DP} can have its distinct exclusion distance so that the particles of 40 nm, 200 nm and 2 μm were separated. However, the separation resolution between the particle suspensions was too low to be evaluated as sufficient separation. Thus, in order to increase the separation efficiency, Tris buffer as a proton scavenger was added in the buffer stream so that the concentration gradient inside the concentration boundary layer became steeper. As a result, the separation resolutions were significantly enhanced. Furthermore, since Tris played an essential role as a pH regulator, pH of produced stream was appropriate for most of pH-sensitive biomolecules. Therefore, we expected the suggested continuous and spontaneous diffusiophoretic separation platform to be useful for analyzing various nano-meter scale bio-particles.

Chapter 5. Concluding Remarks

In this thesis, we discussed about the electrokinetic phenomena induced by ion selectivity which is unique characteristics of nanochannels. First, we presented a fabrication method for a micro/nanofluidic device with an arbitrary-shaped nanoporous membrane. Using the patterning method, nanoporous membranes were patterned along microchannels with shapes of square, sine, sawtooth, triangle and fractal wave. Since the accuracy of the membrane patterning was confirmed by direct visualization of ICP, the fluidic motions of three mechanisms in ICP were visualized in microchannels with depth of 5 μm, 15 μm and 150 μm. Furthermore, through direct visualization and electrical measurements, it was confirmed that the undulation of the membrane surface differently effects in EOF regime and EOI regime. Secondly, we fabricated a micro/nanofluidic platform with reinforcing structures inside ion selective membrane using the presented nanoporous membrane patterning method. Through numerical simulation and experiments, the stable electroconvection was aligned with the reinforcements and the conditions of reinforcement geometry for the vortex alignment was confirmed. Moreover, the reinforcements contributed to the alignment and stabilization of electroconvection in chaotic regime. The stabilization was demonstrated with the electric measurements and quantification with time-averaged profiles of cation concentration in simulation and fluorescence intensity in experiment. It was confirmed that electroconvection was stabilized when the reinforcement is wide and close to ion depletion zone, similar to the stable regime. Finally, we developed a continuous and spontaneous nanoparticle separator based on diffusiophoresis induced by ion exchange. We

demonstrated that the developed diffusiophoretic nanoparticle separator followed the scaling law of the conventional diffusiophoretic system. Using the scaling law, the nanoparticles with different diffusiophoretic mobility (carboxylate-modified 40 nm, 200 nm and 2 μm particles) was separated. To increase the separation resolution, Tris buffer was injected to enhanced concentration gradient. Consequently, pH in the separated stream was regulated with the addition of Tris. In summary, we investigated the concentration boundary layers formed near nanoporous membranes which have not been fabricated due to the limitations of conventional fabrication techniques. Therefore, we suggest that this thesis would broaden the knowledge for fabrication of near-practical micro/nanofluidic platforms and the electrokinetic phenomena inside the platforms.

Appendix

Appendix A as courtesy of Prof. Hyomin Lee.

Appendix A. Numerical Modeling of Concentration Boundary Layer near the Ion-selective Membrane with Water Absorption

A.1. Numerical Methods

A.1.1. 2D Numerical Model for Diffusiophoretic Separation

To model and analyze the diffusiophoretic separation device as shown in Figure 4.1, coupled mass transport equations and electroneutral constraint was numerically simulated. Inside the microchannel, following self-ionization reaction of water would occur as

$$\mathrm{H_2O} \rightleftarrows \mathrm{H^+ + OH^-}. \tag{A.1}$$

For the simplicity, the hydration reaction of CO_2 was neglected so that the pH condition of inlet stream was assumed to be 7. Since the actual condition of inlet stream was pH 6, the assumption of neutral pH would be proper to reduce a computational cost. In the microchannel filled with NaCl electrolyte, there were 5 dissolved species as Na^+, Cl^-, H^+, OH^-, and colloidal particle. The transport phenomenon of each species was governed by the Nernst-Planck equation as

$$-\nabla \cdot \left(-D_{Na} \nabla c_{Na} - \frac{F D_{Na}}{RT} c_{Na} \nabla \phi + c_{Na} \mathbf{u} \right) = 0, \tag{A.2}$$

$$-\nabla\cdot\left(-D_{Cl}\nabla c_{Cl}+\frac{FD_{Cl}}{RT}c_{Cl}\nabla\phi+c_{Cl}\mathbf{u}\right)=0\,, \tag{A.3}$$

$$-\nabla\cdot\left(-D_{H}\nabla c_{H}-\frac{FD_{H}}{RT}c_{H}\nabla\phi+c_{H}\mathbf{u}\right)+k_{w}^{b}\left(K_{w}-c_{H}c_{OH}\right)=0\,, \tag{A.4}$$

$$-\nabla\cdot\left(-D_{OH}\nabla c_{OH}+\frac{FD_{OH}}{RT}c_{OH}\nabla\phi+c_{OH}\mathbf{u}\right)+k_{w}^{b}\left(K_{w}-c_{H}c_{OH}\right)=0 \quad \text{and} \tag{A.5}$$

$$-\nabla\cdot\left(-D_{p}\nabla c_{p}+\mu_{DP}c_{p}\nabla\ln c\right)=0 \tag{A.6}$$

where c_i is the concentration of i-th species (subscription 'p' means colloidal particle), t is the time, D_i is the diffusivity of i-th species, F is the Faraday constant, R is the gas constant, T is the absolute temperature, ϕ is the electric potential, **u** is the flow field, k_w^b is the rate constant of backward reaction of self-ionization reaction as denoted in equation (A.1), K_w is the equilibrium constant of the water reaction, μ_{DP} is the diffusiophoretic mobility of colloidal particle and c is the total ion concentration. The electric potential should be needed for describing ion-ion interactions to retain local electroneutrality inside the electrolytic solution. Instead of solving the Poisson equation to obtain the potential distribution, local electroneutral constraint was introduced as

$$c_{Na}-c_{Cl}+c_{H}-c_{OH}=0\,. \tag{A.7}$$

Utilizing above constraint, c can be defined as $c = c_{Na} + c_H$. Additionally, the flow field **u** was set to be the Poiseuille flow.

$$\mathbf{u}=6\frac{Q}{A}\left(\frac{y}{H}-\frac{y^{2}}{H^{2}}\right)\mathbf{e}_{x} \tag{A.8}$$

where Q is the flow rate, A is the cross-sectional area of actual microchannel and H is the height of microchannel.

Equations of (A.2) – (A.8) as the governing equations and constraints were completed with following boundary conditions. At inlet, the bulk reservoir conditions were given as

$$c_{Na} = c_{Cl} = 1\ \text{mM},\ \ c_H = c_{OH} = 100\,\text{nM} \ \text{ and } \ c_p = 1\ \text{nM}. \tag{A.9}$$

At outlet,

$$\mathbf{n}\cdot\nabla c_i = 0 \tag{A.10}$$

for all species. Equation (A.10) means that dissolved species went through the outlet boundary by convective transport only. At wall, no-penetration conditions were employed as

$$\mathbf{n}\cdot\left(-D_i\nabla c_i - \frac{z_i F D_i}{RT} c_i \nabla\phi\right) = 0 \ \text{ for ionic species and} \tag{A.11}$$

$$\mathbf{n}\cdot\left(-D_p\nabla c_p + \mu_{DP} c_p \nabla \ln c\right) = 0 \ \text{ for colloidal particle} \tag{A.12}$$

where **n** is the outward normal vector and z_i is the ion valence of i-th species. At cation-exchange surface, the boundary conditions were

$$\mathbf{n}\cdot\left(-D_{Na}\nabla c_{Na} - \frac{F D_{Na}}{RT} c_{Na}\nabla\phi\right) = k_{ex} c_{Na}, \tag{A.13}$$

$$\mathbf{n}\cdot\left(-D_{Cl}\nabla c_{Cl} + \frac{F D_{Cl}}{RT} c_{Cl}\nabla\phi\right) = 0, \tag{A.14}$$

$$\mathbf{n}\cdot\left(-D_H\nabla c_H - \frac{F D_H}{RT} c_H \nabla\phi\right) = -k_{ex} c_{Na}, \tag{A.15}$$

$$\mathbf{n}\cdot\left(-D_{OH}\nabla c_{OH} + \frac{F D_{OH}}{RT} c_{OH}\nabla\phi\right) = 0 \ \text{ and} \tag{A.16}$$

$$\mathbf{n}\cdot\left(-D_p\nabla c_p + \mu_{DP} c_p \nabla \ln c\right) = 0. \tag{A.17}$$

Equation (A.13) and (A.15) represent 1:1 ion exchange process [162]. Equation

(A.14), (A.16) and (A.17) are no-penetration conditions.

Governing equations of equation (A.2) – (A.6), constraints of equation (A.7) – (A.8) and boundary conditions of equation (A.9) – (A.17) were solved by COMSOL Multiphysics software under steady-state condition. Used parameter values in numerical model were summarized in Table A.1. Numerical results of diffusiophoretic exclusion were shown in Figure A.1 and Figure A.2.

A.1.2. 1D Numerical Model for Concentration Boundary Layer with Tris Buffer

Comparing to 2D model, 1D model can further reduce computational cost. Therefore, in 1D modeling, we introduced other possible reactions such as hydration reaction of CO_2 [163] and Tris buffer reaction.

$$CO_2 + H_2O \rightleftarrows H^+ + HCO_3^- \tag{A.18}$$

$$TrisH^+ \rightleftarrows Tris + H^+ \tag{A.19}$$

The rate constants of equation (A.18) are $k_{CO2}^f = 3.7 \times 10^{-2}$ s^{-1} for forward reaction and $kCO_2^b = 18$ s^{-1} for backward reaction [163]. For equation (A.19), the rate constants were determined by the Smoluchowski-Debye theory [164]. The rate constant of backward reaction for equation (A.19), k_{TrisH}^b can be represented as

$$k_{TrisH}^b = 4\pi N_A \left(D_{Tris} + D_H \right) r_{AB} \tag{A.20}$$

where N_A is the Avogadro number, D_{Tris} is the diffusivity of Tris and r_{AB} is the reaction distance between reactant A and B. Since $r_{AB} \sim 0.2$ nm typically, $k_{TrisH}^b = 1.56 \times 10^7$ m^3 mol^{-1} s^{-1} with $D_{Tris} = 1 \times 10^{-9}$ m^2 s^{-1}. Furthermore, p$K_a = 8.07$ for Tris reaction so that $k_{TrisH}^f = K_a \, k_{TrisH}^b$.

The governing equations for ion exchange with Tris buffer were

$$-\frac{d}{dx}\left(-D_{Na}\frac{dc_{Na}}{dx}-\frac{FD_{Na}}{RT}c_{Na}\frac{d\phi}{dx}\right)=0, \tag{A.21}$$

$$-\frac{d}{dx}\left(-D_{Cl}\frac{dc_{Cl}}{dx}+\frac{FD_{Cl}}{RT}c_{Cl}\frac{d\phi}{dx}\right)=0, \tag{A.22}$$

$$\begin{aligned}&-\frac{d}{dx}\left(-D_{H}\frac{dc_{H}}{dx}-\frac{FD_{H}}{RT}c_{H}\frac{d\phi}{dx}\right)+k_{w}^{b}\left(K_{w}-c_{H}c_{OH}\right)\\&+\left(k_{CO2}{}^{f}c_{CO2}-k_{CO2}{}^{b}c_{H}c_{HCO3}\right)+\left(k_{TrisH}{}^{f}c_{TrisH}-k_{TrisH}{}^{b}c_{Tris}c_{H}\right)=0,\end{aligned} \tag{A.23}$$

$$-\frac{d}{dx}\left(-D_{OH}\frac{dc_{OH}}{dx}+\frac{FD_{OH}}{RT}c_{OH}\frac{d\phi}{dx}\right)+k_{w}^{b}\left(K_{w}-c_{H}c_{OH}\right)=0, \tag{A.24}$$

$$-\frac{d}{dx}\left(-D_{CO2}\frac{dc_{CO2}}{dx}\right)=0, \tag{A.25}$$

$$-\frac{d}{dx}\left(-D_{HCO3}\frac{dc_{HCO3}}{dx}+\frac{FD_{HCO3}}{RT}c_{HCO3}\frac{d\phi}{dx}\right)+\left(k_{CO2}{}^{f}c_{CO2}-k_{CO2}{}^{b}c_{H}c_{HCO3}\right)=0, \tag{A.26}$$

$$-\frac{d}{dx}\left(-D_{TrisH}\frac{dc_{TrisH}}{dx}-\frac{FD_{TrisH}}{RT}c_{TrisH}\frac{d\phi}{dx}\right)+\left(k_{TrisH}{}^{f}c_{TrisH}-k_{TrisH}{}^{b}c_{Tris}c_{H}\right)=0 \quad \text{and} \tag{A.27}$$

$$-\frac{d}{dx}\left(-D_{Tris}\frac{dc_{Tris}}{dx}\right)=0. \tag{A.28}$$

In the case of 1D formulation, the electric potential was directly determined by solving the Poisson equation as

$$-\varepsilon\frac{d^{2}\phi}{dx^{2}}=F\left(c_{Na}-c_{Cl}+c_{H}-c_{OH}+c_{TrisH}-c_{HCO3}\right). \tag{A.29}$$

The boundary conditions at bulk interface (*i.e.* end of concentration boundary layer) were

$$c_{Na}=c_{Cl}=1\ \text{mM},\ c_{H}=10^{-pH}\ \text{M},\ c_{OH}=10^{-14+pH}\ \text{M},\ c_{CO2}=\frac{k_{CO2}{}^{b}}{k_{CO2}{}^{f}}c_{H}c_{HCO3},$$

$$c_{HCO3} = c_H + c_{TrisH} - c_{OH}\,,\quad c_{TrisH} = \frac{c_{buffer}}{1+\frac{k_{TrisH}{}^{f}}{k_{TrisH}{}^{b}}\frac{1}{c_H}}\,,$$

$$c_{Tris} = \frac{c_{buffer}}{1+\frac{k_{TrisH}{}^{b}}{k_{TrisH}{}^{f}}c_H} \quad \text{and} \quad \phi = 0 \tag{A.30}$$

where c_{buffer} is the initial concentration of Tris before progressing reaction of equation (A.19). In 1D simulation, c_{buffer} was set to be 1 mM. The boundary conditions at cation-exchange surface were

$$-D_{Na}\frac{dc_{Na}}{dn} - \frac{FD_{Na}}{RT}c_{Na}\frac{d\phi}{dn} = k_{ex}c_{Na}\,, \tag{A.31}$$

$$-D_{Cl}\frac{dc_{Cl}}{dn} + \frac{FD_{Cl}}{RT}c_{Cl}\frac{d\phi}{dn} = 0\,, \tag{A.32}$$

$$-D_{H}\frac{dc_{H}}{dn} - \frac{FD_{H}}{RT}c_{H}\frac{d\phi}{dn} = -k_{ex}c_{Na}\,, \tag{A.33}$$

$$-D_{OH}\frac{dc_{OH}}{dn} + \frac{FD_{OH}}{RT}c_{OH}\frac{d\phi}{dn} = 0\,, \tag{A.34}$$

$$-D_{CO2}\frac{dc_{CO2}}{dn} = 0\,, \tag{A.35}$$

$$-D_{HCO3}\frac{dc_{HCO3}}{dn} + \frac{FD_{HCO3}}{RT}c_{HCO3}\frac{d\phi}{dn} = 0\,, \tag{A.36}$$

$$-D_{TrisH}\frac{dc_{TrisH}}{dn} - \frac{FD_{TrisH}}{RT}c_{TrisH}\frac{d\phi}{dn} = 0\,, \tag{A.37}$$

$$-D_{Tris}\frac{dc_{Tris}}{dn} = 0 \quad \text{and} \tag{A.38}$$

$$\phi = -100\ \text{mV} \tag{A.39}$$

where operator d/dn means normal derivative. The condition of equation (A.39) was referred from [162].

A.2. Results and Discussions

A.2.1. Taylor Dispersion of the Nanoparticle Suspensions

To investigate further for the relationship between δ_{ex} and the flow rate, we conducted a numerical simulation. See details of simulation on Methods section. As shown in Figure A.1(a)-A.1(b), we confirmed that the concentration boundary layer reduces as the flow rate increases by the numerical simulation. However, as we analyzed in the inset of Figure 4.2(b), δ_{ex} is linearly proportional to $(L/U_{mean})^{0.5}$, which means the same δ_{ex} can be maintained as a combination of L and U_{mean}. For example, processing 50 μL sample takes 10 hours with Q = 0.04 μL/min. However, processing the same amount of sample may take 1 hour with 10 times faster flow rate and 10 times longer microchannel (*i.e.* Q = 0.4 μL/min and 8 cm microchannel).

On the other hand, the effective diffusivity (D_{eff}) by Taylor dispersion is scaled with the square of the flow rate. If there is the Taylor dispersion, the effective diffusivity of colloidal particle can be represented by $D_{eff} = D_p(1 + Pe^2 / 48)$ where Pe is the particle Peclet number[165]. The major point is whether Taylor dispersion is serious or not in this chapter. The bandwidth (w) of diffusive plug is scaled by $w \sim (D_{eff}t)^{0.5}$ where t means the retention time in channel and scaled with Q^{-1}. Since $Pe \sim Q$ and $t \sim Q^{-1}$, w is proportional to $Q^{0.5}$ at high Pe limit. This scaling analysis implies that band broadening become severe if Q increases. However, as shown in Figure 4.3(c) which was obtained by 2D numerical model, increasing Q resulted in decreasing bandwidth. This is because $D_{eff} \approx D_p$ at low or zero Peclet number limit so that $w \sim$

$Q^{-0.5}$ (*i.e.* $w = (D_{eff}\, t)^{0.5} \sim (D_p \,/\, Pe)^{0.5} \sim Q^{-0.5}$). Furthermore, the bandwidth of the numerical simulation was well-agreed with the experimental data shown in Figure 4.3(c). In the meantime, the bandwidths calculated by the theory of diffusion without considering Taylor dispersion (area plot) and experimentally measured (bar plot) were well-agreed with each other as shown in Figure A.1(d)-A.1(f). From this analysis, we can conclude that Taylor dispersion is negligible in our system since the direction of the flow in microchannel is perpendicular to the direction of the particle dispersion (*i.e.* zero Peclet number limit).

As stated in previous paragraph, our system laid on low (or zero) Peclet number regime. While D_{eff} would be proportional to $1/D_p$ in high Peclet number limit, $D_{eff} \propto D_p$ in low (or zero) Peclet number limit, leading to a negligible Taylor dispersion. This was also experimentally confirmed that the bandwidths of the larger particles (low D_p) were thinner than ones of the smaller particles (high D_p) by comparing Figure A.2(a)-A.2(c).

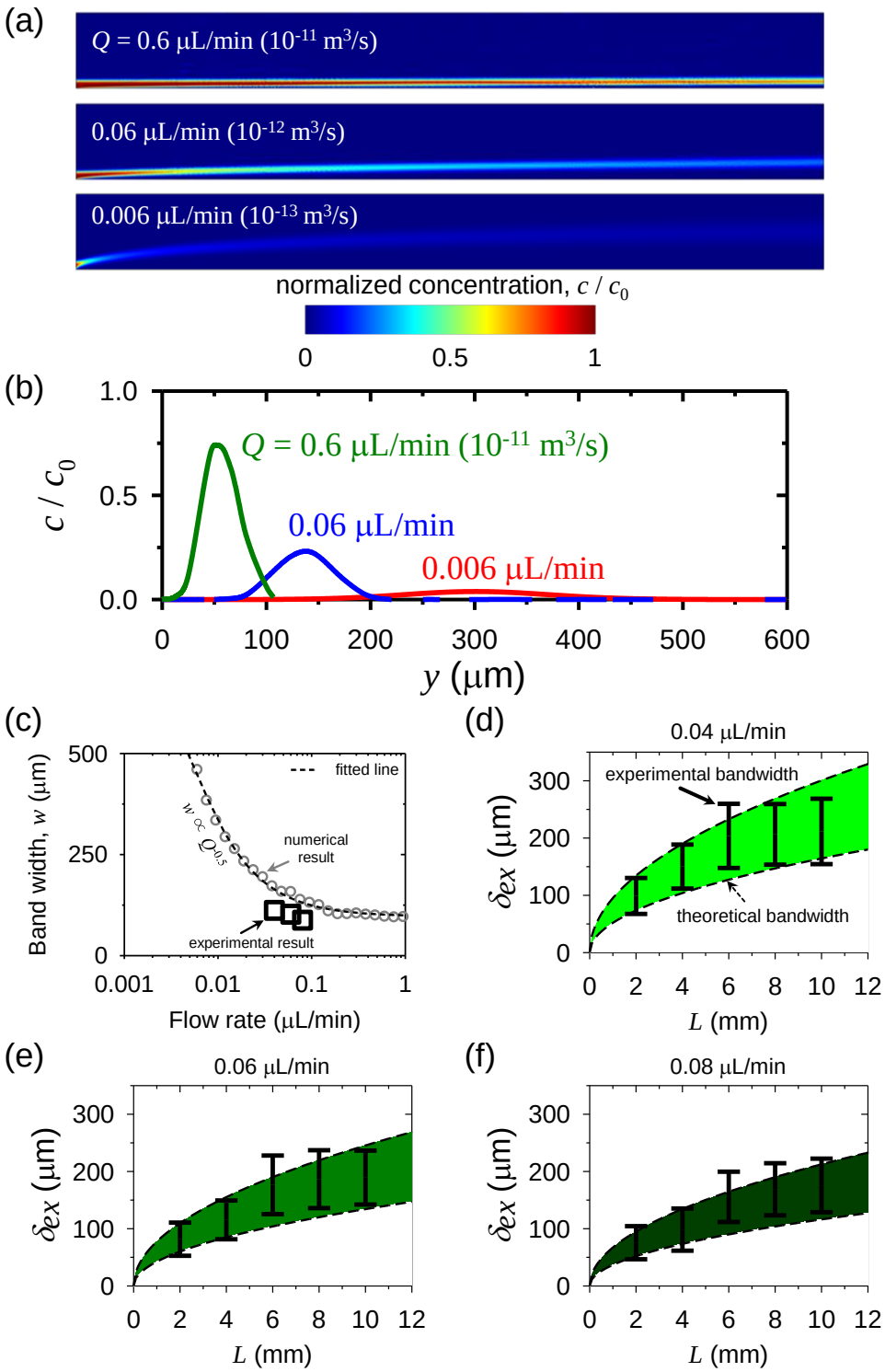
(a)
Q = 0.6 μL/min (10-11 m3/s)
0.06 μL/min (10-12 m3/s)
0.006 μL/min (10-13 m3/s)
normalized concentration, c / c0
0
0.5
1
(b)
1.0
0.5
0.0
c / c0
Q = 0.6 μL/min (10-11 m3/s)
0.06 μL/min
0.006 μL/min
0
100
200
300
400
500
600
y (μm)
(c)
500
250
0
Band width, w (μm)
fitted line
w ∝ Q0.5
numerical result
experimental result
0.001
0.01
0.1
1
Flow rate (μL/min)
(d)
0.04 μL/min
300
200
100
0
δex (μm)
experimental bandwidth
theoretical bandwidth
0
2
4
6
8
10
12
L (mm)
(e)
0.06 μL/min
300
200
100
0
δex (μm)
0
2
4
6
8
10
12
L (mm)
(f)
0.08 μL/min
300
200
100
0
δex (μm)
0
2
4
6
8
10
12
L (mm)

Figure A.1. (a) The diffusiophoretic exclusion of colloidal particle stream with various flow rate. The particle concentration was normalized by c_{p0} = 1 nM. The flow direction was from left to right. The colloidal particle was assumed to be 40 nm diameter so that its diffusivity was about 10^{-11} m^2 s^{-1}. The total length of microchannel in this simulation was 6 mm. (b) Concentration profiles of colloidal particle which is evaluated at outlet (right boundary). (c) The bandwidth of diffusiophoretically excluded colloidal particles as a function of flow rate. Numerical results (circles) were fitted as $w \sim Q^{-0.5}$, which reflected the Taylor dispersion is negligible. The fitted line was matched with experimental data (rectangles). (d)-(f) Comparison of experimentally measured bandwidth to the theory of diffusion without considering Taylor dispersion for Q = 0.04, 0.06 and 0.08 μL/min, respectively.

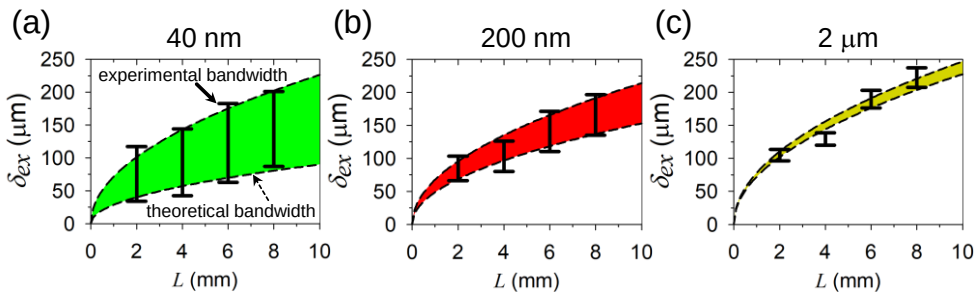

Figure A.2. (a)-(c) Comparison of experimentally measured bandwidth to the theory of diffusion without considering Taylor dispersion for particles of 40, 200 and 2,000 nm, respectively. The bandwidths of the larger particles were thinner than ones of the smaller particles.

A.2.2. Numerical Results of Ion Concentration with Injection of Tris

By the 1D numerical simulation (See details of simulation on section A.1), the total cation concentration ($c_{net} = c_{Na} + c_H + c_{TrisH}$) became lower in the case with Tris (red dash line) as shown in Figure A.3. Furthermore, normalized diffusiophoretic migration term ($\delta_c \nabla \ln(c_{net}/c_{net0})$) was significantly enhanced when Tris buffer was added to the buffer solution. These results confirmed that the addition of Tris would enhance the diffusiophoretic migration as we experimentally measured.

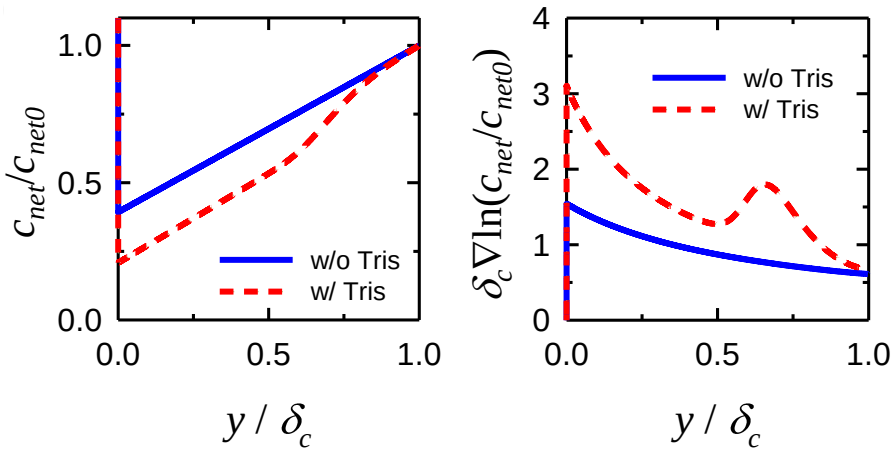

Figure A.3. Numerically simulated effect of Tris addition to the buffer solution. The gradient of total cation concentration and diffusiophoretic migration term would be significantly enhanced.

Table A.1. Parameters used for the numerical simulation.

Parameter	Values	Description	Reference
L	6 mm	x-directional length of domain	
H	600 μm	y-directional height of domain	
A	600 μm × 15 μm	cross-sectional area of microchannel	
Q	0.001 – 1 μL min^{-1}	flow rate	
D_{Na}	1.33×10^{-9} m^2 s^{-1}	Na^+ diffusivity	[1]
D_{Cl}	2.03×10^{-9} m^2 s^{-1}	Cl^- diffusivity	[1]
D_H	9.31×10^{-9} m^2 s^{-1}	H^+ diffusivity	[1]
D_{OH}	5.26×10^{-9} m^2 s^{-1}	OH^- diffusivity	[1]
D_p	10^{-11} m^2 s^{-1}	particle diffusivity	
μ_{DP}	2×10^{-9} m^2 s^{-1}	diffusiophoretic mobility	
k_w^b	1.4×10^8 m^3 mol^{-1} s^{-1}	rate constant of water reaction	[166]
K_w	10^{-8} mol^2 m^6	equilibrium constant of water reaction	[166]
k_{ex}	3.08×10^{-6} m s^{-1}	rate constant of ion exchange	[162]

Bibliography

[1] J. H. Masliyah and S. Bhattacharjee, *Electrokinetic and Colloid Transport Phenomena*. Hoboken, NJ: Wiley, 2006.

[2] B. J. Kirby, *Micro-and nanoscale fluid mechanics: transport in microfluidic devices*. Cambridge university press, 2010.

[3] K. A. Mauritz and R. B. Moore, "State of understanding of Nafion," *Chemical reviews,* vol. 104, no. 10, pp. 4535-4586, 2004.

[4] S. J. Kim, Y. C. Wang, J. H. Lee, H. Jang, and J. Han, "Concentration polarization and nonlinear electrokinetic flow near a nanofluidic channel," *Phys Rev Lett,* vol. 99, no. 4, p. 044501, Jul 27 2007, doi: 10.1103/PhysRevLett.99.044501.

[5] E. V. Dydek, B. Zaltzman, I. Rubinstein, D. S. Deng, A. Mani, and M. Z. Bazant, "Overlimiting current in a microchannel," *Phys Rev Lett,* vol. 107, no. 11, p. 118301, Sep 9 2011, doi: 10.1103/PhysRevLett.107.118301.

[6] H. C. Chang, E. A. Demekhin, and V. S. Shelistov, "Competition between Dukhin's and Rubinstein's electrokinetic modes," *Phys Rev E Stat Nonlin Soft Matter Phys,* vol. 86, no. 4 Pt 2, p. 046319, Oct 2012, doi: 10.1103/PhysRevE.86.046319.

[7] S. S. Dukhin, "Electrokinetic phenomena of the second kind and their applications," *Advances in colloid and interface science,* vol. 35, pp. 173-196, 1991.

[8] I. Rubinstein and B. Zaltzman, "Electro-osmotically induced convection at a permselective membrane," *Physical Review E,* vol. 62, no. 2, p. 2238, 2000.

[9] I. Rubinstein and B. Zaltzman, "Electro-osmotic slip of the second kind and instability in concentration polarization at electrodialysis membranes," *Mathematical Models and Methods in Applied Sciences,* vol. 11, no. 02, pp. 263-300, 2001.

[10] S. M. Davidson, M. Wessling, and A. Mani, "On the Dynamical Regimes of Pattern-Accelerated Electroconvection," *Sci Rep,* vol. 6, p. 22505, Mar 3 2016, doi: 10.1038/srep22505.

[11] C. L. Druzgalski, M. B. Andersen, and A. Mani, "Direct numerical simulation of electroconvective instability and hydrodynamic chaos near an ion-selective surface," *Physics of Fluids,* vol. 25, no. 11, 2013, doi: 10.1063/1.4818995.

[12] S. Shin, J. T. Ault, J. Feng, P. B. Warren, and H. A. Stone, "Low-Cost Zeta Potentiometry Using Solute Gradients," *Adv Mater,* vol. 29, no. 30, Aug 2017, doi: 10.1002/adma.201701516.

[13] S. Shin *et al.*, "Size-dependent control of colloid transport via solute gradients in dead-end channels," *Proc Natl Acad Sci U S A,* vol. 113, no. 2, pp. 257-61, Jan 12 2016, doi: 10.1073/pnas.1511484112.

[14] D. C. Prieve, J. L. Anderson, J. P. Ebel, and M. E. Lowell, "Motion of a particle generated by chemical gradients. Part 2. Electrolytes," *J. Fluid Mech.,* vol. 148, pp. 247-269, 1984.

[15] T. Kniazeva, J. C. Hsiao, J. L. Charest, and J. T. Borenstein, "A microfluidic respiratory assist device with high gas permeance for artificial lung applications," *Biomedical microdevices,* vol. 13, no. 2, pp. 315-323, 2011.

[16] K. J. Morton *et al.*, "Crossing microfluidic streamlines to lyse, label and wash cells,"

Lab on a Chip, vol. 8, no. 9, pp. 1448-1453, 2008.
[17] R. Fan *et al.*, "Integrated barcode chips for rapid, multiplexed analysis of proteins in microliter quantities of blood," *Nature biotechnology,* vol. 26, no. 12, pp. 1373-1378, 2008.
[18] D. Tanaka *et al.*, "Microdroplet synthesis of azo compounds with simple microfluidics-based pH control," *RSC Advances,* vol. 10, no. 64, pp. 38900-38905, 2020.
[19] D. Welch and J. B. Christen, "Real-time feedback control of pH within microfluidics using integrated sensing and actuation," *Lab on a Chip,* vol. 14, no. 6, pp. 1191-1197, 2014.
[20] D. D. Huh, "A human breathing lung-on-a-chip," *Ann Am Thorac Soc,* vol. 12 Suppl 1, pp. S42-4, Mar 2015, doi: 10.1513/AnnalsATS.201410-442MG.
[21] J. Yoon, V. Q. Do, V.-S. Pham, and J. Han, "Return flow ion concentration polarization desalination: A new way to enhance electromembrane desalination," *Water research,* vol. 159, pp. 501-510, 2019.
[22] B. Kim, H. Kwon, S. H. Ko, G. Lim, and J. Han, "Partial desalination of hypersaline brine by lab-scale ion concentration polarization device," *Desalination,* vol. 412, pp. 20-31, 2017.
[23] S. J. Kim, S. H. Ko, K. H. Kang, and J. Han, "Direct seawater desalination by ion concentration polarization," *Nat Nanotechnol,* vol. 5, no. 4, pp. 297-301, Apr 2010, doi: 10.1038/nnano.2010.34.
[24] H. Lee, J. Kim, J. Yang, S. W. Seo, and S. J. Kim, "Diffusiophoretic exclusion of colloidal particles for continuous water purification," *Lab Chip,* vol. 18, no. 12, pp. 1713-1724, Jun 12 2018, doi: 10.1039/c8lc00132d.
[25] J. Choi, H. Lee, and S. J. Kim, "Hierarchical micro/nanoporous ion-exchangeable sponge," *Lab on a Chip,* vol. 20, no. 3, pp. 505-513, 2020.
[26] S. Park *et al.*, "Capillarity ion concentration polarization as spontaneous desalting mechanism," *Nat Commun,* vol. 7, p. 11223, Apr 1 2016, doi: 10.1038/ncomms11223.
[27] W. Kim *et al.*, "Nanoelectrokinetic purification device for a continuous peritoneal dialysate recycler," in *2017 IEEE 30th International Conference on Micro Electro Mechanical Systems (MEMS)*, 2017: IEEE, pp. 319-322.
[28] L. Gurreri *et al.*, "Electrodialysis with asymmetrically profiled membranes: Influence of profiles geometry on desalination performance and limiting current phenomena," *Desalination,* vol. 506, 2021, doi: 10.1016/j.desal.2021.115001.
[29] R. Kwak, G. Guan, W. K. Peng, and J. Han, "Microscale electrodialysis: Concentration profiling and vortex visualization," *Desalination,* vol. 308, pp. 138-146, 2013, doi: 10.1016/j.desal.2012.07.017.
[30] P. Zhang *et al.*, "Nanochannel-Based Transport in an Interfacial Memristor Can Emulate the Analog Weight Modulation of Synapses," *Nano Lett,* vol. 19, no. 7, pp. 4279-4286, Jul 10 2019, doi: 10.1021/acs.nanolett.9b00525.
[31] D. Mijatovic, J. C. Eijkel, and A. van den Berg, "Technologies for nanofluidic systems: top-down vs. bottom-up--a review," *Lab Chip,* vol. 5, no. 5, pp. 492-500, May 2005, doi: 10.1039/b416951d.
[32] V. G. Kutchoukov, F. Laugere, W. van der Vlist, L. Pakula, Y. Garini, and A. Bossche, "Fabrication of nanofluidic devices using glass-to-glass anodic bonding," *Sensors and Actuators A: Physical,* vol. 114, no. 2-3, pp. 521-527, 2004, doi: 10.1016/j.sna.2003.12.027.
[33] P. Mao and J. Han, "Fabrication and characterization of 20 nm planar nanofluidic

channels by glass–glass and glass–silicon bonding," *Lab on a Chip,* vol. 5, no. 8, pp. 837-844, 2005.

[34] P. Mao and J. Han, "Massively-Parallel Ultra-High-Aspect-Ratio Nanochannels as Mesoporous Membranes," *Lab Chip,* vol. 9, no. 4, pp. 586-591, 2009, doi: 10.1039/B809370A.

[35] J. Kim, I. Cho, H. Lee, and S. J. Kim, "Ion Concentration Polarization by Bifurcated Current Path," *Sci Rep,* vol. 7, no. 1, p. 5091, Jul 11 2017, doi: 10.1038/s41598-017-04646-0.

[36] H. Lee, J. Kim, H. Kim, H. Y. Kim, H. Lee, and S. J. Kim, "A concentration-independent micro/nanofluidic active diode using an asymmetric ion concentration polarization layer," *Nanoscale,* vol. 9, no. 33, pp. 11871-11880, Aug 24 2017, doi: 10.1039/c7nr02075a.

[37] J. H. Lee, Y. A. Song, and J. Han, "Multiplexed proteomic sample preconcentration device using surface-patterned ion-selective membrane," *Lab Chip,* vol. 8, no. 4, pp. 596-601, Apr 2008, doi: 10.1039/b717900f.

[38] G. M. Whitesides and J. C. Love, "The art of building small," *Scientific american,* vol. 285, no. 3, pp. 38-47, 2001.

[39] V. Nikonenko, A. Nebavsky, S. Mareev, A. Kovalenko, M. Urtenov, and G. Pourcelly, "Modelling of ion transport in electromembrane systems: Impacts of membrane bulk and surface heterogeneity," *Applied Sciences,* vol. 9, no. 1, p. 25, 2019.

[40] N. D. Pismenskaya, E. V. Pokhidnia, G. Pourcelly, and V. V. Nikonenko, "Can the electrochemical performance of heterogeneous ion-exchange membranes be better than that of homogeneous membranes?," *Journal of Membrane Science,* vol. 566, pp. 54-68, 2018, doi: 10.1016/j.memsci.2018.08.055.

[41] V. V. Wagholikar *et al.*, "Modeling cell pair resistance and spacer shadow factors in electro-separation processes," *Journal of Membrane Science,* vol. 543, pp. 151-162, 2017, doi: 10.1016/j.memsci.2017.08.054.

[42] S. Bhattacharya, A. Datta, J. M. Berg, and S. Gangopadhyay, "Studies on surface wettability of poly(dimethyl) siloxane (PDMS) and glass under oxygen-plasma treatment and correlation with bond strength," *Journal of Microelectromechanical Systems,* vol. 14, no. 3, pp. 590-597, 2005, doi: 10.1109/jmems.2005.844746.

[43] H. Lee *et al.*, "dCas9-mediated Nanoelectrokinetic Direct Detection of Target Gene for Liquid Biopsy," *Nano Lett,* vol. 18, no. 12, pp. 7642-7650, Dec 12 2018, doi: 10.1021/acs.nanolett.8b03224.

[44] N. Rosenberg and C. Tirrell, "Limiting currents in membrane cells," *Industrial & Engineering Chemistry,* vol. 49, no. 4, pp. 780-784, 1957.

[45] S. Nam *et al.*, "Experimental verification of overlimiting current by surface conduction and electro-osmotic flow in microchannels," *Phys Rev Lett,* vol. 114, no. 11, p. 114501, Mar 20 2015, doi: 10.1103/PhysRevLett.114.114501.

[46] C.-H. Chen, H. Lin, S. K. Lele, and J. G. Santiago, "Convective and absolute electrokinetic instability with conductivity gradients," *Journal of Fluid Mechanics,* vol. 524, pp. 263-303, 2005.

[47] S. Mehdizadeh, M. Yasukawa, T. Abo, Y. Kakihana, and M. Higa, "Effect of spacer geometry on membrane and solution compartment resistances in reverse electrodialysis," *Journal of Membrane Science,* vol. 572, pp. 271-280, 2019, doi: 10.1016/j.memsci.2018.09.051.

[48] B. De Jaegher, W. De Schepper, A. Verliefde, and I. Nopens, "A model-based analysis of electrodialysis fouling during pulsed electric field operation," *Journal of*

Membrane Science, vol. 642, 2022, doi: 10.1016/j.memsci.2021.119975.
[49] C. Druzgalski and A. Mani, "Statistical analysis of electroconvection near an ion-selective membrane in the highly chaotic regime," *Physical Review Fluids,* vol. 1, no. 7, 2016, doi: 10.1103/PhysRevFluids.1.073601.
[50] S. Sensale, Z. Ramshani, S. Senapati, and H.-C. Chang, "Universal Features of Non-equilibrium Ionic Currents through Perm-Selective Membranes: Gating by Charged Nanoparticles/Macromolecules for Robust Biosensing Applications," *The Journal of Physical Chemistry B,* vol. 125, no. 7, pp. 1906-1915, 2021.
[51] H. Lee, "Electroconvective Instability on Undulated Ion-selective Surface," *Korean Chemical Engineering Research,* vol. 57, no. 5, pp. 735-742, 2019.
[52] T. Pundik, I. Rubinstein, and B. Zaltzman, "Bulk electroconvection in electrolyte," *Phys Rev E Stat Nonlin Soft Matter Phys,* vol. 72, no. 6 Pt 1, p. 061502, Dec 2005, doi: 10.1103/PhysRevE.72.061502.
[53] F. Roghmans *et al.*, "2D Patterned Ion-Exchange Membranes Induce Electroconvection," *Advanced Materials Interfaces,* vol. 6, no. 1, 2018, doi: 10.1002/admi.201801309.
[54] Z. Slouka, S. Senapati, Y. Yan, and H.-C. Chang, "Charge inversion, water splitting, and vortex suppression due to DNA sorption on ion-selective membranes and their ion-current signatures," *Langmuir,* vol. 29, no. 26, pp. 8275-8283, 2013.
[55] Z. Wang *et al.*, "A Flexible and regenerative aptameric graphene–Nafion biosensor for cytokine storm biomarker monitoring in undiluted biofluids toward wearable applications," *Advanced Functional Materials,* vol. 31, no. 4, p. 2005958, 2021.
[56] J. Y. Chu, K. H. Lee, A. R. Kim, and D. J. Yoo, "Improved electrochemical performance of composite anion exchange membranes for fuel cells through cross linking of the polymer chain with functionalized graphene oxide," *Journal of Membrane Science,* vol. 611, p. 118385, 2020.
[57] T. Y. Son, D. J. Kim, V. Vijayakumar, K. Kim, D. S. Kim, and S. Y. Nam, "Anion exchange membrane using poly (ether ether ketone) containing imidazolium for anion exchange membrane fuel cell (AEMFC)," *Journal of Industrial and Engineering Chemistry,* vol. 89, pp. 175-182, 2020.
[58] V. Elumalai and D. Sangeetha, "Synergic effect of ionic liquid grafted titanate nanotubes on the performance of anion exchange membrane fuel cell," *Journal of Power Sources,* vol. 412, pp. 586-596, 2019.
[59] J. Veza, B. Peñate, and F. Castellano, "Electrodialysis desalination designed for off-grid wind energy," *Desalination,* vol. 160, no. 3, pp. 211-221, 2004.
[60] P. Sistat, P. Huguet, B. Ruiz, G. Pourcelly, S. A. Mareev, and V. V. Nikonenko, "Effect of pulsed electric field on electrodialysis of a NaCl solution in sub-limiting current regime," *Electrochimica Acta,* vol. 164, pp. 267-280, 2015, doi: 10.1016/j.electacta.2015.02.197.
[61] Q.-B. Chen, J. Wang, Y. Liu, J. Zhao, and P. Li, "Novel energy-efficient electrodialysis system for continuous brackish water desalination: innovative stack configurations and optimal inflow modes," *Water Research,* vol. 179, p. 115847, 2020.
[62] D. H. Jung, E. D. Han, B. H. Kim, and Y. H. Seo, "Ultra-thin ion exchange film on the ceramic supporter for output power improvement of reverse electrodialysis," *Sci Rep,* vol. 9, no. 1, p. 17440, Nov 25 2019, doi: 10.1038/s41598-019-54002-7.
[63] D. A. Vermaas, J. Veerman, M. Saakes, and K. Nijmeijer, "Influence of multivalent ions on renewable energy generation in reverse electrodialysis," *Energy Environ. Sci.,* vol. 7, no. 4, pp. 1434-1445, 2014, doi: 10.1039/c3ee43501f.

[64] J.-H. Han *et al.*, "Reverse electrodialysis (RED) using a bipolar membrane to suppress inorganic fouling around the cathode," *Water research,* vol. 166, p. 115078, 2019.

[65] A. Nazif, H. Karkhanechi, E. Saljoughi, S. M. Mousavi, and H. Matsuyama, "Recent progress in membrane development, affecting parameters, and applications of reverse electrodialysis: A review," *Journal of Water Process Engineering,* vol. 47, p. 102706, 2022.

[66] T. A. Saleh, M. Mustaqeem, and M. Khaled, "Developing water treatment technologies in removing heavy metals from wastewater: A review," *Environmental Nanotechnology, Monitoring & Management,* p. 100617, 2021.

[67] R. R. Raja Sulaiman, W. Y. Wong, and K. S. Loh, "Recent developments on transition metal–based electrocatalysts for application in anion exchange membrane water electrolysis," *International Journal of Energy Research,* vol. 46, no. 3, pp. 2241-2276, 2022.

[68] D. Lee, D. Choi, H. Park, H. Lee, and S. J. Kim, "Electroconvective circulating flows by asymmetric Coulombic force distribution in multiscale porous membrane," *Journal of Membrane Science,* vol. 636, 2021, doi: 10.1016/j.memsci.2021.119286.

[69] B. Cooke, "Concentration polarization in electrodialysis—I. The electrometric measurement of interfacial concentration," *Electrochimica Acta,* vol. 3, no. 4, pp. 307-317, 1961.

[70] K. Spiegler, "Polarization at ion exchange membrane-solution interfaces," *Desalination,* vol. 9, no. 4, pp. 367-385, 1971.

[71] S. J. Kim, Y. A. Song, and J. Han, "Nanofluidic concentration devices for biomolecules utilizing ion concentration polarization: theory, fabrication, and applications," *Chem Soc Rev,* vol. 39, no. 3, pp. 912-22, Mar 2010, doi: 10.1039/b822556g.

[72] J.-H. Choi, J.-S. Park, and S.-H. Moon, "Direct measurement of concentration distribution within the boundary layer of an ion-exchange membrane," *Journal of colloid and interface science,* vol. 251, no. 2, pp. 311-317, 2002.

[73] B. Cooke and S. Van der Walt, "Concentration polarization in electrodialysis—III. Practical electrodialysis systems," *Electrochimica Acta,* vol. 5, no. 3, pp. 216-228, 1961.

[74] S. J. Kim, L. D. Li, and J. Han, "Amplified electrokinetic response by concentration polarization near nanofluidic channel," *Langmuir,* vol. 25, no. 13, pp. 7759-65, Jul 7 2009, doi: 10.1021/la900332v.

[75] R. Ibanez, D. F. Stamatialis, and M. Wessling, "Role of membrane surface in concentration polarization at cation exchange membranes," *Journal of Membrane Science,* vol. 239, no. 1, pp. 119-128, 2004, doi: 10.1016/j.memsci.2003.12.032.

[76] I. Rubinstein and L. Shtilman, "Voltage against current curves of cation exchange membranes," *Journal of the Chemical Society, Faraday Transactions 2: Molecular and Chemical Physics,* vol. 75, pp. 231-246, 1979.

[77] J. C. de Valença, R. M. Wagterveld, R. G. Lammertink, and P. A. Tsai, "Dynamics of microvortices induced by ion concentration polarization," *Physical Review E,* vol. 92, no. 3, p. 031003, 2015.

[78] H. Lee, "Time-resolved Analysis for Electroconvective Instability under Potentiostatic Mode," *Korean Chemical Engineering Research,* vol. 58, no. 2, pp. 319-324, 2020.

[79] E. Demekhin, N. Nikitin, and V. Shelistov, "Direct numerical simulation of electrokinetic instability and transition to chaotic motion," *Physics of Fluids,* vol.

25, no. 12, p. 122001, 2013.
[80] H. Strathmann, "Electrodialysis, a mature technology with a multitude of new applications," *Desalination,* vol. 264, no. 3, pp. 268-288, 2010.
[81] L. Bazinet and T. R. Geoffroy, "Electrodialytic processes: Market overview, membrane phenomena, recent developments and sustainable strategies," *Membranes,* vol. 10, no. 9, p. 221, 2020.
[82] K. S. Barros, M. C. Martí-Calatayud, T. Scarazzato, A. M. Bernardes, D. C. R. Espinosa, and V. Pérez-Herranz, "Investigation of ion-exchange membranes by means of chronopotentiometry: A comprehensive review on this highly informative and multipurpose technique," *Advances in Colloid and Interface Science,* vol. 293, p. 102439, 2021.
[83] A. Mani and K. M. Wang, "Electroconvection Near Electrochemical Interfaces: Experiments, Modeling, and Computation," *Annual Review of Fluid Mechanics,* vol. 52, no. 1, pp. 509-529, 2020, doi: 10.1146/annurev-fluid-010719-060358.
[84] K. Huh, S. Y. Yang, J. S. Park, J. A. Lee, H. Lee, and S. J. Kim, "Surface conduction and electroosmotic flow around charged dielectric pillar arrays in microchannels," *Lab Chip,* vol. 20, no. 3, pp. 675-686, Feb 7 2020, doi: 10.1039/c9lc01008d.
[85] H. Lee *et al.*, "Overlimiting Current in Nonuniform Arrays of Microchannels: Recirculating Flow and Anticrystallization," *Nano Lett,* vol. 21, no. 12, pp. 5438-5446, Jun 23 2021, doi: 10.1021/acs.nanolett.0c05049.
[86] I. Rubinstein, B. Zaltzman, and T. Pundik, "Ion-exchange funneling in thin-film coating modification of heterogeneous electrodialysis membranes," *Physical review E,* vol. 65, no. 4, p. 041507, 2002.
[87] J. de Valenca, M. Jogi, R. M. Wagterveld, E. Karatay, J. A. Wood, and R. G. H. Lammertink, "Confined Electroconvective Vortices at Structured Ion Exchange Membranes," *Langmuir,* vol. 34, no. 7, pp. 2455-2463, Feb 20 2018, doi: 10.1021/acs.langmuir.7b04135.
[88] E. Korzhova, N. Pismenskaya, D. Lopatin, O. Baranov, L. Dammak, and V. Nikonenko, "Effect of surface hydrophobization on chronopotentiometric behavior of an AMX anion-exchange membrane at overlimiting currents," *Journal of Membrane science,* vol. 500, pp. 161-170, 2016.
[89] V. Gil *et al.*, "Impact of heterogeneous cation-exchange membrane surface modification on chronopotentiometric and current–voltage characteristics in NaCl, CaCl2 and MgCl2 solutions," *Electrochimica Acta,* vol. 281, pp. 472-485, 2018.
[90] J. Balster *et al.*, "Morphology and microtopology of cation-exchange polymers and the origin of the overlimiting current," *The Journal of Physical Chemistry B,* vol. 111, no. 9, pp. 2152-2165, 2007.
[91] V. Sarapulova *et al.*, "Transport Characteristics of CJMAED Homogeneous Anion Exchange Membranes in Sodium Chloride and Sodium Sulfate Solutions," *Int J Mol Sci,* vol. 22, no. 3, Jan 31 2021, doi: 10.3390/ijms22031415.
[92] E. Stránská and D. Neděla, "Reinforcing fabrics as the mechanical support of ion exchange membranes," *Journal of Industrial Textiles,* vol. 48, no. 2, pp. 432-447, 2018.
[93] S. A. Mareev, D. Y. Butylskii, N. D. Pismenskaya, C. Larchet, L. Dammak, and V. V. Nikonenko, "Geometric heterogeneity of homogeneous ion-exchange Neosepta membranes," *Journal of Membrane Science,* vol. 563, pp. 768-776, 2018, doi: 10.1016/j.memsci.2018.06.018.
[94] K. Nebavskaya *et al.*, "Impact of ion exchange membrane surface charge and hydrophobicity on electroconvection at underlimiting and overlimiting currents,"

Journal of Membrane Science, vol. 523, pp. 36-44, 2017.

[95] J. Choi, A. Mani, H. Lee, and S. J. Kim, "Investigation on the Stability of Random Vortices in an Ion Concentration Polarization Layer with Imposed Normal Fluid Flow," *Micromachines (Basel),* vol. 11, no. 5, May 22 2020, doi: 10.3390/mi11050529.

[96] V. S. Pham, Z. Li, K. M. Lim, J. K. White, and J. Han, "Direct numerical simulation of electroconvective instability and hysteretic current-voltage response of a permselective membrane," *Phys Rev E Stat Nonlin Soft Matter Phys,* vol. 86, no. 4 Pt 2, p. 046310, Oct 2012, doi: 10.1103/PhysRevE.86.046310.

[97] P. Shi and W. Liu, "Length-dependent instability of shear electroconvective flow: From electroconvective instability to Rayleigh-Benard instability," *Journal of Applied Physics,* vol. 124, no. 20, p. 204304, 2018.

[98] E. Karatay, M. B. Andersen, M. Wessling, and A. Mani, "Coupling between buoyancy forces and electroconvective instability near ion-selective surfaces," *Physical review letters,* vol. 116, no. 19, p. 194501, 2016.

[99] W. Liu, Y. Zhou, and P. Shi, "Scaling laws of electroconvective flow with finite vortex height near permselective membranes," *Physical Review E,* vol. 102, no. 3, p. 033102, 2020.

[100] E. Karatay, C. L. Druzgalski, and A. Mani, "Simulation of chaotic electrokinetic transport: performance of commercial software versus custom-built direct numerical simulation codes," *J Colloid Interface Sci,* vol. 446, pp. 67-76, May 15 2015, doi: 10.1016/j.jcis.2014.12.081.

[101] P. Shi, "Direct numerical simulation of electroconvection with thin Debye layer matching canonical experiments," *Physics of Fluids,* vol. 33, no. 3, p. 032015, 2021.

[102] M. B. Andersen, K. M. Wang, J. Schiffbauer, and A. Mani, "Confinement effects on electroconvective instability," *Electrophoresis,* vol. 38, no. 5, pp. 702-711, 2017.

[103] M. Seo, S. Park, J. Ryu, and S. J. Kim, "Adhesive Lift Method for Patterning Arbitrary-shaped Thin Ion-selective Films in Micro/Nanofluidic Device," *Lab on a Chip,* 2022.

[104] C. Druzgalski and A. Mani, "Statistical analysis of electroconvection near an ion-selective membrane in the highly chaotic regime," *Physical Review Fluids,* vol. 1, no. 7, p. 073601, 2016.

[105] A. M. Benneker, B. Gumuscu, E. G. H. Derckx, R. G. H. Lammertink, J. C. T. Eijkel, and J. A. Wood, "Enhanced ion transport using geometrically structured charge selective interfaces," *Lab Chip,* vol. 18, no. 11, pp. 1652-1660, May 29 2018, doi: 10.1039/c7lc01220a.

[106] N. A. Mishchuk, "Concentration polarization of interface and non-linear electrokinetic phenomena," *Adv Colloid Interface Sci,* vol. 160, no. 1-2, pp. 16-39, Oct 15 2010, doi: 10.1016/j.cis.2010.07.001.

[107] N. A. Mishchuk, "Polarization of systems with complex geometry," *Current Opinion in Colloid & Interface Science,* vol. 18, no. 2, pp. 137-148, 2013, doi: 10.1016/j.cocis.2013.02.005.

[108] S. M. Davidson, M. Wessling, and A. Mani, "On the dynamical regimes of pattern-accelerated electroconvection," *Sci Rep,* vol. 6, no. 1, pp. 1-10, 2016.

[109] F. Roghmans *et al.*, "2D patterned ion-exchange membranes induce electroconvection," *Advanced Materials Interfaces,* vol. 6, no. 1, p. 1801309, 2019.

[110] S. Park and R. Kwak, "Microscale electrodeionization: In situ concentration profiling and flow visualization," *Water research,* vol. 170, p. 115310, 2020.

[111] S. J. Kim, S. H. Ko, R. Kwak, J. D. Posner, K. H. Kang, and J. Han, "Multi-vortical

flow inducing electrokinetic instability in ion concentration polarization layer," *Nanoscale,* vol. 4, no. 23, pp. 7406-10, Dec 7 2012, doi: 10.1039/c2nr32467a.
[112] R. Kwak, J. Y. Kang, and T. S. Kim, "Spatiotemporally defining biomolecule preconcentration by merging ion concentration polarization," *Analytical chemistry,* vol. 88, no. 1, pp. 988-996, 2016.
[113] A. Kovalenko *et al.*, "Space-Charge breakdown phenomenon and spatio-temporal ion concentration and fluid flow patterns in overlimiting current electrodialysis," *Journal of Membrane Science,* vol. 636, p. 119583, 2021.
[114] J. Kim, S. Kim, and R. Kwak, "Controlling ion transport with pattern structures on ion exchange membranes in electrodialysis," *Desalination,* vol. 499, p. 114801, 2021.
[115] V. V. Nikonenko *et al.*, "Desalination at overlimiting currents: State-of-the-art and perspectives," *Desalination,* vol. 342, pp. 85-106, 2014.
[116] S. Choi *et al.*, "Techno-economic analysis of ion concentration polarization desalination for high salinity desalination applications," *Water research,* vol. 155, pp. 162-174, 2019.
[117] K. Kim, W. Kim, H. Lee, and S. J. Kim, "Stabilization of ion concentration polarization layer using micro fin structure for high-throughput applications," *Nanoscale,* 10.1039/C6NR08978J vol. 9, no. 10, pp. 3466-3475, 2017, doi: 10.1039/C6NR08978J.
[118] A. Gonzalez-Vogel and O. J. Rojas, "Exploiting electroconvective vortices in electrodialysis with high-frequency asymmetric bipolar pulses for desalination in overlimiting current regimes," *Desalination,* vol. 474, p. 114190, 2020.
[119] J. Han, J. Fu, and R. B. Schoch, "Molecular Sieving Using Nanofilters: Past, Present and Future," *Lab Chip,* vol. 8, pp. 23-33, 2008, doi: 10.1039/b714128a.
[120] A. Bennett, "Membrane technology: Developments in ultrafiltration technologies," *Filtration+ Separation,* vol. 49, no. 6, pp. 28-33, 2012.
[121] G. W. Slater and J. Noolandi, "On the reptation theory of gel electrophoresis," *Biopolymers,* vol. 25, pp. 431-454, 1986.
[122] O. J. Lumpkin, P. Dejardin, and B. H. Zimm, "Theory of gel electrophoresis of DNA," *Biopolymers,* vol. 24, pp. 1573-1593, 1985. [Online]. Available: http://dx.doi.org/10.1002/bip.360240812.
[123] O. J. Lumpkin and B. H. Zimm, "Mobility of DNA in Gel Electrophoresis," *Biopolymers,* vol. 21, pp. 2315-2316, 1982.
[124] H. M. Georgiou, G. E. Rice, and M. S. Baker, "Proteomic analysis of human plasma: Failure of centrifugal ultrafiltration to remove albumin and other high molecular weight proteins," *Proteomics,* vol. 1, no. 12, pp. 1503-1506, 2001. [Online]. Available: http://dx.doi.org/10.1002/1615-9861(200111)1:12<1503::AID-PROT1503>3.0.CO;2-M.
[125] J. Han and H. G. Craighead, "Separation of Long DNA Molecules in a Microfabricated Entropic Trap Array," *Science,* vol. 288, pp. 1026-1029, 2000. [Online]. Available: http://dx.doi.org/10.1126/science.288.5468.1026.
[126] J. Fu, R. R. Schoch, A. L. Stevens, S. R. Tannenbaum, and J. Han, "Patterned anisotropic nanofluidic sieving structure for continuous-flow separation of DNA and protein," *Nat. Nanotech.,* vol. 2 no. 2, pp. 121 - 128, 2006, doi: 10.1038/nnano.2006.206.
[127] T. Salafi, K. K. Zeming, and Y. Zhang, "Advancements in microfluidics for nanoparticle separation," *Lab Chip,* vol. 17, no. 1, pp. 11-33, 2017.
[128] X. C. Xuan, J. J. Zhu, and C. Church, "Particle focusing in microfluidic devices,"

(in English), *Microfluidics and Nanofluidics,* Review vol. 9, no. 1, pp. 1-16, Jul 2010, doi: 10.1007/s10404-010-0602-7.

[129] X. Sun *et al.*, "Separation of Nanoparticles in a Density Gradient: FeCo@C and Gold Nanocrystals," *Angew. Chem.,* vol. 48, pp. 939-942, 2009.

[130] D. Di Carlo, D. Irimia, R. G. Tompkins, and M. Toner, "Continuous inertial focusing, ordering, and separation of particles in microchannels," *Proc. Natl. Acad. Sci. U. S. A.,* vol. 104, no. 48, pp. 18892-18897, 2007. [Online]. Available: http://dx.doi.org/10.1073/pnas.0704958104.

[131] D. Di Carlo, "Inertial microfluidics," *Lab Chip,* vol. 9, no. 21, pp. 3038-3046, 2009.

[132] S. S. Kuntaegowdanahalli, A. A. S. Bhagat, G. Kumar, and I. Papautsky, "Inertial microfluidics for continuous particle separation in spiral microchannels," *Lab Chip,* vol. 9, no. 20, pp. 2973-2980, 2009.

[133] H. Jeon, H. Lee, K. H. Kang, and G. Lim, "Ion concentration polarization-based continuous separation device using electrical repulsion in the depletion region," (in English), *Sci Rep,* Article vol. 3, Dec 2013, Art no. 3483, doi: 10.1038/srep03483.

[134] S. J. Kim, Y.-A. Song, and J. Han, "Nanofluidic concentration devices for biomolecules utilizing ion concentration polarization: theory, fabrication, and application," *Chem. Soc. Rev.,* vol. 39, pp. 912-922, 2010, doi: 10.1039/b822556g.

[135] R. Kwak, S. J. Kim, and J. Han, "Continuous-flow biomolecule and cell concentrator by ion concentration polarization," *Anal. Chem.,* vol. 83, pp. 7348-7355, 2011.

[136] W. Kim, S. Park, K. Kim, and S. J. Kim, "Experimental verification of simultaneous desalting and molecular preconcentration by ion concentration polarization," *Lab Chip,* vol. 17, no. 22, pp. 3841-3850, 2017.

[137] J. Choi *et al.*, "Nanoelectrokinetic Selective Preconcentration Based on Ion Concentration Polarization," *BioChip Journal,* pp. 1-10, 2020.

[138] S. Hong, R. Kwak, and W. Kim, "Paper-Based Flow Fractionation System Applicable to Preconcentration and Field-Flow Separation," *Anal. Chem.,* vol. 88, no. 3, pp. 1682-1687, 2016.

[139] Y.-Y. Chen, P.-H. Chiu, C.-H. Weng, and R.-J. Yang, "Preconcentration of diluted mixed-species samples following separation and collection in a micro–nanofluidic device," *Biomicrofluidics,* vol. 10, no. 1, p. 014119, 2016.

[140] B. Zaltzman and I. Rubinstein, "Electro-osmotic slip and electroconvective instability," *J. Fluid Mech.,* vol. 579, pp. 173-226, 2007.

[141] I. Rubinstein and B. Zaltzman, "Equilibrium Electroconvective Instability," *Phys. Rev. Lett.,* vol. 114, no. 11, p. 114502, 03/16/ 2015. [Online]. Available: http://link.aps.org/doi/10.1103/PhysRevLett.114.114502.

[142] Y. Pawar, Y. E. Solomentsev, and J. L. Anderson, "Polarization Effects on Diffusiophoresis in Electrolyte Gradients," *J. Colloid Interface Sci.,* vol. 155, no. 2, pp. 488-498, 1993/2 1993. [Online]. Available: C:\Documents and Settings\Jongyoon Han\Desktop\PDF\Nanofilter\1993 JCIS Pawar Anderson Diffusoelectrophoresis.pdf.

[143] D. Ha, S. Seo, K. Lee, and T. Kim, "Dynamic Transport Control of Colloidal Particles by Repeatable Active Switching of Solute Gradients," *ACS Nano,* vol. 13, no. 11, pp. 12939-12948, 2019.

[144] J. Anderson, M. Lowell, and D. Prieve, "Motion of a particle generated by chemical gradients Part 1. Non-electrolytes," *J. Fluid Mech.,* vol. 117, pp. 107-121, 1982.

[145] H. J. Keh and Y. K. Wei, "Diffusiophoretic mobility of spherical particles at low potential and arbitrary double-layer thickness," *Langmuir,* vol. 16, no. 12, pp. 5289-

5294, 2000.
[146] S. Shin *et al.*, "Size-dependent control of colloid transport via solute gradients in dead-end channels," *Proc. Natl. Acad. Sci.,* vol. 113, no. 2, pp. 257-261, 2016.
[147] S. Shin, J. T. Ault, J. Feng, P. B. Warren, and H. A. Stone, "Low-Cost Zeta Potentiometry Using Solute Gradients," *Advanced Materials,* vol. 29, no. 30, p. 1701516, 2017.
[148] S. Shin, J. T. Ault, P. B. Warren, and H. A. Stone, "Accumulation of Colloidal Particles in Flow Junctions Induced by Fluid Flow and Diffusiophoresis," *Physical Review X,* vol. 7, no. 4, p. 041038, 2017.
[149] T. J. Shimokusu, V. G. Maybruck, J. T. Ault, and S. Shin, "Colloid Separation by CO2-Induced Diffusiophoresis," *Langmuir,* 2020.
[150] D. Florea, S. Musa, J. M. Huyghe, and H. M. Wyss, "Long-range repulsion of colloids driven by ion exchange and diffusiophoresis," *Proc. Natl. Acad. Sci.,* vol. 111, no. 18, pp. 6554-6559, 2014.
[151] S. Musa, D. Florea, H. M. Wyss, and J. M. Huyghe, "Convection associated with exclusion zone formation in colloidal suspensions," *Soft Matter,* vol. 12, no. 4, pp. 1127-1132, 2016.
[152] H. Lee, J. Kim, J. Yang, S. W. Seo, and S. J. Kim, "Diffusiophoretic exclusion of colloidal particles for continuous water purification," *Lab Chip,* vol. 18, pp. 1713-1724, 2018.
[153] D. Lee, J. A. Lee, H. Lee, and S. J. Kim, "spontaneous selective preconcentration Leveraged by Ion exchange and Imbibition through Nanoporous Medium," *Sci Rep,* vol. 9, no. 1, p. 2336, 2019.
[154] J. A. Lee, D. Lee, S. Park, H. Lee, and S. J. Kim, "Non-negligible Water-permeance through Nanoporous Ion Exchange Medium," *Sci Rep,* vol. 8, no. 1, p. 12842, 2018.
[155] J. Choi, H. Lee, and S. J. Kim, "Hierarchical micro/nanoporous ion-exchangeable sponge," *Lab Chip,* vol. 20, pp. 503-513, 2020.
[156] H. J. Keh and Y. K. Wei, "Osmosis through a fibrous medium caused by transverse electrolyte concentration gradients," *Langmuir,* vol. 18, no. 26, pp. 10475-10485, 2002.
[157] T. Pedley, "Calculation of unstirred layer thickness in membrane transport experiments: a survey," *Q. Rev. Biophys.,* vol. 16, no. 2, pp. 115-150, 1983.
[158] D. C. Prieve, "Migration of a colloidal particle in a gradient of electrolyte concentration," *Advances in Colloid and Interface Science,* vol. 16, no. 1, pp. 321-335, 1982.
[159] K. L. Saar *et al.*, "On-chip label-free protein analysis with downstream electrodes for direct removal of electrolysis products," *Lab Chip,* vol. 18, no. 1, pp. 162-170, 2018.
[160] J. C. Giddings, "Unified Separation Science," in *Unified Separation Science*: John Wiley & Sons, Inc., 1991, pp. 200-219.
[161] R. A. Durst and B. R. Staples, "Tris/Tris· HCl: a standard buffer for use in the physiologic pH range," *Clin. Chem.,* vol. 18, no. 3, pp. 206-208, 1972.
[162] R. Niu *et al.*, "Microfluidic pumping by micromolar salt concentrations," *Soft Matter,* 10.1039/C6SM02240E vol. 13, no. 7, pp. 1505-1518, 2017, doi: 10.1039/C6SM02240E.
[163] Y. Pocker and D. W. Bjorkquist, "Stopped-flow studies of carbon dioxide hydration and bicarbonate dehydration in water and water-d2. Acid-base and metal ion catalysis," *J. Am. Chem. Soc.,* vol. 99, no. 20, pp. 6537-6543, 1977/09/01 1977, doi: 10.1021/ja00462a012.

[164] A. T. Brown, W. C. K. Poon, C. Holm, and J. de Graaf, "Ionic screening and dissociation are crucial for understanding chemical self-propulsion in polar solvents," *Soft Matter,* 10.1039/C6SM01867J vol. 13, no. 6, pp. 1200-1222, 2017, doi: 10.1039/C6SM01867J.

[165] G. I. Taylor, "The dispersion of matter in turbulent flow through a pipe," *Proceedings of the Royal Society of London. Series A. Mathematical and Physical Sciences,* vol. 223, no. 1155, pp. 446-468, 1954.

[166] G. Pardon and W. van der Wijngaart, "Modeling and simulation of electrostatically gated nanochannels," *Adv. Colloid Interface Sci.,* vol. 199-200, pp. 78-94, 2013/11/01/ 2013, doi: https://doi.org/10.1016/j.cis.2013.06.006.

Abstract in Korean

나노채널은 나노채널의 독특한 특성으로 인해 마이크로/나노유체 시스템에서 널리 활용되어 왔다. 나노채널의 독특한 특성 중 하나로 전기 이중층의 겹침에 의해 유도되는 이온 선택성이 있다. 이온 선택성을 활용하여, 나노 채널을 사용하는 전기수력학적 시스템이 다양하게 개발되어 왔다. 마이크로/나노 유체 플랫폼은 확장성과 가시성이라는 장점으로 인해, 전기수력학 시스템에 대한 이해를 위한 연구에 활용되어 왔다. 따라서 마이크로 장치는 실제 시스템을 모사하기 위해 실제 시스템의 특성을 모방하는 디자인으로 제작되어 왔다. 하지만 나노채널 제작 기술의 한계로 인해 장치의 설계에 제한이 있었다. 따라서 본 논문에서는 나노다공성막 패터닝 방법을 개발하고 해당 패터닝 방법으로 제작된 마이크로/나노유체 플랫폼을 이용하여 플랫폼 내의 농도 경계층을 조사하였다.

먼저 임의의 모양을 가진 나노다공성 막의 제작을 위한 접착식 리프트 방식을 제안하였다. 해당 방식은 산소 플라즈마 처리와 스핀 코팅을 활용하여 균일하고 정밀한 나노다공성 막의 패터닝이 가능하다. 제작 방식의 유효성을 입증하기 위해, 사각파, 사인파, 톱니파, 삼각파, 프랙탈 형태의 모양을 가지며, 5 μm, 15 μm, 150 μm 의 두께를 가진 마이크로채널을 따라 패터닝 된 나노다공성 막이 있는

마이크로/나노유체 플랫폼을 제작하였다. 패터닝의 정확성은 이온 농도 분극의 세 가지 메커니즘 (표면 전도, 전기삼투유동, 전기삼투 불안정)의 가시화를 통해 확인하였다. 또한, 전기삼투유동 영역과 전기삼투 불안정 영역에서의 굴곡진 표면의 이온 농도 분극에 대한 영향의 차이를 직접적인 가시화와 전기적인 측정을 통해 평가하였다. 따라서 제안된 나노다공성 막 제작 방식이 실제 시스템과 유사한 마이크로/나노 유체 플랫폼의 제작을 가능하게 할 것이라 기대한다.

두번째로 이온 교환 막의 물리적 요소로 활용되어온 강화 구조를 활용한 전기와류의 정렬에 대해 입증하였다. 실험 장치는 접착식 리프트 방식을 활용하여 제작하였다. 안정적인 전기와류는 강화 체의 폭이 넓고 이온공핍층과 가까울 때 정렬된다는 것을 전산 모사와 실험을 통해 확인하였으며, 와류 정렬을 위한 강화체의 기하학적 조건을 확인하였다. 또한 강화체를 이용해 혼돈 영역에서도 전기 와류를 정렬하였다. 전기 와류는 정렬로 인해 안정화되었으며, 해당 안정화는 시간으로 평균한 양이온 농도 분포(전산 모사) 및 형광 세기 분포(실험)을 통해 수치화하였다. 또, 전류 또한 나노다공성 막 내의 강화체를 통해 안정화되었음을 입증하였다. 따라서 강화체가 다양한 농도 분극 시스템 내의 전기 와류의 안정화에 활용될 수 있음을 제안한다.

마지막으로 이온 교환으로 인한 확산영동을 기반으로 한 연속적이고 자발적인 나노입자 분리 장치를 제안하였다. 확산영동 기반의 분리 장치는 접착식 리프트 방식을 활용하여 제작하였다. 분리 장치 내의

배제 거리에 대한 경향성은 기존의 자발적 확산영동 기반의 시스템의 경향성을 따랐다. 따라서 크기의 차이(40 nm, 200 nm, 2 μm)로 인한 확산영동적 이동도를 띈 파티클을 분리하는 것이 가능했다. 또한 Tris 버퍼 용액의 추가를 통해 이온 농도 구배를 향상시켜 분리 효율을 증가시켰다. Tris를 추가는 분리된 버퍼 용액이 pH에 민감한 생체 분자에 적합하도록 하는 역할도 했다. 따라서 제안된 연속적이고 자발적인 확산영동 기반의 분리 플랫폼이 다양한 나노 생체 분자의 분석에 활용될 수 있음을 기대한다.

주요어: 전기수력학 현상, 접착식 리프트 방식, 이온 선택성, 이온 농도 분극, 전기와류, 확산영동

학번: 2017-23030